Imaging of Single Quantum Emitters Using Azimuthally and Radially Polarized Laser Beams

Dissertation

der Mathematisch-Naturwissenschaftlichen Fakultät

der Eberhard Karls Universität Tübingen

zur Erlangung des Grades eines

Doktors der Naturwissenschaften

(Dr. rer. nat.)

vorgelegt von

Dipl.-Phys. Anna Chizhik

aus Sankt Petersburg

Tübingen

2010

Tag der mündlichen Qualifikation:	15.12.2010
Dekan:	Prof. Dr. Wolfgang Rosenstiel
1. Berichterstatter:	Prof. Dr. Alfred J. Meixner
2. Berichterstatter:	Prof. Dr. Michael Hanack

Contents

1 Introduction **5**

1.1 Aim of this Thesis……...5

1.2 Scope of this Thesis……7

2 Instrumentation and Higher-Order Laser Modes **9**

2.1 Instrumentation……10

2.2 Higher-Order Laser Modes: Azimuthally and Radially Polarized Laser Beams.....12

2.3 Imaging of Single Quantum Emitters Using Linearly Polarized Laser Beam……..17

2.4 Imaging of Fluorescence Spheres Using Higher-Order Laser Modes.....19

2.5 Imaging of Single Molecules Using Higher-Order Laser Modes….....20

2.6 Summary and Conclusion…….....23

3 Imaging of the Excited-State Tautomerization in Single Metal-Free Phthalocyanine and Porphyrin Molecules **24**

3.1 Introduction……...25

3.2 Experimental…….27

3.3 NH Tautomerization…….28

3.4 Simulated Excitation Patterns for Different Angles between Two Dipoles and Different Orientation of the Molecule……....29

3.5 Imaging of the Tautomerism Process in Single Phthalocyanine Molecules Using Higher-Order Laser Modes ……32

3.6 Imaging of the Tautomerism Process in Single Porphyrin Molecules Using an Azimuthally Polarized Laser Beam.……...34

3.7 Summary and Conclusion…….37

4 Imaging of Single CdSe/ZnS Quantum Dots **39**

4.1 Introduction……...40

4.2 Experimental…….41

4.3 Fluorescence Imaging of Single CdSe/ZnS Quantum Dotes Using Higher-Order Laser Modes……42

4.4 Blinking and Bleaching Behavior of Single CdSe/ZnS Quantum Dots……...45

4.5 Summery and Conclusion……..…46

5 Imaging of Defect Luminescence in Single SiO_2 Nanoparticles 47

5.1 Introduction……..48

5.2 Experimental…….49

5.3 3D Transition Dipole Moment Orientation of Single SiO_2 Nanoparticles……...50

5.4 Emission Polarization of Single SiO_2 Nanoparticles……51

5.5 Blinking and Bleaching Behavior of Single SiO_2 Nanoparticles……..53

5.6 Flipping of the Transition Dipole Moment Orientation in Single SiO_2 Nanoparticles……..53

5.7 Summary and Conclusion…….55

6 Luminescence Imaging of Individual Si Nanocrystals. Part I: Defect Photoluminescence 56

6.1 Introduction……...57

6.2 Experimental…….58

6.3 Fluorescence Imaging of Single Si NCs Using Higher-Order Laser Modes……61

6.4 Flipping of the Transition Dipole Moment Orientation in Single Si Nanocrystals……..……...63

6.5 Summary and Conclusion…….64

7 Luminescence Imaging of Individual Si Nanocrystals. Part II: Exciton Photoluminescence 66

7.1 Introduction……...67

7.2 Experimental…….68

7.3 Fluorescence Imaging of Single Si Nanocrystals Using an Azimuthally Polarized Laser Beam…….69

7.4 Summary and Conclusion…….71

8 Investigation of the Single Stopcock Molecules Orientation at Channel Entrances of an Organic Host-Guest Compound 72

8.1 Introduction…….....73

8.2 Experimental…….74

8.3 Density Functional Theory Calculations……..75

8.4 Single Stopcock Molecules in the Glass-Air Confinement……..76

8.5 PHTP – Crystals without Stopcock Molecules…….76

8.6 PHTP – Crystals with Stopcock Molecules……..77

8.7 Distribution of the Stopcock Molecules in the Channels……..79

8.8 PHTP – Crystals with Single Stopcock Molecules……...81

8.9 Crystals Oriented Vertically with Respect to the Sample Surface……...82

8.10 Summary and Conclusion……...84

9 Investigation of the Single CdSe/ZnS Quantum Dots Orientation in the Channels of Porous Silica Beads 85

9.1 Introduction……...86

9.2 Experimental…….86

9.3 Single Quantum Dots in the Glass-Air Confinement……...88

9.4 Porous Silica Beads without and with Quantum Dots in the Channels……89

9.5 Porous Silica Beads with Single Quantum Dots in the Channels…….90

9.6 Distribution of the Quantum Dots in the Channels……...91

9.7 Summary and Conclusion…….92

List of the Abbreviations 93

References 94

A Acknowledgement 102

B Abstract 104

C Zusammenfassung 106

1 Introduction

1.1 Aim of this Thesis

The combination of confocal microscopy with cylindrical vector beams (CVB) (azimuthally and radially polarized laser beams) is widely used for the investigation of the single quantum emitters. This method provides information about the excitation transition dipole moment (TDM), while other microscopy techniques, e. g. defocusing imaging [1, 2] or polarization microscopy [3], provide information about the emission TDM. It has proven to be very efficient in probing the three-dimensional orientation and dimensionality of excitation TDM of single molecules [4-6], Nile Red nano-spheres [7-9], SiO_2 nanoparticles [10, 11], gold nanoparticles [12] and gold cones [13].

By comparing experimental and simulated excitation patterns of the single dye molecules excited with an azimuthally or radially polarized laser beam (APLB and RPLB, respectively) one can determine the two dimensional (2D) or three dimensional (3D) excitation TDM orientation, respectively [4]. This information is important for such applications, as Förster resonance energy transfer (FRET), since the efficiency not only depends on the distance between donor and acceptor molecules, but also on relative orientations of the two molecules.

The CVB technique has been applied for imaging of the excited-state tautomerism process in single porphycene molecules [14, 15]. Single molecule excitation patterns exhibit the reorientation of the TDM during the tautomerization and give the information about 3D orientation of the molecules with respect to the sample surface, the angle between the two TDMs of the molecule upon the tautomerism process and frequency of the TDM reorientation, which can strongly vary for different types of the molecules.

Furthermore, it has been shown that the CVB can be used not only for investigation of the emitter in free space, but also inside a tunable optical microresonator. By analyzing the excitation patterns, resulting from the illumination with a RPLB, the longitudinal position of the fluorescent Nile Red nano-beads or 3D orientation of the single molecules inside the tunable microresonator can be determined [6, 8].

Recently it has been shown that this method can be also used for scattering imaging of different shape single Au nanoparticles (spheres, rods, triangles) [12, 16]. The

scattering images of the single Au nanoparticles excited with CVB provide an information about the particles position, orientation, size and shape.

In this study we investigate photo-physical and photo-chemical properties of single molecules and semiconductor quantum dots by imaging their excitation TDM using confocal microscopy combined with APLB and RPLB. We show that using this technique the 3D orientation, dimensionality and dynamical effects of the excitation TDM of single quantum emitters can be determined.

The work can be divided into the three main parts:

1. The determination of 3D TDM orientation and study of the tautomerism process in single dye molecules.

2. The investigation of direct/indirect band gap semiconductor single quantum dots and single silicon dioxide nanoparticles.

3. The study of host-guest compounds: the orientation of the guest molecules or quantum dots in the channels of host compounds.

1.2 Scope of this Thesis

Each of the chapters presents independent topics of the research. Chapter 2 gives an overview of the experimental methods and equipment used in this study. Each chapter starts with an introduction of the object of the research and experimental part which refers to the specific instrumentation briefly presented in chapter 2.1.

In chapters 3, we investigate the changing of the TDM orientation during the excited-state tautomerism process in single metal-free phthalocyanine and porphyrin molecules. In the case of phthalocyanine molecules the fluorescence excitation patterns show that the angle between the transition dipole moments of the two trans forms is near 90^{o}. Most of porphyrin molecules exhibit the absence of the tautomerism process, while for 7% of the total number of investigated molecules we observe excitation patterns of two different trans forms of the same single molecule. Experimental results are in good agreement with theoretical prediction based on quantum chemical calculations.

In chapter 4, we investigate the excitation TDM of the single CdSe/ZnS quantum dots (QD). We study different types of commercially available water/toluene soluble QDs. We show that single CdSe/ZnS QDs possess 3D excitation TDM in contrast to dye molecules which possess linear excitation TDM. We demonstrate that using the CVB we can determine the dimensionality of the excitation TDM. Investigated QDs show characteristic dynamical effects featuring single QDs such as fluorescence intermittency (blinking and bleaching).

In chapter 5, we study single SiO_2 nanoparticles (NPs) which possess defect luminescence. The obtained results clearly demonstrate the presence of the one-dimensional TDM of SiO_2 NPs. Moreover, image series of the same sample area revealed the possibility for some silica NPs to change their TDM orientation from one image to another.

In chapter 6 and 7, we investigate single Si/SiO_2 core-shell nanocrystals (Si NCs) produced by laser pyrolysis. In chapter 6, we study samples with single Si NCs embedded in polymer matrix which were prepared by method of spin coating. In chapter 7, we study the Si NCs which were directly deposited on the surface of the glass cover slide. We show that samples with Si NCs prepared by method of spin coating possess defect photoluminescence, while some of directly deposited Si NCs possess emission due to the

quantum confined electron-hole recombination. We demonstrate that Si NC with defect photoluminescence possess linear excitation TDM, while Si NCs with exciton photoluminescence - 3D excitation TDM.

In chapters 8 and 9, we demonstrate that the orientation of the single quantum emitters can be determined not only in polymer layer spin coated on the glass cover slide surface but, for example, inside the nanochannels of host materials. We investigate two different types of host-guest compounds. In chapter 8, we show the ability of new type of stopcock molecules close the channels of the organic crystals. Using an APLB we determine the single stopcock molecules orientation in the nanochannel entrances of the crystals.

In chapter 9, we study mesoporous silica beads with included CdSe/ZnS QDs in the channels. The beads with different concentration of the QDs included in the channels were investigated. Using an APLB for the sample excitation we determine the orientation of single QDs in the channels of mesoporous silica beads.

2 Instrumentation and Higher-Order Laser Modes

In this chapter we describe our experimental setup and present theoretical background as well as the use of basic cylindrical vector beams (azimuthally and radially polarized donut modes laser beams) to determine the three-dimensional orientation of the quantum emitters transition dipole moment. We show that analysis of the molecular emission patterns reveals the 3D orientations of the dipole moments.

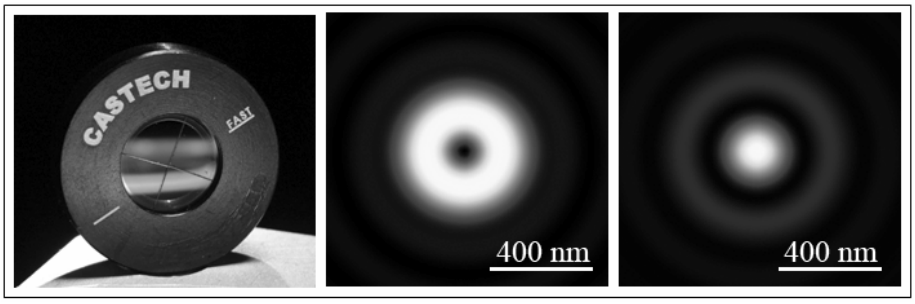

This chapter is based on:

D. Khoptyar, R. Gutbrod, A. M. Chizhik, J. Enderlein, F. Schleifenbaum, M. Steiner, A. J. Meixner, „Tight focusing of laser beams in a lambda/2-microcavity“ *Optics Express*, **16(13)**, 9907-9917, **2008**. link to article page

and

A. M. Chizhik, T. Schmidt, A. I. Chizhik, F. Huisken, A. J. Meixner, "Confocal Microscopy and Spectroscopy of Defect Photoluminescence in Single SiO_2 Nanoparticles", *Proc. SPIE,* **7393,** 739305, **2009**, doi:10.1117/12.825288. link to article page

and

S. Bär, A. I. Chizhik, R. Gutbrod, F. Schleifenbaum, A. M. Chizhik, A. J. Meixner, “Microcavities: tailoring the optical properties of single quantum emitters”, *Analytical and Bioanalytical Chemistry*, **396**, 3-14, **2010**. link to article page

2.1 Instrumentation

For optical measurements we use a home-build inverted confocal microscope with a high numerical aperture objective lens (NA = 1.25) to detect the orientation of the transition dipole moment (TDM) of single quantum emitters when excited by the doughnut modes. A scheme of the setup is depicted in Figure 1a. As

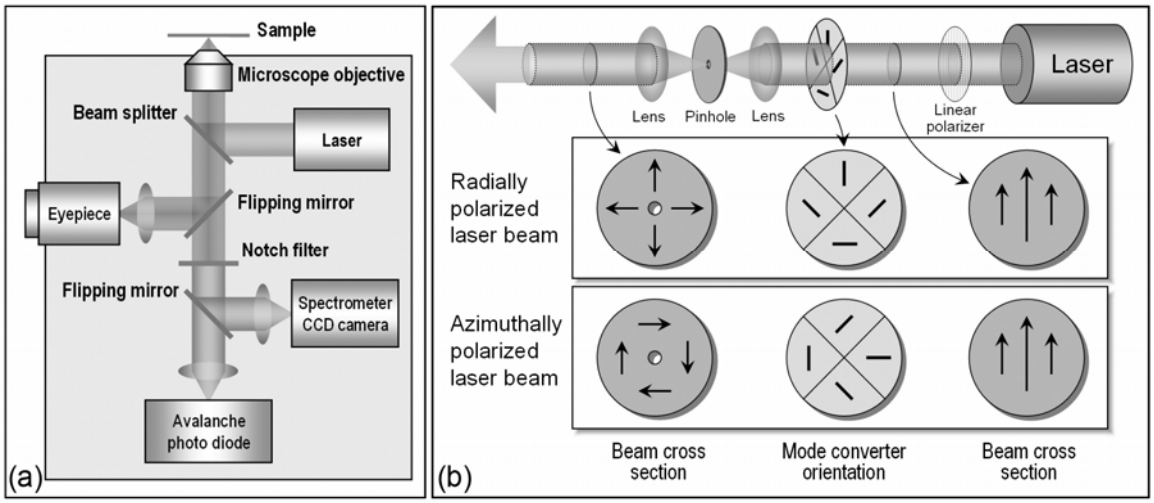

Figure 1. (a) Scheme of the home-built confocal microscope setup. (b) The laser beam polarization conversion technique and scheme of the laser beam cross-section before and after the polarization conversion.

excitation source an optically pumped semiconductor laser at 488 nm or a tunable argon-krypton laser, can be used. After the Gaussian beam passed through the mode-conversion optical line, the resulting doughnut laser mode is focused by the objective lens onto the sample. The fluorescence of the quantum emitters is collected through the same objective lens and focused on the detector. By raster scanning the sample through the focal spot, confocal images arise from the signals detected with an avalanche photo diode (APD). Additionally, a charge coupled device (CCD) camera acquires spectral information of selected emitters. The mode-conversion part consists of the mode-converter (see chapter 2.2 for details) and a pinhole with a diameter of 15 μm placed at the focal point between two lenses, to cut out other higher order modes, which occur due to structural discontinuity. Home-made mode-converters (Fig. 2) can be produced by cutting two λ/2 plates in four parts each: one perpendicular, one parallel and two others are shifted by 45° each, with respect to the polarization direction [17]. Then four of these eight parts (two

from each λ/2 plate) are glued together tilted by 45° towards each other, as shown in Figure 1b. By turning the mode-converter

Figure 2. The photo of the home-made mode-converter.

by 90° we can switch the polarization of the laser beam between azimuthal and radial polarization.

Sample preparation: For inverted confocal microscopes the samples have to be prepared on thin transparent substrates, like non-fluorescent glass cover slides (thickness of 170 μm), which have to be cleaned carefully to avoid any kind of contamination fluorescence. To obtain single quantum emitter concentrations on the sample, solutions of 10^{-9} mol/l are added to non-fluorescent transparent polymer solutions ≤1% and spin coated on the cleaned cover slides. For example, a layer prepared with a 1% poly(methyl-methacrylate) (PMMA, $[C_5O_2H_8]_n$) solution can reach a height of approximately 50 nm as determined by atomic force microscopy (AFM) measurements. A polymer matrix, e. g. PMMA or polystyrene (PS, $[C_8H_8]_n$), is used to fix the single emitters on the cover slide. Hence, translation and rotation of the quantum objects are excluded. In addition, the polymer matrix prevents the embedded quantum emitters from fast oxidation. Usually polymers are used, otherwise movement of the particles cannot be neglected, especially in the case of determination of their orientation. Depending on the speed of the spin coater (~ 8000 rpm), solutions with concentrations lower than 10^{-9} mol/l are needed.

Computational details: Electric field and excitation pattern calculations were performed with the "Focused Fields" program by A. Lieb [18] and with modified version of this program "PMCalc" (modified by M. Sackrow). Scan images were processed with WSxM software of Nanotec [19].

2.2 Higher-Order Laser Modes: Azimuthally and Radially Polarized Laser Beams

In this section the theoretical background of mode formation will be described.

In general, solving the scalar Helmholtz equation

$$(\Delta+k^2)E = 0 \tag{1}$$

for an electromagnetic field E, where k is the wavenumber, within the boundary conditions of a laser resonator results in stationary solutions, eigen states or what is referred to as modes. Applying the paraxial approximation the solution of these eigen states can be written as so called Hermite-Gauss modes (HG_{mn}) for cartesian coordinates or as Laguerre-Gauss modes (LG_{pl}) for cylindrical coordinates. These eigen states play an important role in optical and laser engineering. The simplest and often the most desirable type of beam provided by a laser source is the Gaussian beam, the fundamental transverse electromagnetic mode TEM_{00}. All types of higher order modes can be described by a linear combination of the Hermite-Gauss or Laguerre-Gauss modes. In general, there are two ways to generate these higher order laser modes: either inside a laser cavity or transforming the Gaussian laser beam extra-cavity using a mode converter. Intracavity formation of higher order laser modes can be achieved by a number of ways, e. g. axial intracavity birefringence [20, 21] or dichroism [22], diffractive phase plates or polarization selective end mirrors [23], and interferometric methods [24]. However, these methods require a more complex resonator design and/or special fabrication techniques. Thus, for most research areas, the passive generation of higher-order laser modes from a Gaussian beam outside the laser resonator delivers an adequate beam quality and it is much easier to achieve. The conversion can be realized by different types of mode converters. Liquid crystal mode converters [25] are convenient when different wavelengths have to be used to examine the sample. They are composed of cells containing the liquid crystals. By applying different voltages to the individual cells, the crystals can be oriented to a designated form, and thus, the polarization of the incident beam is varied spatially, resulting in CVB. If the flexibility in wavelengths is not an issue, CVB can be generated from linear polarized light by a special arrangement of $\lambda/2$ wave plates. Gluing four [25, 26] or eight [27] segmented $\lambda/2$ plates with discrete angles, the basic CVB azimuthally polarized laser beam (APLB) and radially polarized laser

beam (RPLB) can be obtained. However, due to the structural discontinuity at the edges of the segments, different higher order modes are generated of which the undesired modes have to be removed. This mode cleaning can be done either by a pinhole [26, 28] or by a near-confocal Fabry-Perot interferometer [17]. The principle of function of a four-segments mode converter is shown in Figure 3. Basically, an azimuthally or radially polarized laser beam is obtained by combining the TEM_{10} and TEM_{01} modes in the following way [28]:

$$AP = -HG_{01}n_x+HG_{10}n_y \quad (2)$$

$$RP = HG_{10}n_x+HG_{01}n_y. \quad (3)$$

A further superposition of RPLB and APLB results in the formation of a generalized CVB, which is described nicely in the papers of Zhan and co-workers [29, 30].

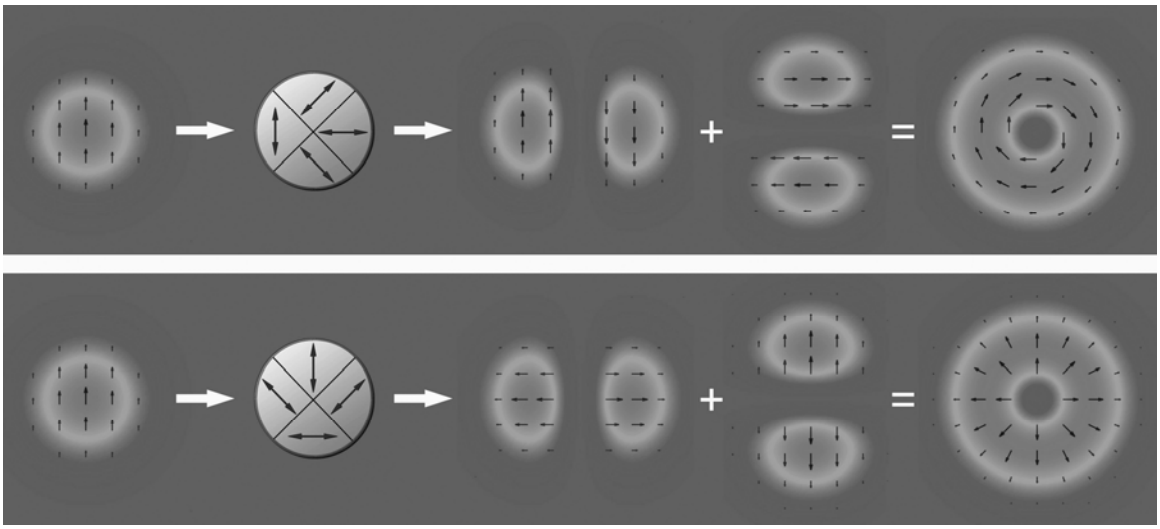

Figure 3. Scheme of APLB and RPLB generation: a mode-converter fabricated by four half-wavelength plates transforms a linear polarized Gaussian beam into the two orthogonal first-order Hermite-Gauss modes, which combine to the ring-shaped higher order modes. Depending on the position of the half-wavelength plates either an azimuthally or radially polarized laser beam is generated.

Although both beams show in free propagation all polarization states in the *x*/*y*-plane perpendicular to the propagation direction *z*, their behavior changes when they are focused. While the APLB contains only the in-plane (*x*/*y*) polarization components of the electrical field (Fig. 4), the RPLB has an additional field component in the *z*-direction (Fig. 5).

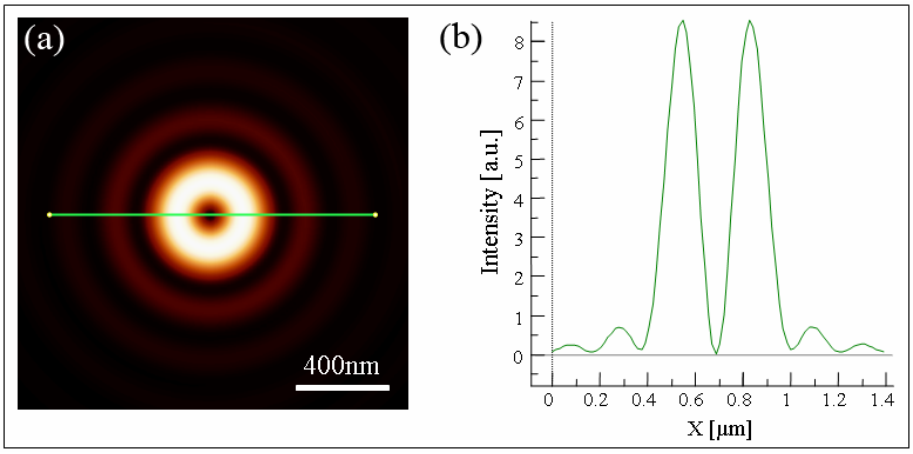

Figure 4. (a) Calculated field intensity distribution of an azimuthally polarized laser beam focused by a microscope objective lens (NA=1.25) onto a glass substrate; (b) cross-section of this field intensity distribution thought the center of the focal spot (green line). The distribution in the focus contains only the in-plane component of the field.

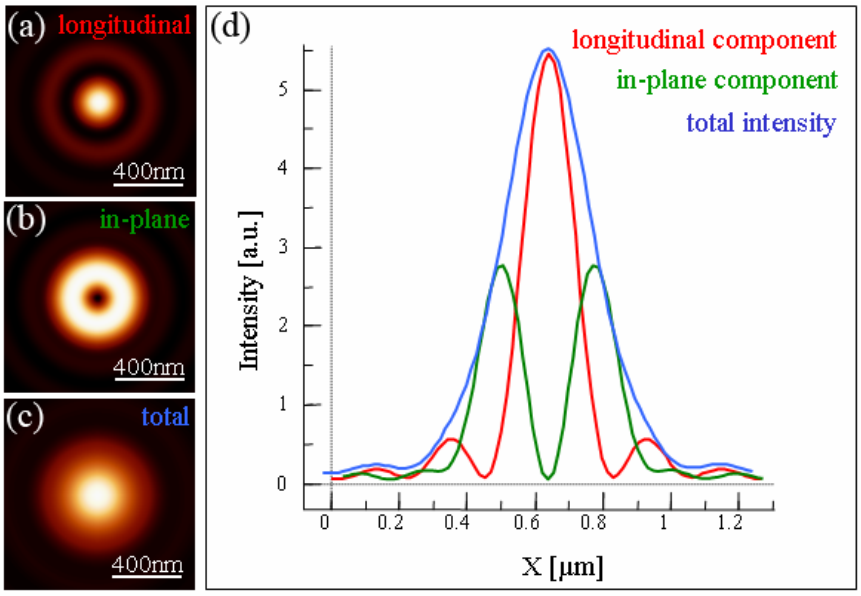

Figure 5. (a), (b), (c) Calculated field intensity distributions of the longitudinal, in-plane components and the total intensity of a radially polarized laser beam focused by a microscope objective (NA=1.25) onto a glass substrate, respectively; (d) cross-sections of the field intensity distributions thought the center of the focal spot. The total distribution in the focus contains the longitudinal and in-plane components of the field.

The interaction of these doughnut modes with the dipole moment of a single quantum emitter will be discussed in details in chapter 2.5. An APLB possesses an electric field distribution in the focus with polarization components oriented only in the focal plane. As the fluorescence rate R_f of a molecule depends on the projection of the excitation dipole moment $\vec{\mu}$ on the electric field strengths $\vec{E}$ according to $R_f \sim \left| \vec{\mu} \cdot \vec{E} \right|^2$, the obtained excitation pattern shows always a double-lobe pattern with vanishing intensities the further the dipole is oriented out-of-plane (Fig. 6a). The axis of this double-lobe, given by the dark gap separating the bright lobes, represents the projection of a single emitters TDM, which is indicated by the arrows in Figure 6c. As the dipole vector has always the same lengths, its projection length depends on the out-of-plane orientation. The axis of this double-lobe defines the in-plane orientation φ.

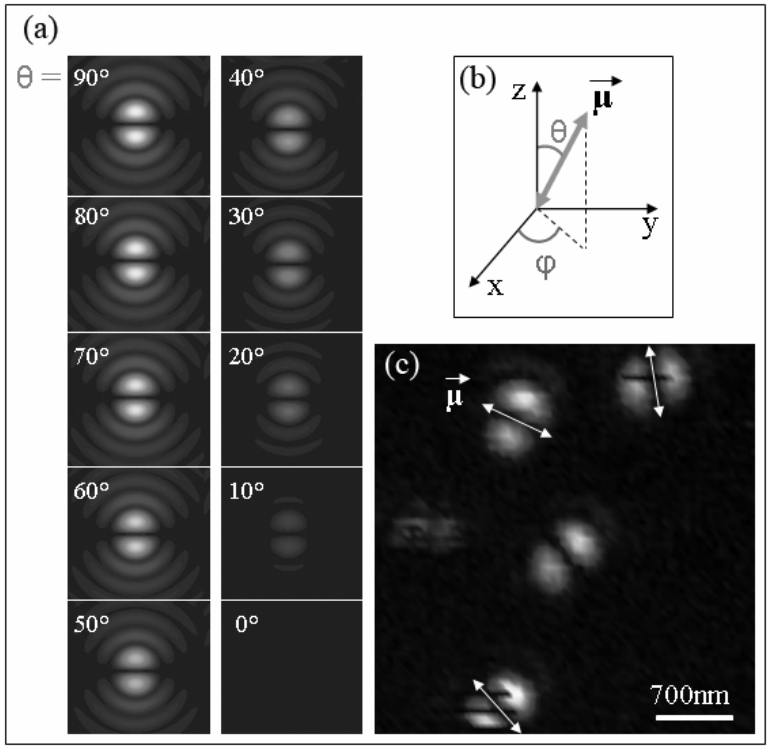

Figure 6. (a) The calculated fluorescence patterns for different θ angles (φ = 90° = const) of single quantum emitter with linear TDM $\vec{\mu}$ excited with an APLB. (b) The coordinate system according to which the angle values for the TDM orientations are given. (c) The excitation fluorescence patterns of four single R6G dye molecules excited with APLB. The arrows indicate the orientation of the TDM projection on the sample surface.

The RPLB has in addition to the in-plane polarization component also the longitudinal component (z-direction), and thus, the resulting excitation patterns have shapes ranging from spot-like to double-lobe patterns, depending on the three-dimensional orientation of the TDM of the quantum emitter. As it can be seen from the calculations presented in the Figure 7, a double-lobe pattern arises from a dipole in the focal plane and changes to a spot-like pattern for a dipole oriented perpendicular to this plane.

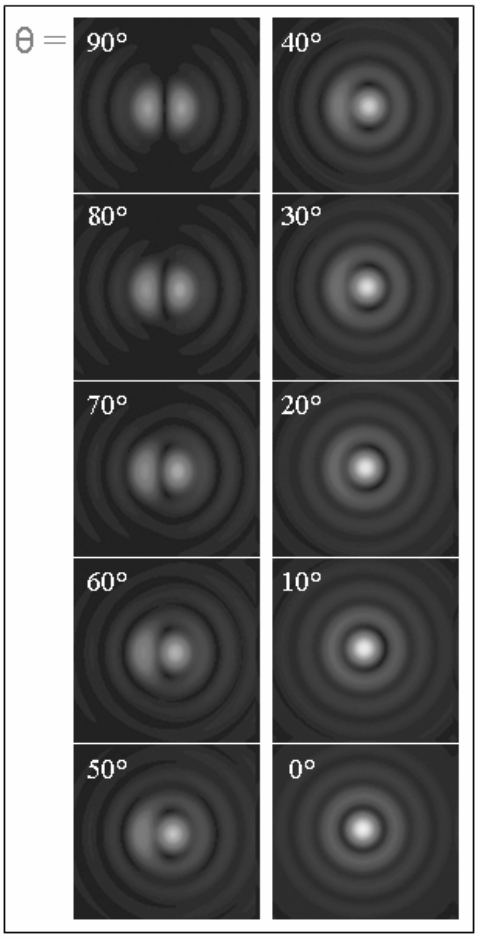

Figure 7. The calculated fluorescence patterns for different θ angles (φ = 90° = const) of single quantum emitter with linear TDM $\vec{\mu}$ excited with an RPLB. The coordinate system according to which the angle values for the TDM orientations are given is shown in Fig. 6b.

In the following, the recorded patterns are termed excitation patterns although the fluorescence is detected. This expression is chosen as the focal spot of the laser beam

with a diameter of ≈450 nm is much larger than the quantum emitter to be excited (several nm). Thus, the quantum emitter is excited by different parts of the doughnut beam during raster scanning, and therefore can only emit if it is excited by the correct polarization, i. e. coincides with the emitter's TDM orientation.

Based on this consideration, confocal images of single molecules are now compared with the theoretical prediction and their three-dimentional orientation can be determined (see Fig. 8). The presented examples show polymer-embedded PI ((perylene derivative (N-(2,6-diisopropylphenyl)-perylene-3,4-dicarboxymide) dye molecules, which were excited by a RPLB at a wavelength of 488 nm. The figures show that the experimental recorded pattern is also changing its shape from the double-lobe pattern to the spot-like shape.

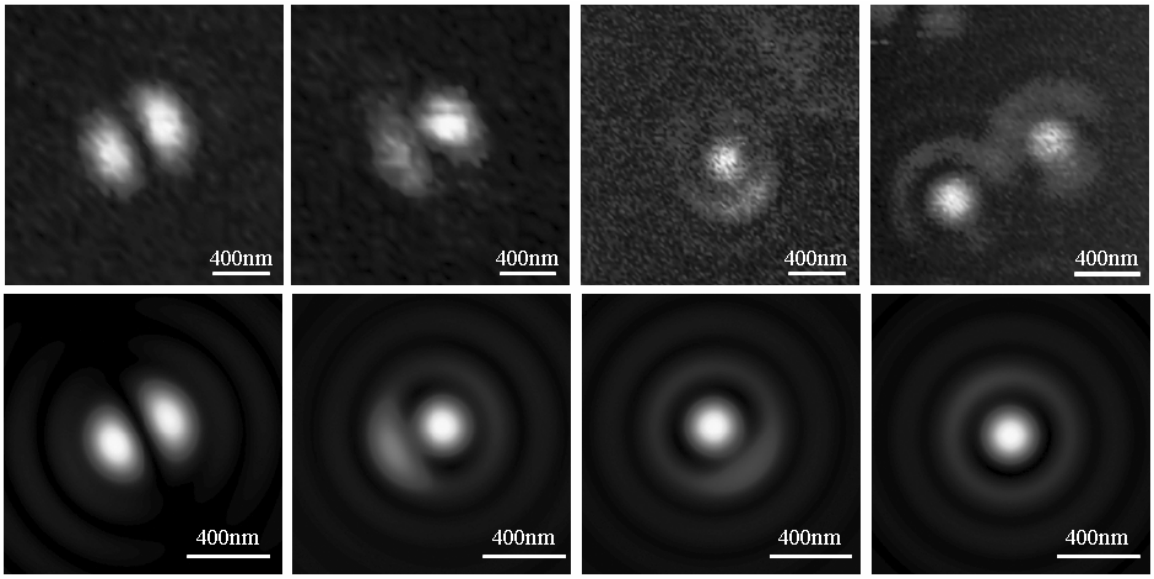

Figure 8. Experimental (upper row) and the corresponding calculated (lower row) excitation patterns of five PI molecules resulting from illumination with a RPLB. The corresponding θ/φ angles are: 85°/295°, 60°/115°, 40°/220°, 15°/47°, where φ = 0° is in *x*-direction (see Fig. 6b).

2.3 Imaging of the Single Quantum Emitters Using Linearly Polarized Laser Beam

When for the excitation the linearly polarized laser beam is used, then from the shape of the fluorescence patterns of the single quantum emitters it is not possible to

determine the orientation and the dimensionality of the excitation TDM. The field intensity distribution of a focused by a microscope objective lens (NA=1.25) linearly polarized Gaussian beam has two components, weak longitudinal component (Fig. 9a) and strong in-plane component (Fig. 9b). The longitudinal component can be neglected, since its intensity is approximately 13 times less than the intensity of the in-plane component. The total field intensity distribution is similar to the intensity distribution of the in-plane component and has one maximum (Fig. 9c). The fluorescence patterns of single quantum emitters, e.g. molecules or nanoparticles, after the excitation with linearly polarized laser beam have shape like a bright spots (Fig. 9d). The intensity of the patterns depends on the orientation of the TDM with respect to the sample surface, since field intensity distribution has only strong in-plane component, and also depends on the angle between the polarization direction of the laser beam and direction of the TDM (the intensity of the fluorescence pattern is higher when the angle is smaller).

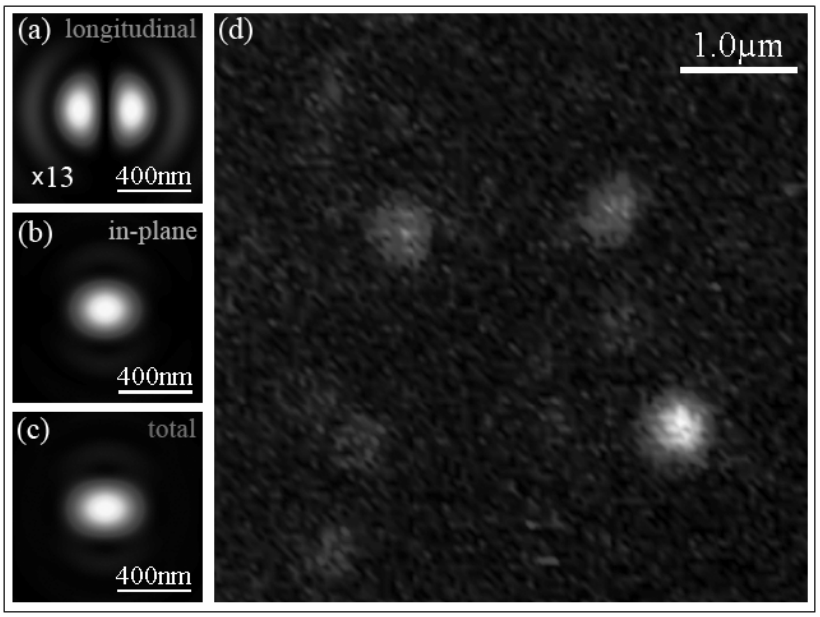

Figure 9. (a), (b), (c) Calculated field intensity distributions of the longitudinal, in-plane components and the total intensity of a linearly polarized laser beam focused by a microscope objective (NA=1.25) onto a glass substrate. The total distribution in the focus contains the longitudinal and in-plane components of the field. (d) The excitation fluorescence patterns of single CdSe/ZnS quantum dots excited with linearly polarized laser beam.

2.4 Imaging of the Fluorescence Spheres Using Higher-Order Laser Modes

The quality of the laser modes is examined by imaging these higher order laser modes with fluorescent spheres. These nanometer-sized polystyrene spheres contain a large number of fluorescent molecules (~ 200), where the individual molecules have random orientation (Fig. 10a). Thus, all polarizations of the excitation light are absorbed simultaneously by the molecules (in contrast to the interaction of these modes with a

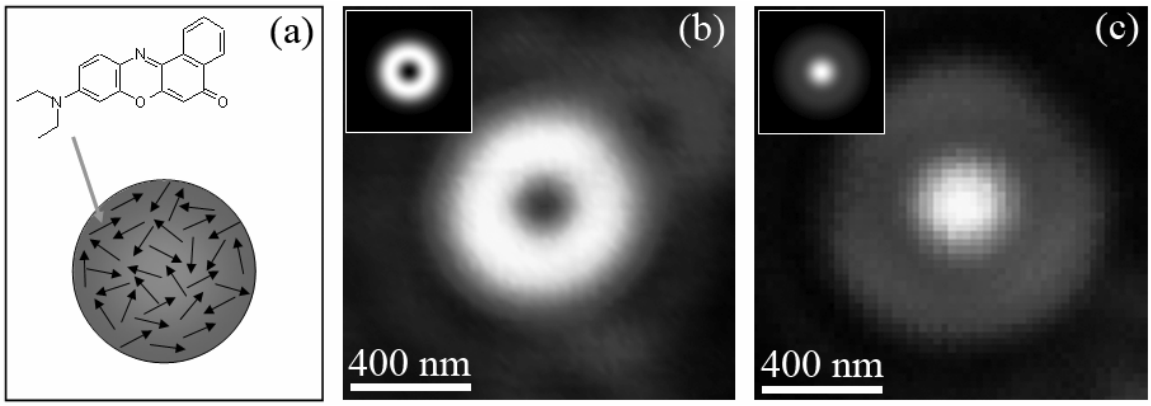

Figure 10. (a) The structure of the fluorescence Nile Red sphere. (b) and (c) the fluorescence images of the single sphere excited with an azimuthally and radially polarized laser beam, respectively. The insets show the corresponding calculated intensity distribution.

single transition dipole of one distinct emitter). Therefore, the scan image is a measure for the electric field distribution in the focus of the excitation beam. The spheres purchased by Molecular Probes (Leiden Netherlands) have a diameter of 20 nm and are loaded with Nile Red molecules (Fig. 10a). To align the modes, a diluted solution of the spheres in water/PVA (polyvinyl alcohol, $(C_2H_4O)_n$) was spin coated on a glass substrate. For this experiment either a 488 nm or 514 nm laser was used to excite the dye. The scan images in Figure 10b and 10c show the results of the interaction of an azimuthally and a radially polarized laser with an isotropic emitter.

In the focus of an APLB the electric field vectors in the focal area are entirely polarized parallel to the surface, exactly like the far field intensity distribution of the beam. Thus, a perfect ring-shaped pattern appears when an isotropic emitter is scanned through the focus of an azimuthal mode. The experimentally obtained scan image and the

corresponding calculated pattern is shown on the left side in Figure 10b. In turn, the focus of a radial mode consists of a very strong field polarized perpendicular to the surface, which is much stronger than the ring of parallel polarized electric field vectors around it. As a consequence, one can see in the right scan image (Figure 10c) mainly the interaction with the strong perpendicular field in the center.

2.5 Imaging of the Single Molecules Using Higher-Order Laser Modes

First we will present quantum emitters with a linear TDM. For this purpose, we investigated stopcock molecules (tetra-phenyl-porphyrin: SC-TPP), which consist of a head (porphyrin based structure) and a tail (alkoxy chain). These molecules find their application within the research of host-guest-compounds [31, 32], see chapter 8 for the details. These compounds can be made of organic or inorganic crystals (host) exhibiting hollow channels to include the guest material, e. g. chromophores. The function of the stopcock molecules is to close the channels and avoid out-diffusion of the guest material [33].

Figures 11a and 11b show the fluorescence images of five single stopcock molecules excited with azimuthally and radially polarized doughnut modes, respectively. The excitation wavelength is 488 nm. Since the molecules possess a linear TDM, excitation with an APLB results in double-lobe patterns (Fig. 11a). As described in section 2.2, the projection of a single molecule's TDM is parallel to the dark gap as indicated by the arrows for molecules A, E, and D of Fig. 11a. The intensity of the pattern in the case of excitation with an APLB mainly depends on the following parameters: out-of-plane orientation of the TDM (see also Fig. 6 in section 2.2), the depth position of the molecule in the polymer layer (in the case of the excitation with RPLB) [5], quantum efficiency of the molecule, the local environment. However, if molecules of identical chemical structure are fixed in a polymer matrix (in this case PMMA), the intensity of single molecule images exhibits good correlation with the tilt of the TDM.

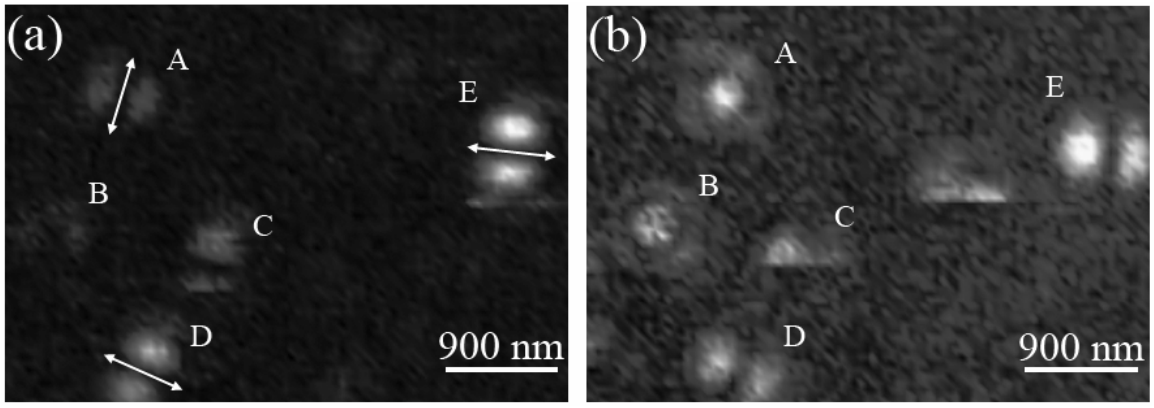

Figure 11. Fluorescence patterns of the same five single dye molecules excited with azimuthally (a) and radially (b) polarized laser beam. The white arrows indicate the orientation of the TDM projection on the sample surface.

In particular, the molecules possessing horizontally or nearly horizontally oriented TDM, typically show the highest excitation efficiency (Fig. 11a, molecule D and E). Molecules with vertically oriented TDM cannot be excited with APLB at all, hence will not show any emission (in Fig. 11a, molecule B). Different tilt angles θ (see Fig. 6) of the molecule's TDM will lead to different intermediate intensities (Fig. 11a, molecules A, C). In addition, one can see in this scan image the bleaching behavior of molecules, e. g. in C, which is an indication that single molecules were investigated.

Subsequent to the APLB excitation the same sample area has been investigated by excitation with a RPLB, which consists of both, in-plane and longitudinal field components. Thus, in case of a horizontally oriented TDM the molecule interacts only with the in-plane field component of the RPLB, and we will observe the same double-lobe pattern as in the previous case, but turned by 90° (Fig. 11b, molecule D). However, if the TDM is oriented vertically (Fig. 11b, molecule B) or nearly vertically (Fig. 11b, molecule A), the resulting image has the shape of a spot with a weak ring around. This difference in the shapes of the patterns is due to the fact, that vertically oriented TDM can be excited only with the longitudinal field component of the RPLB. The molecules with a TDM in positions in between, i. e. tilted by the angle θ, will result in different non-symmetric shapes (for example Fig. 11b, molecule E). Then the three-dimensional orientation of the transition dipoles can be obtained by analyzing the recorded excitation patterns with respect to the calculated patterns (see Fig. 7).

Thus, the technique of CVB provides us the complete information about the spatial orientation of the excitation transition dipole of a single quantum emitter. Additionally, it is possible to distinguish between a one-dimensional (linear) excitation TDM (e. g. molecules) or three-dimensional excitation transition dipole moment (e. g. spherical CdSe/ZnS or Si/SiO_2 quantum dots, chapters 4 and 7). However, so far no conclusion on the parameters of the emission dipole moment can be made. For this purpose, we combine the higher order laser modes for excitation with the well-known method of polarization microscopy [3, 10], where an analyzer is placed in front of the detector (here an APD).

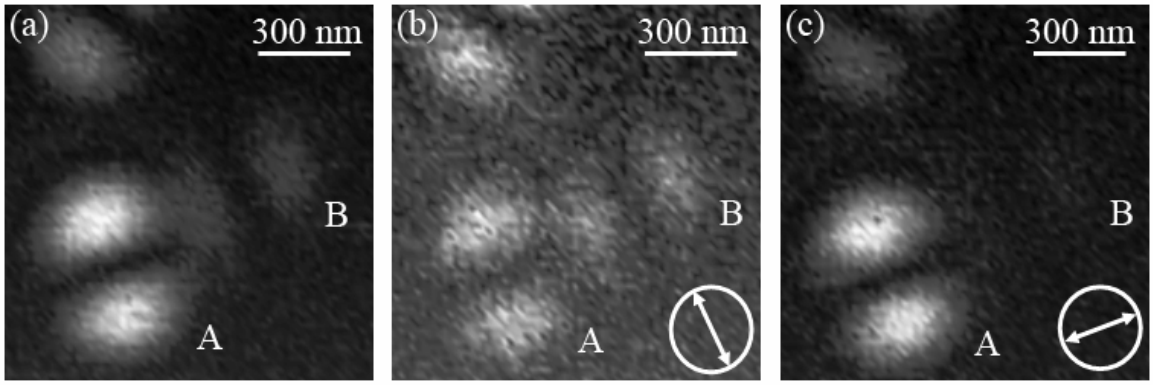

Figure 12. Three single PI molecules excited with APLB: (a) without linear polarized in front of the photodetector; (b) and (c) with linear polarizer in front of the photodetector oriented according to the arrow.

By recording a series of images of the emitters with different orientations of the polarizer a direct relation between the absorption dipole orientation and the emission dipole orientation can be obtained. Corresponding to this method Figure 12 shows three images of single dye molecules (PI) fixed in a polymer matrix and excited with APLB. Without the linear polarizer (Fig. 12a) the intensities of the single molecule images correspond to the out-of-plane orientation of their TDMs. In particular, the weak intensity of molecule B gives evidence, that its TDM is oriented nearly vertical with respect to the sample surface, while molecule A is aligned nearly horizontally. When the linear polarizer is placed in front of the APD according to the orientation of the arrows shown in the images (b) and (c), only the emission possessing the selected orientation of the polarization plane will be detected. We see that the maximum emission from a single

molecule is detected when the linear polarizer is parallel to the dark gap of the double-lobe image, i. e. to the excitation dipole. At the same time, when the polarizer axis is nearly perpendicular to the excitation dipole, the single molecule emission detected by the APD dramatically decreases (Fig. 12b, molecule A) or completely vanishes (Fig. 12c, molecule B). Thus, the combination of CVB and classical polarization microscopy technique gives us the important result that the emission and excitation dipoles of this type of dye molecule are parallel.

2.6 Summary and Conclusion

We presented the use of cylindrical vector beams to determine the three-dimensional orientation of linear TDM of spatially isolated and immobilized single molecules. An inverted confocal microscope was used to investigate the samples. The recorded excitation patterns are compared with the corresponding calculated patterns, and thus, the orientation information is revealed. As the APLB possesses only in-plane field components, it is more suitable to use a RPLB for the 3D TDM orientation. In this mode in-plane as well as longitudinal polarization components can be used to probe the emitters TDM orientation. We have demonstrated the use of these two different cylindrical vector beams for PI molecules as well as for stopcock molecules.

3 Imaging of the Excited-State Tautomerization in Single Metal-Free Phthalocyanine and Porphyrin Molecules

*Tautomerism of single fluorescent molecules was studied by means of confocal microscopy in combination with azimuthally or radially polarized laser beams. During a tautomerism process the transition dipole moment of a molecule changes its orientation which can be visualized by the fluorescence excitation image of the molecule. In this chapter we present experimental and theoretical studies of a symmetrically substituted metal-free phthalocyanine (**1**) and porphyrin (**2**).*

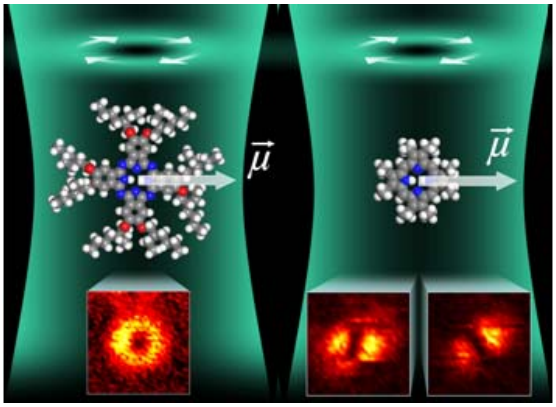

This chapter is based on:

A. M. Chizhik, R. Jäger, A. I. Chizhik, S. Bär, H.-G. Mack, M. Sackrow, C. Stanciu, A. Lyubimtsev, M. Hanack, A. J. Meixner, "Optical imaging of excited-state tautomerization in single molecules", *Phys. Chem. Chem. Phys.*, **13,** 1722-1733, **2011**. link to article page

Quantum chemical calculations were carried out by Dr. H.-G. Mack (Tübingen University).

3.1 Introduction

Tautomerization is a basic chemical process, gaining interest of researchers since several decades. Specific chemical and especially biochemical reactions require a modification in the constitution of the involved molecules. Prototropy is the most important tautomerism process, which occurs in nature. Many porphyrin derivatives can be found in a complex bound to a metal ion, e.g. in hemoglobin for oxygen transportation or in chlorophyll for photosynthesis. Phtalocyanines are widely used as blue or green pigments for ink- and laser-printers and like porphyrazines and porphyrins in the photodynamic tumortherapy (PDT) [34-38]. Moreover, light-induced tautomerization can be used for information storage in holography [39]. Porphyrins serve as biomimetic models for enzymes, for catalytic reactions, as well as sensors and biosensors [40]. For the investigation of the tautomerism process porphyrin molecules can be considered as a basic matrix for the prototropy, since it proceed isolated in the inner ring of the symmetric structure of the porphyrin.

Tautomerism processes have been intensively studied by nuclear magnetic resonance (NMR) analysis [41, 42], combined with isotope markers, insertion of different substituents to investigate the tautomerism process in porphyrin-systems in solutions as well as in crystals at low and high temperatures [43-48]. Remarkable, that NMR studies provide information only of the ground state tautomerism process. Other spectroscopic methods, such as fluorescence spectroscopy [49], polarization spectroscopy [50, 51], as well as influences of excitation by studying near-infrared two-photon absorption spectra [52] and other experiments involving excited states concerning photoisomerism [53, 54] have also been used to investigate the tautomerisation. In agreement with experimental results, theoretical studies of porphyrin molecules and their derivatives revealed two possible intra-molecular processes: a synchronous hydrogen movement, i.e. transition between two trans states, or a step-wise transition through a cis tautomer [42, 43, 55]. Previous researchers showed that one of the inner hydrogens can move and form the cis tautomer [41, 46-48, 53, 54]. Afterwards the initial trans form can be reproduced again or the other hydrogen can change its position relaxing into the chemically identical trans tautomer, but with different position of the hydrogen atoms. Nevertheless, these methods can provide only averaged information for an ensemble of molecules.

The combination of confocal microscopy with cylindrical vector beams (APLB and RPLB) is widely used for the investigation of single quantum emitters. This method provides information about the excitation transition dipole moment (TDM) while other microscopy techniques, e.g. defocusing imaging [1, 2] or polarization microscopy [3], provide information about the emission TDM. The knowledge of the orientation of a molecule's TDM is directly related to the orientation of the molecule. Thus, the relative position of a certain molecule with respect to the sample plane can be obtained. The optical imaging of the excitation patterns has already been employed to the analysis of tautomerization in single porphycene molecules by Piwonski et al [14, 15]. Since the trans forms are chemically and magnetically equal, the single molecule confocal microscopy provides new insight into the excited-state tautomerism process, while other techniques are not able to discriminate between these two forms.

In this chapter we show new results on the experimental and theoretical investigations of the tautomerism process in a symmetrically substituted metal-free phthalocyanine (H_2Pc) and a symmetric octaethylporphyrin (OEP). The single molecule studies have been carried out using higher order laser modes (APLB and RPLB) [4, 9-12, 17, 56], in combination with confocal microscopy [29, 30]. This method allows us to do imaging of the tautomerism process at the single molecule level and moreover, to determine the three-dimensional orientation of the molecule's TDM upon its reorientation due to the tautomerism process by comparing experimental and simulated excitation patterns. The molecules were investigated on glass cover slides, in a polar or nonpolar polymer matrix to exclude movement, rotation or any effects of the polarity. We have found that the phthalocyanine molecules exhibit the tautomerism process, which results in fast switching (faster than the scan speed in the optical measurements) between two orientations of the molecule's TDM. Whereas most of studied OEP molecules showed the absence of the tautomerism process, 7% of the total number of the molecules exhibited a slow switching between the two trans forms. Thus, for the first time, by imaging the orientation of the single molecule TDM we separately observed the two different trans forms. These findings give us a new insight in the excited-state tautomerism process and are of fundamental importance for further applications.

3.2 Experimental

Synthesis of the molecules: The symmetrically substituted metal-free phthalocyanine (**1**) and porphyrin (**2**) (Fig. 13) were synthesized according to published procedures [57, 58].

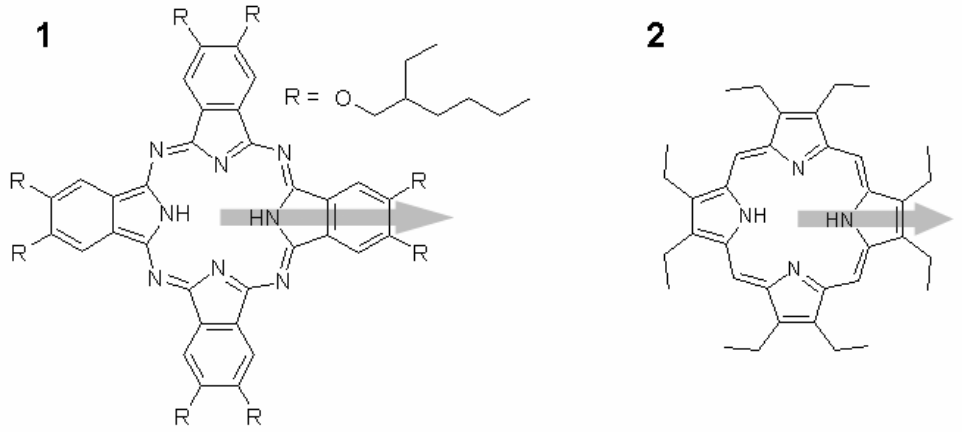

Figure 13. 1: symmetrically substituted phthalocyanine (H_2Pc); **2:** symmetrically substituted porphyrin (OEP). The arrows indicate the calculated transition dipole moments $\vec{\mu}$ for the $S_0 \rightarrow S_1$ transition of the respective trans tautomers.

Computational details: The quantum chemical calculations were carried out with the Gaussian 03 program [59]. Optimized geometries, vibrational frequencies and relative energies for the various tautomers were obtained at the B3LYP/6-311G* level of theory. All structures investigated represent minima on the corresponding energy hypersurface (i.e. possess no imaginary frequency). Calculations of the electric TDMs for the first excited electronic state S_1 were performed by applying the RCIS/6-311G*//B3LYP/6-311G* approximation. In the case of **1**, additionally the first order transition states (first imaginary frequency) for the tautomerism process trans-to-cis in the electronic states S_0 and S_1 were obtained. Geometry optimizations for the S_1 structures were performed applying time-dependent density functional theory (B3LYP-TD/6-311G*, see below).

Sample preparation for single molecules investigation: All samples with single H_2Pc and OEP molecules were prepared by the method of spin coating (see chapter 2.1).

Microscopy: Fluorescence imaging of the single H_2Pc and OEP molecules was performed with the experimental setup sketched in Fig. 1 and described in chapter 2.1.

3.3 NH Tautomerization

The molecules, are excited either to a vibronic level, located lower the barrier (Fig. 14, (1)), separating the trans tautomers from the cis form, or higher (Fig. 14, (2)). In the first case the molecule recombines to the ground state within the same trans tautomer. In the second case it reaches the level, possessing higher energy than the barrier between the different tautomers, it can transfer to the excited state of another trans form, which leads to recombination to the respective ground state.

Two mechanisms of the tautomerism process (2) (Fig. 14) are proposed, a two-step and a single step. In the two-step mechanism, the two H atoms migrate one after another from the trans through a transition state to cis and a transition state to trans. The single-step mechanism involves synchronous migration of the two H atoms from trans to a transition state and trans. The transition state specified is characterized by no N-H bond, but where the two H atoms are equally shared between two N atoms (two intramolecular H-bonding), and corresponds to the concerted mechanism. According to quantum chemical calculations the two-step mechanism is preferred for H_2Pc as well as for OEP molecules [60-62].

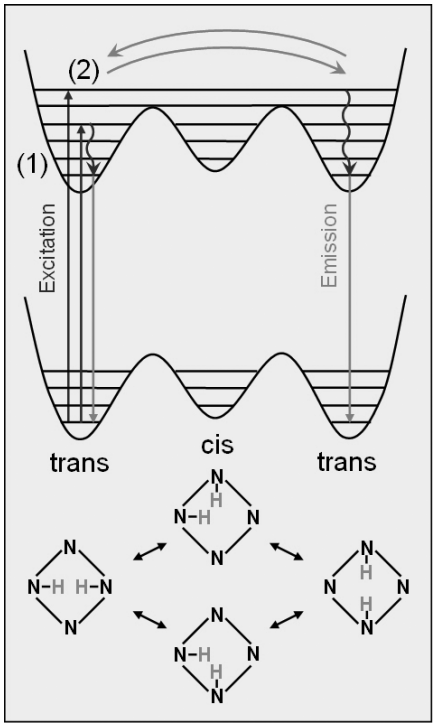

Figure 14. Scheme of the excited-state tautomerism process.

3.4 Simulated Excitation Patterns for Different Angles between Two Dipoles and Different Orientation of the Molecule

Scanning a single molecule with a distinct orientation of its TDM through the focal region of an APLB results in a characteristic double lobe excitation pattern. This pattern (Fig. 15e) is given by the projection of the incident field $\vec{E}$ onto the direction of the transition dipole moment $\vec{\mu}$, since the detected fluorescence intensity is proportional to $\left| \vec{\mu} \cdot \vec{E} \right|^2$. If the orientation of the TDM changes due to the tautomerism process faster than the acquisition time of one line-scan of the image, a pattern results in a superposition of double lobe patterns for the respective orientations of their TDMs. Assuming the change in orientation is 90°, the excitation pattern in the scan image would have a donut-like shape as depicted in Fig. 15h. If the angle between the orientations is different from 90°, the donut degenerates towards an asymmetrical intensity distribution depicted in Fig. 15f, g. Hence, by fitting such theoretical patterns to the measured fluorescence excitation patterns, the angle enclosed between the TDMs for the two tautomeric forms could be determined for every molecule. However, the accuracy of such an analysis depends on the quality, i.e. the signal-to-noise ratio of the experimental data. Comparing our measurements with the theoretical simulations it is possible to clearly distinguish between double-lobe patterns or donut patterns if the angle between the transition moments is between 60° and 120°.

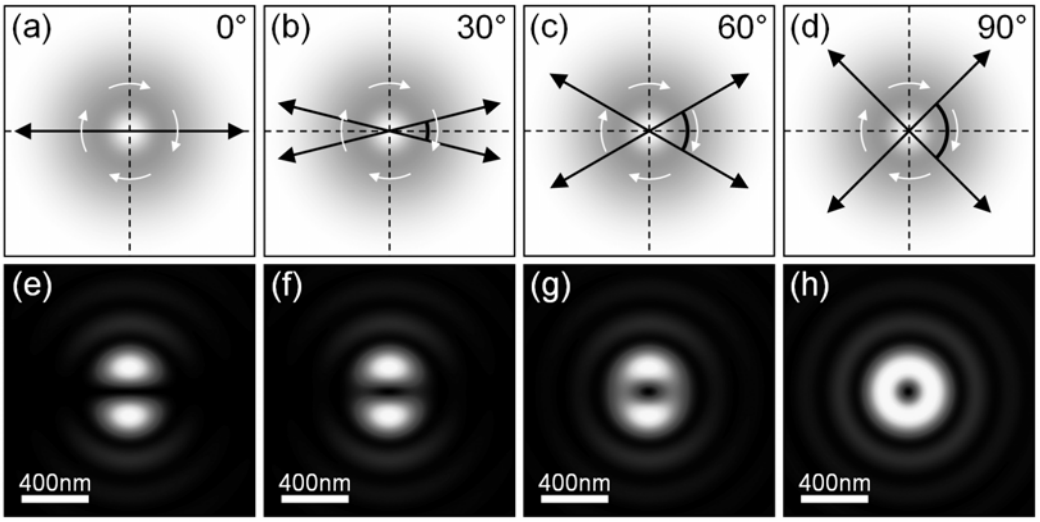

Figure 15. (a)-(d) Scheme of two transition dipole moments (shown as black arrows), lying in the plane of the sample surface, turned at different angles with respect to each other in the focal area of an APLB focused with a high numerical aperture objective lens or parabolic mirror (direction of the light polarization is shown with white arrows). (e)-(h) Calculated excitation patterns for the superposition of two transition dipole moments with different angles in between, according to schemes (a)-(d), respectively.

Now, assuming that the tautomerism process results in a change of the orientation of a molecule's TDM by 90° we would like to consider how the shape of a single molecule pattern is modified upon the change of the molecule's orientation with respect to the sample surface (Fig. 16a, d). According to this condition, Fig. 16e shows for an APLB a simulated excitation pattern of a horizontally oriented molecule undergoing fast tautomerism process. The ring-shaped pattern is a result of the superposition of two double lobe patterns, turned at an angle of 90° with respect to each other. If the molecule is oriented vertically with respect to the sample surface, both projections of the molecule's TDMs on the sample surface are parallel to each other. In this case when the molecule is excited with an APLB, it exhibits the same excitation pattern, as in the case of the fixed linear TDM (i.e., a double lobe pattern, Fig. 16h). If the molecule is tilted, the pattern shows a quazi-ring shape (Fig. 16f, g), which varies depending on the particular orientation.

However, the double lobe pattern can be observed not only in the case of the vertically oriented molecule with fast tautomerization, but also in the absence of the

tautomerism process. Recording the excitation patterns of the molecule, excited with a RPLB, which possesses a longitudinal field component, allows one to distinguish between these two cases. A pattern of the vertically oriented molecule with fast tautomerism process, excited with a RPLB, exhibits a prolate spot, in the center of weaker rings (Fig. 16l) which can not be observed upon excitation of the molecule possessing a fixed linear TDM. Horizontally oriented molecules can be excited only with the in-plane field component, therefore, the pattern exhibits a similar donut-like shape (Fig. 16i), as in the case of the excitation with an APLB. The molecules, which are tilted with respect to the sample surface, show different intermediate asymmetric shapes either resembling a ring-structure (Fig. 16j) or a prolate spot (Fig. 16k) depending on the particular orientation.

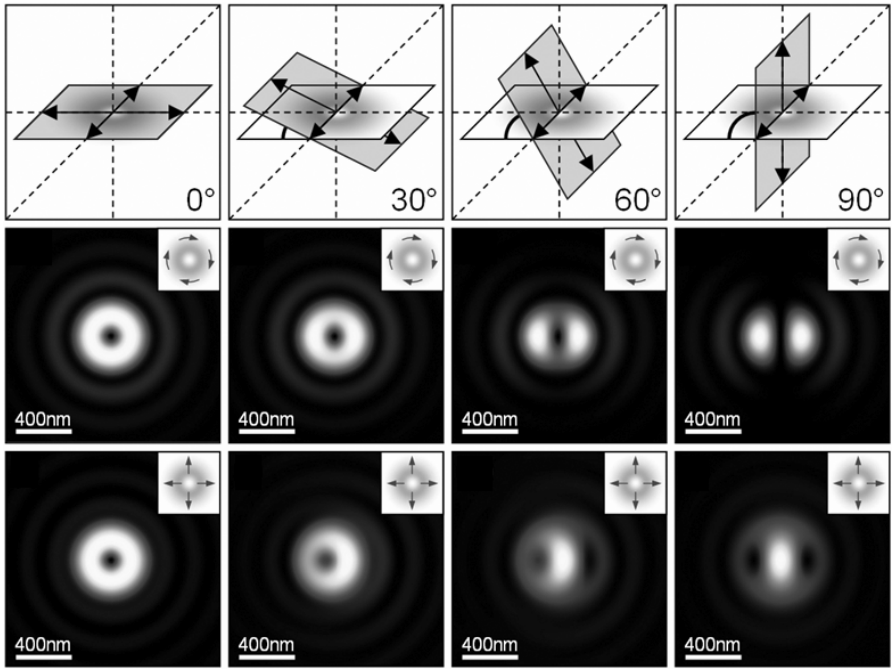

Figure 16. (a)-(d) Scheme of the molecule possessing two orthogonal transition dipole moments, lying in the plane, showed with blue plane. The molecular plane exhibit different orientation with respect to the sample surface (white plane). Simulated excitation patterns of a single molecule possessing two orthogonal transition dipole moments as a result of the tautomerism process upon excitation with an azimuthally ((e)-(h)) or radially ((i)-(l)) polarized laser beams focused with an objective lens. The molecule is oriented according to scheme (a)-(d).

3.5 Imaging of the Tautomerism Process in Single H_2Pc Molecules Using Higher Order Laser Modes

Phthalocyanine (H_2Pc) **1** (Fig. 13) is symmetrically substituted with ether groups [57]. The ether groups efficiently prevent aggregation in solution and on surfaces, confirmed by the analysis of position, half-width and shift of the Q-band components in its UV/Vis absorption spectrum [57]. The position of the two inner ring protons in **1** defines two equivalent tautomeric trans forms for the isolated molecule.

In the electronic ground state, according to the B3LYP/6-311G* calculations, the cis tautomer is 40.2 kJ/mol higher in energy than the trans form and the barrier for trans-to-cis tautomerization is near 58.6 kJ/mol. These values only slightly change for the corresponding structures in the S_1 state (B3LYP-TD/6-311G*), that is, in both states the trans tautomer is predicted to be more stable than the cis form.

Quantum chemical calculations (RCIS/6-311G*//B3LYP/6-311G*) show that the angle between the TDMs of the two trans tautomeric forms of **1** is 90°. Therefore, at room temperature tautomerization changes the direction of the TDM much faster than the scan speed in the optical measurements (5 ms per image pixel and 400 s per image). Figure 17 shows the molecules excited with an APLB which exhibit both donut shape patterns and double lobe patterns (in white dashed circle), suggesting that the orientation of the molecule is close to vertical. To determine the 3D orientation of the molecules we used a radially polarized laser beam for the excitation [4, 11]. Figure 18 shows the experimental and simulated fluorescence patterns of two H_2Pc molecules excited with APLB and RPLB. According to simulations described in the section 3.4, we can assume, that molecules which possess double lobe fluorescence patterns after the excitation with an APLB, are oriented vertically with respect to the sample surface, while molecules which possess ring shape patterns – are oriented horizontally. And we can conclude that all investigated molecules undergo fast 90° tautomerism process.

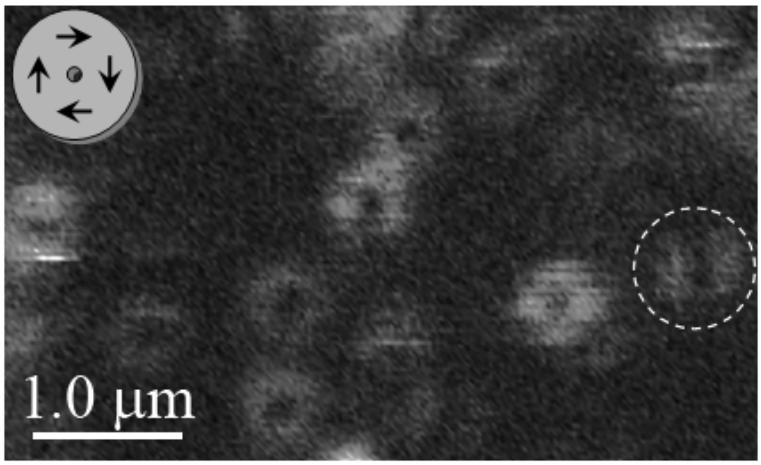

Figure 17. Fluorescence patterns of the single H_2Pc molecules embedded in the polymer matrix and excited with an azimuthally polarized laser beam. The molecule in the dashed circle shows double lobe patterns, while the rest of the molecules have donut-like patterns.

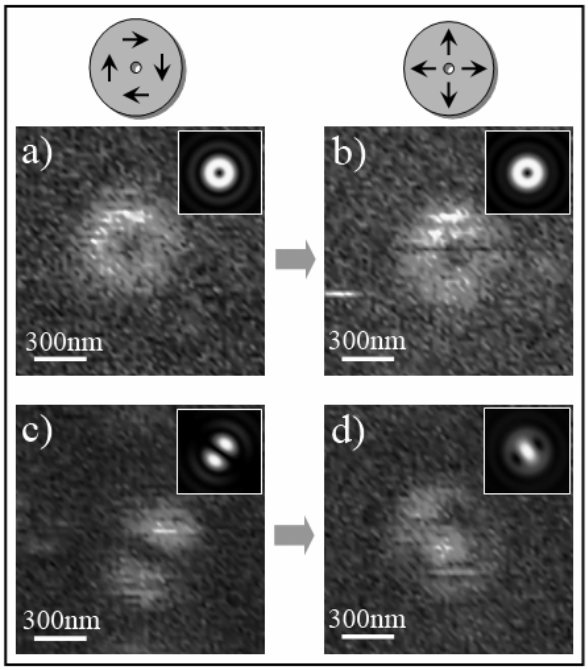

Figure 18. Fluorescence patterns of horizontally (a, b) and vertically (c, d) oriented H_2Pc molecules with respect to the sample surface, excited with azimuthally and radially polarized light, respectively. The insets show the corresponding calculated patterns.

3.6 Imaging of the Tautomerism Process in Single OEP Molecules Using Higher Order Laser Modes

The octaethylporphyrin (OEP) is a symmetrically substituted molecule (Fig. 13). According to quantum chemical calculations the angle between the TDMs of the two trans forms of the OEP molecule is 90°. According to the B3LYP/6-311G* calculations the cis tautomer is about 37.6 kJ/mol less stable than the trans structure, therefore, the molecule in the electronic ground state S_0 can only be in one of the two trans forms. And for this reason, the molecule can be excited only from one of the chemically equivalent trans tautomers.

In contrast to the investigated H_2Pc molecules, OEP molecules show no ring-like shaped patterns after the excitation with an APLB. Most of the investigated molecules exhibit stable double lobe fluorescence patterns, while only 7% of the molecules show flipping of the TDM. In Fig. 19 a series of fluorescence images of four single OEP molecules excited with an APLB is presented. The images were recorded one after the other. The molecule in the white dashed circle shows a sudden change of the TDM orientation during the scan (Fig. 19b), while the other molecules possess stable excitation TDMs. Two arrows in the Fig. 19b show where the TDM of the molecule flipped from one orientation to another, i.e., the molecule switched between two trans tautomers. From the image we estimated that the time, when the molecule was in the same trans form (the central part of the pattern between the arrows) is 36 s. In Fig. 19c the molecule has the original TDM orientation like in Fig. 19a.

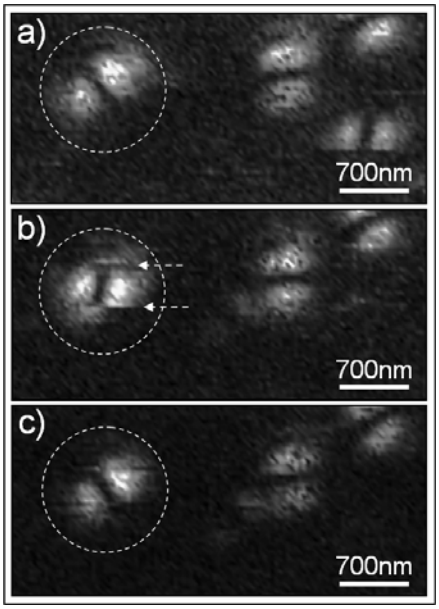

Figure 19. (a)-(c) Images of single OEP molecules embedded in a PMMA matrix and excited with an azimuthally polarized laser beam; the images were recorded one after the other. The molecule in the white dashed circle shows a change of the TDM orientation. The acquisition time of one image is 400 s. The scan direction is top-down. Image (b) shows the sudden flipping of the TDM, caused by the transition of the molecule from one trans form to another. Two arrows show the part of the image (corresponds to 36 s acquisition time), where the molecule possesses a fixed orientation of the TDM, i.e., stays in the same trans form.

Since the OEP molecule can be excited only from one of the trans structures (but not from the less stable cis form), the excitation pattern reflects the orientation of the TDM of the molecule in the trans forms. The angle between two TDM orientations of the molecule in the white circle (Fig. 19a and 19b) is less than 90°, which is different from the result of the quantum chemical calculations. This can be explained by the fact, that the pattern obtained upon excitation of the molecule by an APLB, shows the projection of the TDM on the sample surface. Therefore, if the molecule is tilted with respect to the sample surface, the angle between two projections of the TDMs of the molecule in the trans tautomers is less than 90°.

In Fig. 20 an image series of the same single OEP molecule excited with an APLB is depicted. The pattern in Fig. 20a demonstrates the flipping of the TDM during

the scan. The upper and the lower parts of the image correspond to the TDM orientation like in the Fig. 20b, while the middle part corresponds to the TDM orientation like in the Fig. 20c. Since the molecule can be excited only from one of the two trans forms, the measured patterns correspond to the different trans tautomers of the single molecule. The angle between the two TDM projections is nearly 90° (Fig. 20b and 20c), thus the molecule is lying parallel to the sample surface.

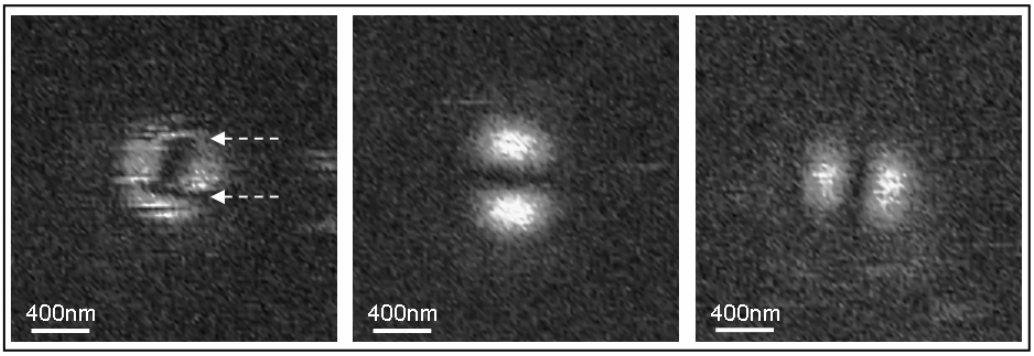

Figure 20. (a)-(c) The image series of a (same as in the text) single OEP molecule embedded in a PMMA matrix and excited with an azimuthally polarized laser beam; the pictures were recorded one after the other. The acquisition time of one image is 400 s. The scan direction is top-down. (a) The tautomerization occurs twice during the scan process. As indicated by the arrows, the central part of the image (corresponds to 30 s acquisition time) shows the fixed TDM orientation of the molecule in one of the trans forms. (b), (c) The excitation patterns of both trans forms of the same single OEP molecule.

Thus, for the first time we could observe, that a molecule undergoing a tautomerism process stays in one tautomeric trans structure during a time comparable with the acquisition time of one excitation pattern (i.e., near 400 s). This allowed us to visualize the existence of each of the two trans forms of a single OEP molecule, as well as the sudden switching between these tautomers. Such observations are impossible for molecules, where the switching between the trans structures occurs faster than the acquisition time of one line of the excitation pattern (for example, H_2Pc molecules).

We investigated molecules embedded in polar (PMMA) and nonpolar (PS) polymers directly spin coated on the surface of the cover slide and found qualitatively the same behavior.

3.7 Summary and Conclusion

In summary, we showed that cylindrical vector beams focused with a high NA objective lens can be used to image the tautomerism process in spatially isolated and immobilized single phthalocyanine (**1**) and porphyrin (**2**) molecules. This method allowed us to distinguish between the fast and slow (with respect to the acquisition time of one line-scan of the single molecule fluorescence image) tautomerism process at the single molecule level. Using a RPLB we determined the three-dimensional orientation of an individual molecule by comparing the experimental and simulated excitation patterns. The recorded excitation patterns exhibited the usual fluorescence dynamics such as blinking and bleaching, and clearly indicating that single molecules were studied. By comparing the experimental and simulated single molecule patterns upon excitation with an APLB we showed that the quantum chemical calculations are in a very good agreement with obtained results.

In particular, the phthalocyanine molecules **1** exhibited either donut-shaped excitation patterns, suggesting a fast tautomerism process between two trans forms with TDMs forming an angle of 90°, or double lobe patterns, corresponding to a tilted orientation of the molecule with respect to the sample surface.

Most of the investigated single porphyrin molecules **2** show a stable TDM and only for 7% of the total number of molecules a sudden flipping of the TDM orientation between two trans tautomers was observed. Thus, for the first time we are able to detect the two trans forms separately. According to the quantum chemical calculations, the angle between TDM orientations of the two trans forms is 90°. Therefore, the double lobe pattern, which was obtained upon excitation of 93% of the total number of the molecules with an APLB, can be observed either in the case of the absence of the tautomerization or in the rare case of a vertical orientation of the molecule with tautomerism process. We relate the absence of the tautomerism process (fixed orientation of the single molecule excitation pattern) to the following reasons: 1. The energy barrier between trans and cis forms is too high. Therefore, the molecule is always excited from the same trans form in the ground state. 2. The excitation energy 245 kJ/mol at the laser wavelength (488 nm) is not high enough to overpass the energy barrier between the two tautomeric forms in the excited state potential of OEP molecules. The absorption maximum of the OEP

molecules is at 400 nm. Assuming that the barrier between the trans and cis forms of the ground state is not higher than the barrier in the excited state, let us estimate the energy, which molecules **1** and **2** require for the excited state tautomerism process. It can be estimated as a sum of the barrier energy and the energy corresponding to the maximum of the most red-shifted band in the excitation spectrum of the molecules (Fig. 21).

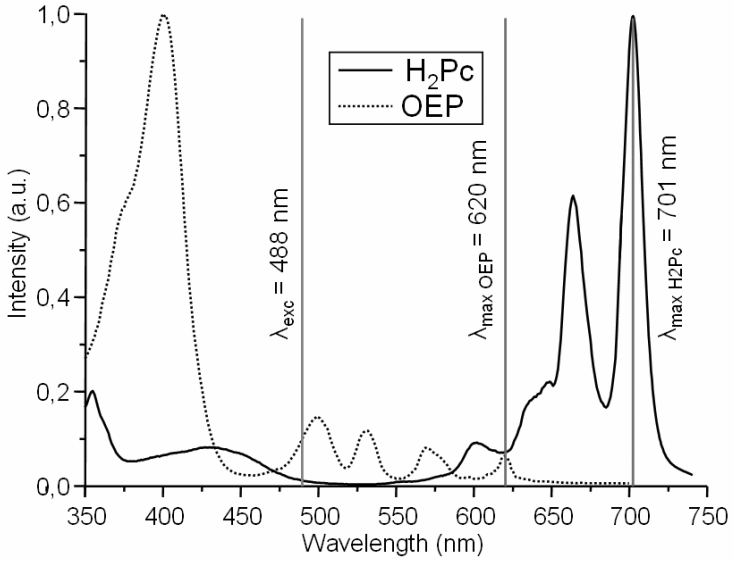

Figure 21. Excitation spectra of H_2Pc and OEP molecules (**1** and **2**, respectively). The plot shows the excitation wavelength (green line) and maxima of the most red-shifted spectral bands (red lines).

Compared to the excitation energy (245 kJ/mol), this value determines the possibility for the excited-state tautomerism to occur. Thus, for molecule **1** we obtained 228 kJ/mol, which allows the molecule to undergo the excited state tautomerization upon excitation with 488 nm laser light, while molecule **2** showed the value 250 kJ/mol. The latter exceeds the excitation power, however, the energy difference of the order of 5 kJ/mol can be compensated by the environment-induced effects, such as local heating or fluctuation of the charges distribution, which leads to the rare sudden switching of the molecule **2** from one trans tautomeric form to another.

To obtain more detailed information on this interesting issue, dedicated studies, including spectroscopic measurements as well as imaging of the tautomerism process for the same single molecules will be carried out in the near future.

4 Imaging of the Single CdSe/ZnS Quantum Dots

In this chapter we present new results on single CdSe/ZnS quantum dots (QDs). Using azimuthally and radially polarized laser beams for the excitation of the QDs, we show that nanoparticles possess the 3D excitation TDM in contrast to the most of common organic dye molecules with 1D excitation TDM. We show that the experimentally obtained fluorescence patterns are in good agreement with the simulated patterns.

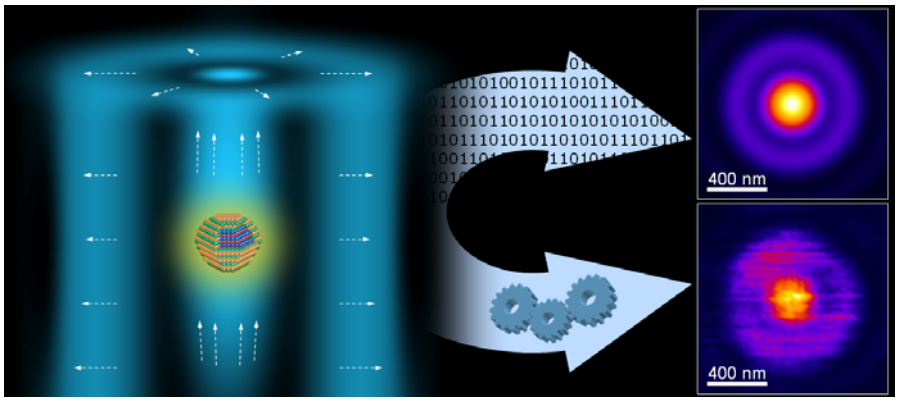

This chapter is based on:

A. I. Chizhik, A. M. Chizhik, D. Khoptyar, S. Bär, A. J. Meixner, *Nano Lett.*, **11(3)**, 1131–1135, **2011**. link to article page

4.1 Introduction

Nanometer-sized semiconductor quantum dots (QDs) have received much attention over the past decades as a result of their size-dependent optical properties [63-65]. Due to the confinement of electrons and holes in the nanocrystallites the energy level scheme resembles that of an atom, with many discrete energy levels. The separation between energy levels increases as the particle size decreases. A series of unique photophysical properties of QDs, such as blinking (fluorescence intermittency) [66, 67], bleaching, spectral jumping [68], etc., have been observed and interpreted.

It is well known that in contrast to common organic chromophores with a simple 1D emission TDM, spherical direct-gap semiconductor CdSe/ZnS QDs show the 2D emission TDM. Bawendi et al. [3] have shown using the method of polarization microscopy (rotating the linear polarizer in front of the detector) that depending on the orientation of so called “bright plane”, the emission light of the single quantum dots can be polarized or depolarized. The “bright plane” can be described as a plane in which two orthogonal dipole moments are lying. The “bright plane” is orthogonal to the “dark axis” which is oriented along the c-axis of the nanocrystal. When the orientation of the “bright plane” is known, the 3D orientation of the single CdSe/ZnS nanocrystal can be determined as well.

Schuster et al. [69] have shown that using defocused wide field fluorescence imaging the information about the orientation of the single QD and its emission TDM can be obtained. By using this method authors showed that QDs have an elliptical 2D emission transition dipole moment.

Remarkably, little attention has been paid to the dimensionality of excitation TDM of CdSe QDs, while this parameter strongly influences the excitation efficiency of the quantum dot, which is important for numerous applications. Bawendi and coauthors [3] have found the weak excitation polarization of the single spherical CdSe/ZnS QDs. This observation was explained by the fact that a region with a relatively high density of electronic states was excited and QDs have lack of a polarization memory for the excitation. This means that many states with different transition dipole moment orientations are excited simultaneously and the dimensionality of the transition dipole moment should be higher than one. Another possible reason that spherical CdSe/ZnS

QDs possess no excitation polarization can be the fact that in spherical nanoparticles the absorption dipole is uncorrelated in direction. According to this observation we assume that the excitation fluorescence patterns of the single spherical QDs are different from the excitation patterns of the single dye molecules which possess linear excitation TDM.

In this chapter we present the imaging of the excitation TDM of the single CdSe/ZnS quantum dots using APLB and RPLB for the excitation. We show that the excitation fluorescence patterns of the QDs have different shape from the patterns of the dye molecules (chapter 2) or single SiO_2 nanoparticles (chapter 5) which possess the linear excitation TDM. According to observed excitation patterns, we can assume, that investigated CdSe/ZnS QDs possess 3D excitation TDM and QDs can be excited with any polarization of the laser beam.

4.2 Experimental

CdSe/ZnS QDs: We investigated commercially available core/shell CdSe/ZnS QDs of different sizes soluble in toluene or in water. The toluene soluble Evidots®, Fig. 22 (Evident Technologies, emission centered at 557, 580, 593 and 629 nm), Lumidots™ (Sigma Aldrich, at 610 nm) and quantum dots from PlasmaChem at 610 nm were investigated. Water soluble quantum dots (Qdot® Invitrogen, emission centered at 565 nm) were studied as well.

Sample preparation for single QDs investigation: All samples with single QDs were prepared by the method of spin coating (see chapter 2.1). For the measurements the toluene soluble QDs were embedded in PMMA matrix, while water soluble QDs were spin coated on the surface of the clean cover slide without the polymer.

Microscopy: Fluorescence imaging of the single QDs was performed with the experimental setup sketched in Fig. 1 and described in chapter 2.1. All optical measurements were performed at room temperature. The typical image size was 100 × 100 or 200 × 200 pixels. For each pixel, the signal was integrated over 5 ms, resulting in an acquisition time of 50 or 200 s, respectively. Monodirectional scanning process doubles this time to the value of 100 or 400 s for one fluorescence image, respectively.

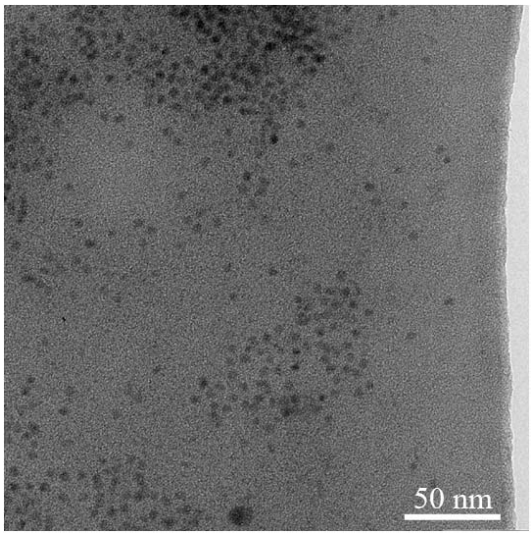

Figure 22. The TEM image of toluene soluble core/shell CdSe/ZnS Evidots® reveals the spherical shape of the nanoparticles.

4.3 Fluorescence Imaging of Single CdSe/ZnS QDs Using Higher-Order Laser Modes

The observed fluorescence patterns of the toluene and water soluble CdSe/ZnS QDs excited with radially (Fig. 23a) and azimuthally (Fig. 23b) polarized laser beam are identical to the patterns which were obtained for the Nile Red fluorescent beads (see chapter 2.4). The single fluorescence bead consists of approximately 200 molecules which are encapsulated in the polymer sphere of 20 nm in diameter. Such fluorescence beads can be considered as an isotropic emitter. The beads have the 3D excitation TDM since the molecules inside the polymer sphere have random orientations [7]. Thus, all polarizations of the excitation light are absorbed simultaneously by the molecules (in contrast to the interaction of these modes with a single transition dipole of one distinct emitter (see chapter 2.2)). The obtained scan images of the single QDs as well as of Nile red fluorescence beads are a measure for the electric field distribution in the focus of the excitation beam. The patterns of the QDs excited with the RPLB have a shape like a bright spot with weak ring around (Fig. 23a), this is a result from the interaction with strong longitudinal and weak in-plane components of the focused beam. The patterns of

the QDs excited with APLB have a shape like a ring (Fig. 23b), since the focused laser beam has only in-plane component.

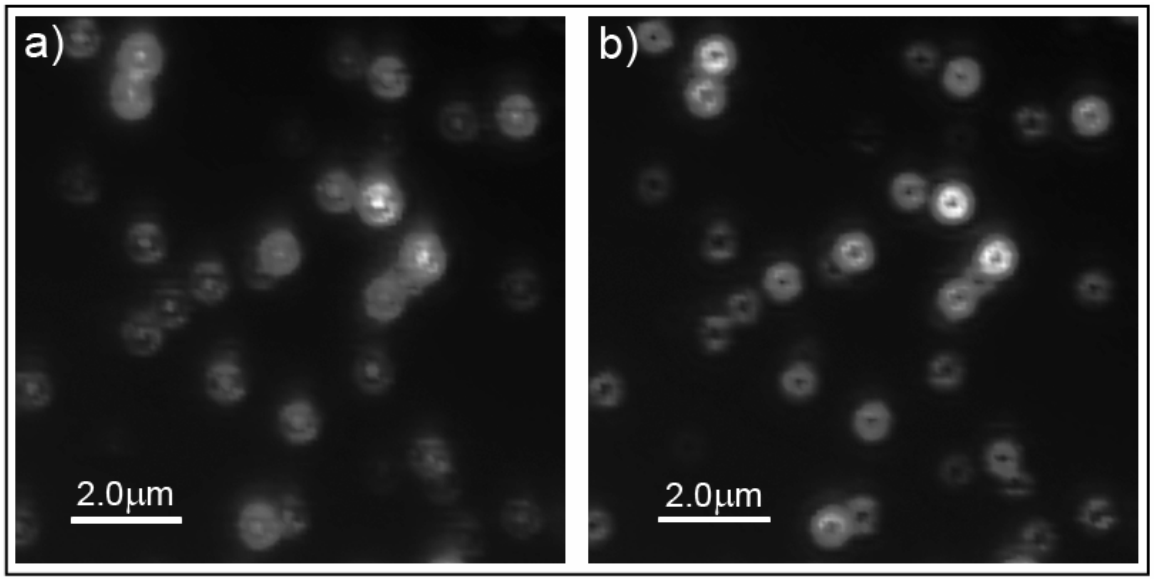

Figure 23. Fluorescence excitation patterns of the same water soluble CdSe/ZnS QDs excited with radially (a) and azimuthally (b) polarized laser beam.

We compared the experimental and simulated patterns of the QDs excited with APLB and RPLB. We chose for the simulation of the fluorescence patterns of the single QD the theoretical model, which consists of three orthogonal dipoles, the first is codirectional to *x* axis, the second – to *y* axis and the third – to *z* axis. This model describes the 3D excitation TDM. Figure 24a and 24b shows the cross-sections through the center of experimental (red circles) and simulated (blue line) excitation fluorescence patterns of QD excited with APLB and RPLB, respectively. Comparison of the cross-sections through the centers of the experimental and simulated patterns shows excellent agreement between the measured data and theoretical fit. This suggests that the studied single CdSe/ZnS quantum dots have a spherically degenerate excitation TDM.

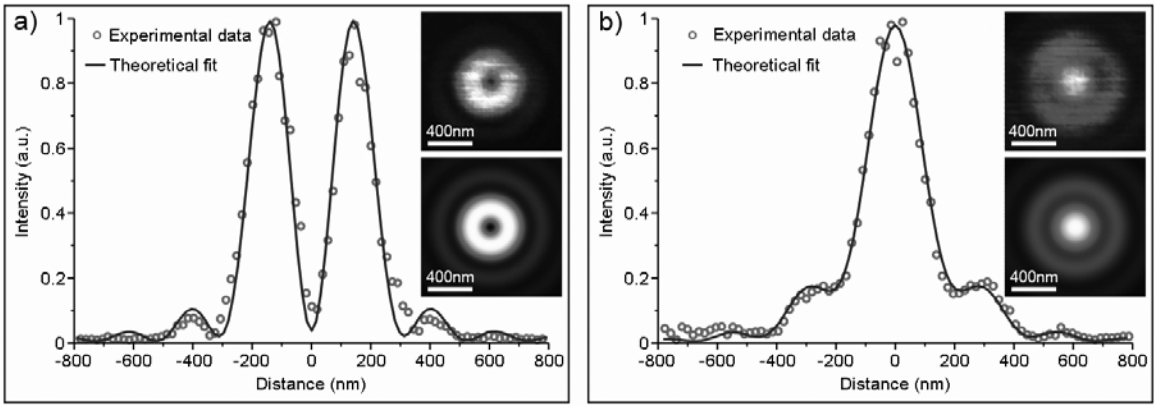

Figure 24. (a), (b) The cross-sections through the center of the experimental (red circles) and simulated (blue line) fluorescence pattern of the single QD excited with azimuthally and radially polarized laser beam. The insets show experimental (upper images) and corresponding simulated (lower images) fluorescence patterns of the QD.

This result is in good agreement with observation of the weak excitation polarization dependence of the single CdSe/ZnS nanocrystals [3], since in both studies the nanocrystals were excited in a region with a relatively high density of electronic states. While individual states should have distinct transition dipole orientations, simultaneous excitation of multiple overlapping states decreases the degree of polarization in excitation. In this case, the weak dependence between the polarization of the excitation light and the photoluminescence (PL) intensity can also be attributed to fluctuations of the single particle PL. The single nanocrystal excitation patterns, presented in Figures 23, 24 have been acquired with excitation density near 100 W/cm^2, which slightly exceeds the density used in the study carried out by Empedocles et al. (60 W/cm^2) [3]. However, variation of the excitation density from 50 to 1000 W/cm^2 did not lead to the change of the excitation pattern shape, which suggests that the dimensionality of the single CdSe/ZnS nanocrystal is not sensitive to the change of the excitation density within this range.

4.4 Blinking and Bleaching Behavior of the Single CdSe/ZnS QDs

The most commonly used model that describes blinking in semiconductor QDs was developed by Frantsuzov *et al.* [70], which is called photoionization model. They attributed the photoluminescence blinking to a random switching between emitting "on" and nonemitting "off" states due to the ionization of QDs under light excitation. The black strips of the fluorescence images (Fig. 25) correspond to the "off" states of the QDs, since no light is emitted during that time.

The water soluble QDs show more stable patterns in comparison with toluene soluble QDs. The water soluble QDs have additional polymer coating, which probably protects the QD from the oxidation and ionization. The toluene soluble QDs have no such coating and show a long time in the non-emitting "off" state during the scanning process.

The disappearance of the emission (bleaching) is caused by the formation of lattice defects (quenching states) in the QDs, thereby creating additional nonradiative recombination pathways [71]. For the QDs in air the quenching states are expected to be formed at the CdSe/$CdSeO_x$ interface. The formation of surface quenching states causes a decrease of the number of photons emitted. Finally, the luminescence disappears and the QD has bleached.

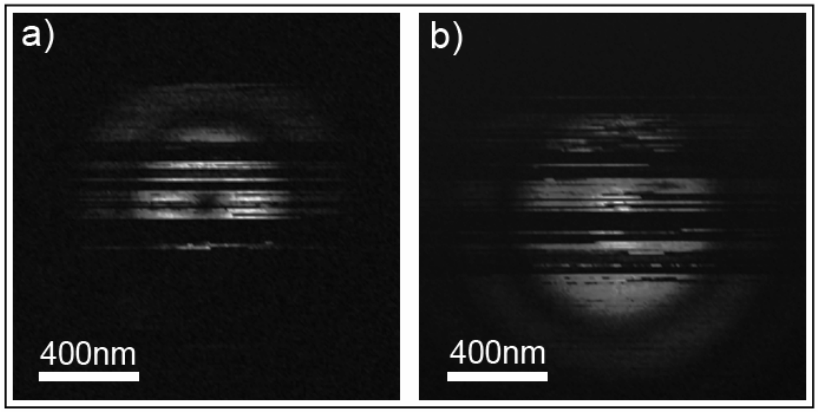

Figure 25. Fluorescence excitation patterns of the same toluene soluble single CdSe/ZnS QD excited with an azimuthally (a) and radially (b) polarized laser beam.

4.5 Summary and Conclusion

In summary, using CVB we studied dimensionality of the excitation TDM of individual CdSe/ZnS nanocrystals. By comparing experimental and simulated excitation patterns, we concluded that the quantum dots possess a spherically degenerate excitation TDM. Observation of a large number of single nanocrystals with different core sizes, both deposited on the top of glass cover slide and embedded in a polymer matrix, revealed that dimensionality of CdSe/ZnS quantum dots is neither affected by the local host environment, nor depend on the size of the core or the type of the coating of the nanocrystal.

Now we want to summarize the first part of our work. We have shown that the excitation pattern of an individual quantum emitter obtained by scanning it through the focal region of an APLB or RPLB with donut-shaped intensity profile has a peculiar shape, which is strongly characteristic for the dimensionality and/or orientation of the emitter's excitation TDM. By comparing the experimental pattern with the simulated images one can determine the dimensionality and/or three-dimensional orientation of the excitation TDM of the emitter. In chapter 2.2 and 2.5 we have shown the simulated and experimental fluorescence patterns for the dye molecules which possess the 1D excitation TDM. In chapter 3.5 we presented the simulated and experimental patterns for the metal-free phthalocyanine molecules which possess 2D excitation TDM, since during the fast tautomerism process the TDM of the molecule can be considered as the plane with two orthogonal dipoles (2D excitation TDM), the dipoles correspond to two different trans forms of the molecule. In this chapter we have shown the simulated and experimental excitation fluorescence patterns of the CdSe/ZnS QDs which possess the 3D excitation TDM.

5 Imaging of Defect Luminescence in Single SiO_2 Nanoparticles

In this chapter we present new results on single SiO_2 nanoparticles (SiO_2 NPs). Using an azimuthally and radially polarized laser beam for the excitation, we determine the three-dimensional orientation of the nanoparticles' transition dipole moment (TDM). The SiO_2 NPs were found to possess quite stable and randomly oriented TDMs. However, characteristic dynamical effects featuring single NPs such as fluorescence intermittency and TDM flipping could also be observed.

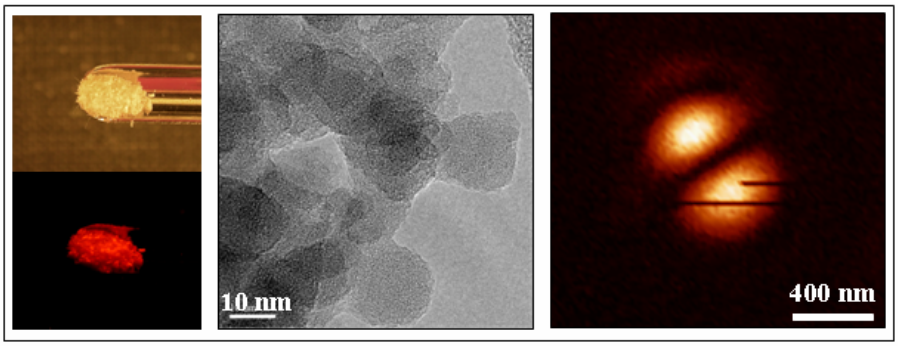

This chapter is based on:

A. M. Chizhik, A. I. Chizhik, R. Gutbrod, A. J. Meixner, T. Schmidt, J. Sommerfeld, F. Huisken, "Imaging and Spectroscopy of Defect Luminescence and Electron-Phonon Coupling in Single SiO_2 Nanoparticles", *Nano Letters*, **9(9)**, 3239-3244, **2009**. link to article page

and

A. M. Chizhik, T. Schmidt, A. I. Chizhik, F. Huisken, A. J. Meixner, "Confocal Microscopy and Spectroscopy of Defect Photoluminescence in Single SiO_2 Nanoparticles", *Proc. SPIE*, **7393,** 739305, **2009**, doi:10.1117/12.825288. link to article page

and

A. M. Chizhik, A. I. Chizhik, A. J. Meixner, T. Schmidt, F. Huisken, "Fluorescence Imaging and Spectroscopy of Single Si and SiO_2 Nanoparticles Using Confocal Microscopy", *Bonsai Project Symposium: Breakthroughs in Nanoparticles for Bio-imaging, AIP Conf. Proc.*, **1275**, 63-70, **2010**. link to article page

Silica nanoparticles were prepared by T. Schmidt (Jena University).

5.1 Introduction

Since more than two decades there is an ongoing discussion on whether the photoluminescence (PL) from nanostructured silicon originates from intergap transitions in quantum confined systems [72, 73] or whether it is due to surface defect states [74-76]. Very recently it was shown [77, 78] that it is possible to control the origin of the PL of silicon nanocrystals (Si NCs) and to switch between quantum confinement and defect-based PL by hydrogen passivation and UV irradiation, respectively. Investigation of naturally oxidized Si NCs selected in size (2.5 to 8 nm) revealed that the PL is caused by quantum confinement, with slight deviation occurring for small NCs (2 to 3 nm in diameter) [79]. This observation was confirmed by Wolkin et al. [80] comparing the PL of Si NCs passivated with hydrogen and oxygen with theoretical results. He concluded that defect PL via oxygen-related inner-gap states becomes dominant when quantum confinement causes the band gap to exceed certain energy. Furthermore, Martin et al. [81] showed that the emission from Si NCs is ruled by quantum confinement for large particles, while small Si NCs revealed that defect-based luminescence is dominating. The defect PL in oxygen-passivated Si NCs originates from localized states in the SiO_2 shell surrounding the crystalline silicon core. Removing the entire Si core, for example by full oxidation, the same states should also be operative. Therefore, the question arises whether the same defect luminescence can also be observed in SiO_2 NPs which are prepared by intentional oxidation of Si NCs. Strong visible luminescence observed from hollow SiO_2 NPs which had been obtained by full oxidation of Si NCs in water was reported by Colder et al. [82]. Surprisingly, the PL spectra of such SiO_2 nanopowder show a very similar shape to that ones recorded from small Si NCs. This gives reason to assume that the origin of the PL can be referred to the same operating mechanism, obviously related to defect PL. Thus, in spite of the extensive results on Si NCs, the origin of the emission is still under debate. Apparently, the border between quantum confinement and defect PL is diffuse, especially for small Si NCs.

In the present study, experiments on single SiO_2 NPs obtained by full oxidation of Si NCs were carried out. Confocal microscopy in combination with higher-order laser modes revealed that the SiO_2 NPs posses a linear, randomly oriented transition dipole

moment (TDM) for excitation and exhibit dynamical effects such as TDM flipping and fluorescence intermittency.

5.2 Experimental

Synthesis of SiO_2 NPs: Amorphous SiO_2 NPs were prepared according to the recipe of Colder et al. [82]. Si NCs (~10 mg), freshly prepared by laser-induced pyrolysis (described in chapter 6.2) [83, 84], collected on a filter paper in the exhaust line of the flow reactor were dispersed in 1 ml doubly distilled water applying ultrasonic treatment for 10 min. The beige viscous solution was stored at room temperature for several days without any further treatment until the yellowish color had turned to a transparent appearance, a clear indication for complete oxidation of the crystalline Si NPs to amorphous SiO_2 NPs. Finally, to evaporate the water, the vessel containing the nanoparticles solution was heated in a simple non-evacuated oven at 95°C. The residue at the bottom of the vial is a white powder exhibiting strong red-orange PL under the illumination of a laboratory UV lamp (λ = 254 nm). High-resolution transmission electron microscopy (HRTEM) images, shown in Fig. 26, reveal the complete amorphous structure of the as-synthesized silica nanopowder. In the present study, the SiO_2 NPs have an average size of 21 nm.

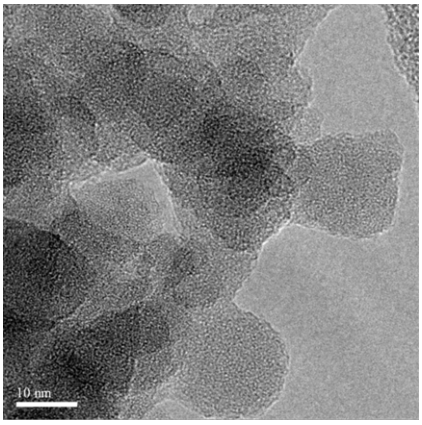

Figure 26. The HRTEM image of silica nanoparticles reveals the complete amorphous structure of the nanoparticles.

Sample preparation for single nanoparticles investigation: For investigation of single SiO_2 NPs in glass-polymer-air confinement, the particles were embedded in very

low concentration into a thin polymer film. For preparing samples containing SiO_2 NPs a small amount of the processed silica nanopowder was dispersed in toluene and then mixed with the polymer (PMMA or PS). Then the droplet (10 µl) of the mixture was spin-coated onto a clean cover slide surface (thickness 170 µm). The thickness of the polymer film of about 50-60 nm was determined by AFM measurements. The two polymers (PMMA and PS) were used to clarify the influence of a polar (PMMA) and a non-polar (PS) matrix on the properties of SiO_2 NPs.

Microscopy: Fluorescence imaging of the single silica nanoparticles was performed with the experimental setup sketched in Fig. 1 and described in chapter 2.1. For the polarization microscopy experiments the emission from the single silica nanoparticles was observed through a linear polarizer and its intensity was recorded as a function of the rotation angle of the polarizer.

5.3 3D Transition Dipole Moment Orientation of the Single SiO_2 Nanoparticles

Figure 27a shows an experimental fluorescence image of two single SiO_2 NPs excited with RPLB possessing a one-dimensional TDM. Particle (1) reveals nearly vertical orientation of the TDM (see calculated pattern in Figure 27c). Particle (2) demonstrates a double-lobe pattern and significantly lower intensity than in the previous case. This is caused by higher intensity of the longitudinal component of the excitation field (chapter 2.3). The shape of particle (2) reveals nearly horizontal orientation of the NP TDM ($\varphi \approx 100°$; $\theta \approx 90°$ see Figure 27d).

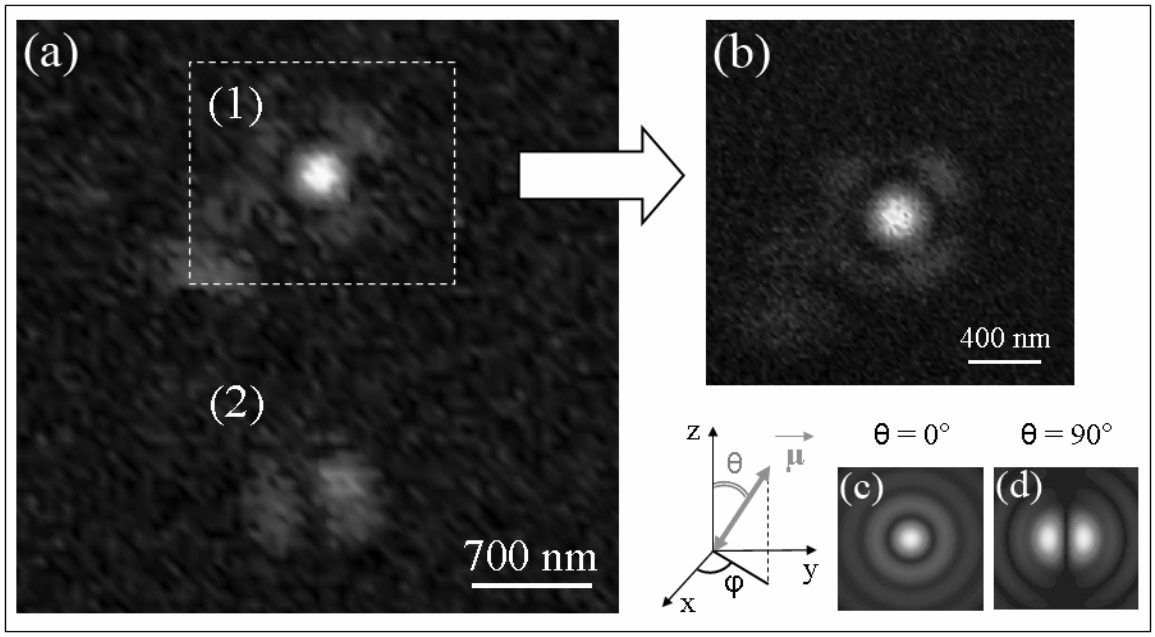

Figure 27. (a) Fluorescence image of two single SiO_2 NPs (PMMA matrix) excited with a radially polarized laser beam revealing different three-dimensional orientation of TDM. (b) High resolution fluorescence image of particle (1) allowing precise determination of the three-dimensional orientation of the TDM. (c) and (d) The simulated emission patterns of two different orientations of TDM ($\theta = 0°$ and $\theta = 90°$) after the excitation with radially polarized laser beam (the images are calculated considering $\varphi = 90°$).

Extensive statistical measurements (more than 200 images) indicate presence of a one-dimensional TDM. Moreover, we found that there is no preferred direction with respect to the substrate surface suggesting that the TDMs are randomly oriented. This is not surprising if one keeps in mind that the NPs are embedded in a ~50 nm thick polymer matrix which keeps them far away from the substrate.

5.4 Emission Polarization of the Single SiO_2 Nanoparticles

Due to the presence of a one-dimensional TDM for excitation, the particle is expected to emit light possessing linear polarization. To confirm this assumption, the fluorescence of a single SiO_2 NP was investigated using a polarization analyzer in front of the photodetector (APD). For each consecutive scan of the sample area, the analyzer

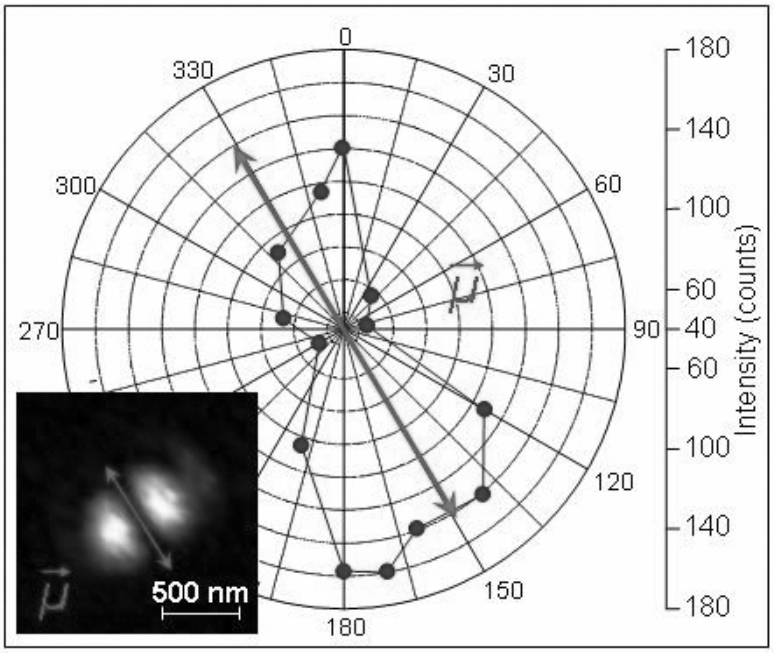

Figure 28. In the left corner, the fluorescence image of a SiO_2 NP in PMMA is shown. As the laser beam was azimuthally polarized, the transition dipole moment for excitation is oriented along the dark gap of the PL pattern. The emission of the same SiO_2 NP was observed through a linear polarizer and its intensity was recorded as a function of the rotation angle of the polarizer. The result presented in polar coordinates shows that the emission dipole moment has the same direction as the one for excitation.

was rotated by a distinct angle. The results of this experiment are presented in Fig. 28. It shows in the inset an image of a single NP measured with an APLB. The TDM is indicated by the red arrow. The integrated fluorescence intensity of this NP was recorded as a function of the polarization analyzer orientation and plotted into a polar coordinate system. The fact that we measure two lobes demonstrates that the emission of a single SiO_2 NP is linearly polarized, and its orientation proves that the TDM for emission has the same direction as the one for excitation. This observation suggests that the PL photon arises from the same defect which was excited. Thus, we have the important result that charges carrier hopping between different defect states is not very likely to occur. The SiO_2 NP seems to behave like a molecule with stable linear TDM.

5.5 Blinking and Bleaching Behavior of Single SiO_2 Nanoparticles

Figure 29a-d shows a series of images of a single SiO_2 NP in PMMA matrix excited with APLB, acquired one after another. The images demonstrate one-dimensional TDM, which remains constant during the whole acquisition time of four images (~ 400 s). In the case of APLB the TDM orientation of the emitter is codirectional with the dark gap, separating the lobes of the coffee bean (Figure 29a). Figures 29b and 29c reveal blinking process which can be explained by electron trapping and non-radiative charge carrier recombination. This process clearly proves that we deal with a single quantum emitter. After sudden bleaching depicted in Figure 29d the particle didn't show PL anymore.

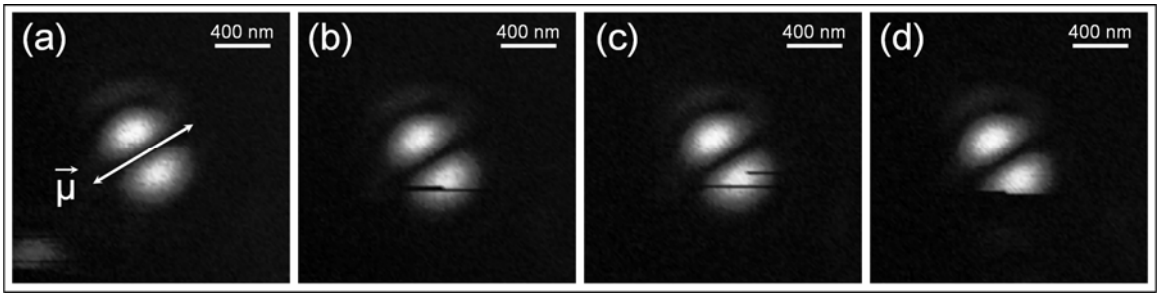

Figure 29. (a)-(d) A series of consecutive fluorescence images of a single SiO_2 NP (PMMA matrix) excited with an azimuthally polarized laser beam. The arrow in image (a) indicates the orientation of the SiO_2 NP TDM. Image (b) and (c) shows blinking of the particle, while the scan in image (d) reveals bleaching.

5.6 Flipping of the Transition Dipole Moment Orientation in Single SiO_2 Nanoparticles

After having presented results on SiO_2 NPs embedded in a thin PMMA polymer layer, we turn to PS as matrix material. At first, we would like to state that, in PS, dynamical effects seem more likely to occur than in PMMA. An example is given in Figure 30a-d which shows a series of images taken one after the other, all showing the same section of 4.3×4.3 μm containing essentially one SiO_2 NP exhibiting relatively strong photoluminescence and 4 NPs of lower intensity. The sample was excited with an APLB, and the time between two consecutive samplings of the same area was 100 s. Following the images from 30a to 30d, we observe a bright two lobe pattern in the center

of each image. Image 30b shows fluorescence intermittency (blinking) of the NP manifested by the sudden quenching of the PL being active for at least 12 s. In image 30c, the same NP appears bright again. Another interesting dynamical effect is demonstrated by the fainter double lobe pattern marked by the dashed circle. Comparing image 30a and 30d, we observe a flipping of the orientation of the TDM, while images 30b and 30c demonstrate intermediate states without a definite stable TDM orientation. Moreover, image 30c also reveals sudden blinking of the NP.

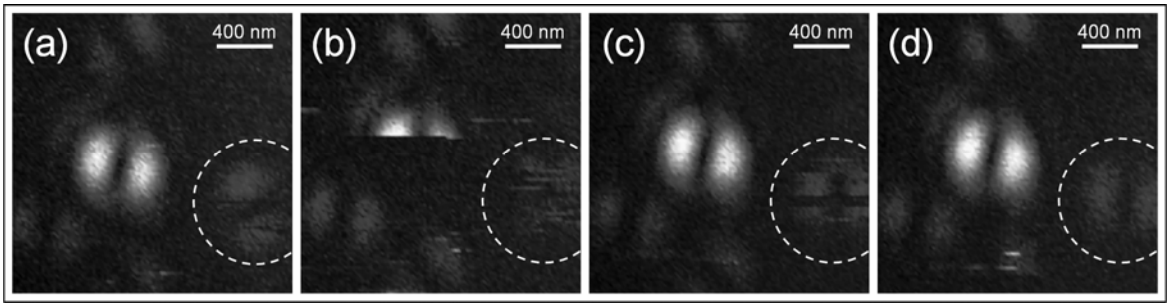

Figure 30. Images of SiO_2 NPs embedded in a polystyrene matrix and excited with an azimuthally polarized laser beam. The images (a) to (d) show the same image section of a series of pictures recorded one after the other every 100 s. The following dynamical processes are observed: Image (b) reveals fluorescence intermittency of the brighter NP (blinking). Blinking is also observed for the fainter NP (marked by the dashed circle) in image (c). In addition, sudden flipping of the TDM of the fainter NP is observed as can be seen by comparing images (a) and (d), while images (b) and (c) show intermediate unstable conditions of the TDM.

However, it should be mentioned that such dynamic effects as fluorescence intermittency and flipping of the TDM were observed quite rarely. These phenomena can be explained by a redistribution of defect states caused by charge fluctuations in the surrounding of the NP. TDM flipping results from the fact that another defect has become energetically more favorable to be accessed. As usual, fluorescence intermittency can be explained by electron trapping and non-radiative charge carrier recombination at the hole. As already mentioned, we have found that dynamical effects are more likely to occur when the SiO_2 NPs are embedded in the nonpolar PS matrix. In contrast to this, defects involved in the excitation and emission process seem locally and energetically more stable if the NPs are surrounded by the polar PMMA matrix. This is ascribed to the

oxygen atoms surrounding the NPs and giving rise to a stronger fixation or localization of the defects. The stabilized situation is also reflected by the better contrast of the fluorescence images.

5.7 Summary and Conclusion

In conclusion, the study of the single SiO_2 NPs microscopy has significantly improved our understanding of defect PL. Imaging of single NPs using a novel laser beam polarization conversion technique revealed new details of origin and dynamics of the SiO_2 NPs TDM. In particular, the fluorescence images clearly revealed presence of linear TDM, which was stable for most of the NPs. However, such dynamic effects as fluorescence intermittency and flipping of the TDM were rarely observed.

6 Luminescence Imaging of Individual Si Nanocrystals. Part I: Defect Photoluminescence.

In this chapter we show that with the help of laser polarization technique, we are able to visualize the transition dipole moment (TDM) for the excitation of individual Si nanoparticles. The dimensionality of the TDM yields information on the process being responsible for the detected PL.

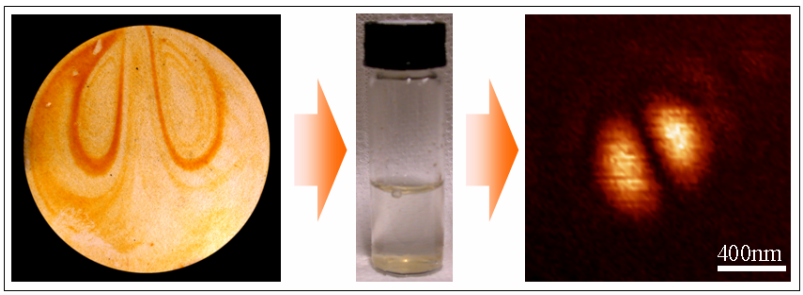

This chapter is based on:

T. Schmidt, A. I. Chizhik, A. M. Chizhik, A. J. Meixner, F. Huisken, "Luminescence Characteristics of Individual Si Nanocrystals Studied by Confocal Microscopy", submitted.

and

A. M. Chizhik, A. I. Chizhik, A. J. Meixner, T. Schmidt, F. Huisken, "Fluorescence Imaging and Spectroscopy of Single Si and SiO_2 Nanoparticles Using Confocal Microscopy", *Bonsai Project Symposium: Breakthroughs in Nanoparticles for Bio-imaging, AIP Conf. Proc.*, **1275**, 63-70, **2010**. link to article page

Si nanocrystals were prepared by T. Schmidt (Jena University).

6.1 Introduction

Silicon, the element of today's processor technology, still offers a wide and active field of research despite the amazing progress that has already been achieved. Dominating the microelectronics with its exceptional electronic properties, silicon is known to be a poor light emitter due to its indirect band gap structure. Nowadays, due to the dramatically growing information volume, an efficient optoelectronic communication just based on silicon is highly desirable. Therefore, an adequate understanding of the optical properties of nanostructured silicon is essential for designing new devices in photonics and optoelectronics.

Intense visible photoluminescence (PL) from nanostructured porous silicon was observed for the first time in 1990 [72, 73]. Since this time, the research was focused on the optical properties of nanostructured silicon. In particular, silicon nanocrystals (Si NCs), as possible light-emitting sources, generated a still ongoing debate about the origin of their PL. However, reviewing the extensive literature of the past two decades [80, 81, 85-87], a general agreement on the involved luminescence processes seems to develop. On the one hand, there is the radiative recombination of excitons driven by quantum confinement (QC) and, on the other hand, the PL may arise from defect centers (DCs) in the oxide shell surrounding the silicon core or in the interface between core and shell. Unfortunately, the emitted light, arising from both, QC and DCs, covers the same spectral range, making a definitive assignment of the PL very difficult. A recent study by Godefroo et al. [77, 78] on Si NCs demonstrated that it is possible to control the PL originating from quantum-confined charge carriers and from defect states, respectively, by hydrogen passivation and UV irradiation.

The number of publications dealing with single quantum dots is still quite small, but since a couple of years, the technique and equipment for high-quality analysis of single quantum dots made a big step forward. Especially confocal microscopy is a powerful tool giving insight into fundamental optical properties. Recently obtained results on single SiO_2 nanoparticles (NPs) [10] visualized the orientation of the TDM by applying scanning confocal fluorescence microscopy in combination with CVB (see chapter 5) [4, 17].

The present study is focused on the PL characteristics of individual Si NCs with lateral dimensions between 2 and 8 nm, synthesized by laser-induced pyrolysis of SiH_4 [83, 84]. It is a continuation of a previous work on single SiO_2 NPs [10, 11] (chapter 5) employing the same methods. Moreover, it can be considered as an extension of the earlier work of Martin et al. [81] on Si NCs, delivering additional and new information on the transition dipole moment for excitation and emission of single NPs. As the Si NCs and SiO_2 NPs were investigated with the same equipment and under the same conditions, it is possible to compare the optical properties of both systems on a single particle level.

Comparing Si NCs with SiO_2 NPs, one should always be aware of the fundamental difference between these two nanomaterials. Whereas Si NCs are composed of a crystalline Si core surrounded by an amorphous layer of SiO_2, the SiO_2 NPs are completely oxidized and amorphous. Therefore, we distinguish semantically between nanocrystals (Si NCs) and nanoparticles (SiO_2 NPs). While the PL of SiO_2 NPs results from defects, the PL of Si NCs can have the two different origins discussed (QC and DCs). Note that, the smaller the Si NCs are, the more important the SiO_2 shell is. As a result, one should expect that the contribution of defect PL becomes increasingly more important with decreasing size of the Si NCs.

6.2 Experimental

Synthesis of Si NPs: The technique for synthesis of ultra fine silicon powder is based on laser-induced pyrolysis of the gaseous precursor silane (SiH_4). The dissociation of SiH_4 followed by gas phase condensation and subsequent formation of crystalline silicon quantum dots (Si NCs) takes place in a laser-driven gas flow reactor. For decomposition of the precursor molecules a pulsed CO_2 laser is used providing very sharp temperature gradients in the gas phase combined with reactions proceeding in a wall-less environment.

A schematic view of the flow reactor employed for synthesis of Si NCs is shown in Figure 31. The reactor is built from a standard stainless steel NW40 cross vacuum fitting. The reaction gas enters the centre of the flow reactor through a stainless-steel tube of 3 mm diameter. Coaxially arranged, in order to confine the precursor gas flow to the

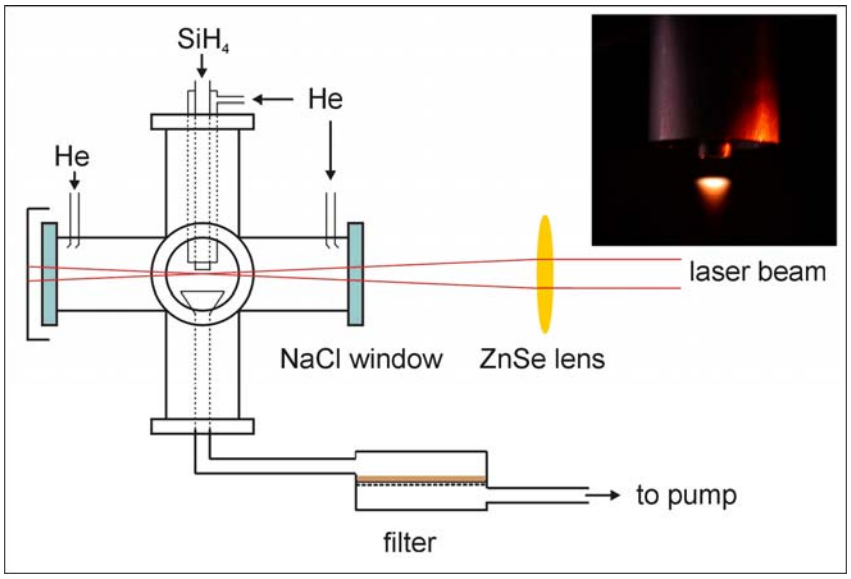

Figure 31. Schematic view of the gas flow reactor. The reactant gas SiH_4 enters through the inner tube, the confinement gas He through the outer tube. The flow of the gases is regulated by controlling independently flow velocity and concentration by means of a flow meter system. The radiation of a pulsed CO_2 laser enters and leaves the reactor through NaCl windows and is focused tightly below the inner tube perpendicular to the gas flow axis to induce the decomposition of SiH_4.
Inset: Photography of the reaction zone. The inner tube and the outer tube for admitting the reactant gas and the confinement gas, respectively. The decomposition of silane (SiH_4) induced by the CO_2 laser radiation results in a visible luminescence, appearing just 2 – 3 mm below the inner tube of the flow reactor.

flow axis, helium is flushed as buffer gas through the outer tube of 12 mm diameter. The gas and reaction products are pumped by a backing pump (D16B, Typ Leybold) through a funnel-shaped tube facing the inlet tubes. The produced nanopowder is collected in a filter unit (Figure 32) at the exit of the flow reactor.

Gas flow rates and the total pressure inside the reaction chamber and therefore concentrations and flow velocities of the precursor gas and the inert confinement gas are regulated independently by means of an appropriate flow meter system (flow regulation system Typ 647BE, MKS instruments; needle valve 248AC, MKS instruments; pressure gauge, 122A, MKS instruments).

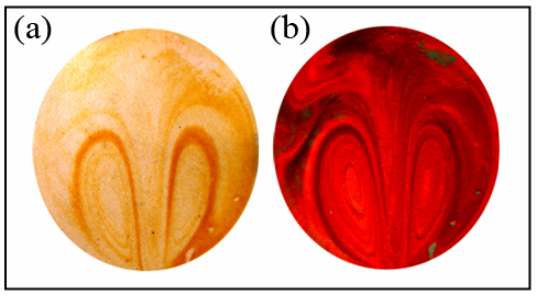

Figure 32. Silicon nanopowder collected on a paper filter observed with (a) daylight and (b) UV light (254 nm).

The molecular flow emanating from the inner gas inlet is crossed perpendicularly by the focused radiation (ZnSe lens with 190.5 mm focus length) of a line-tunable CO_2 laser which enters and leaves the reactor through NaCl windows (loss by reflection ≈ 8 %). The viewing ports are continuously flushed with rare gas to prevent nanoparticles from coating the NaCl windows. The infrared laser intensity is regulated by passing the laser beam through a propylene gas cell with adjustable pressure (not shown in Figure X). As pyrolysing laser a pulsed URENCO-TEA CO_2 laser (model ML 104, Uranit) was used. The working conditions for the laser are: repetition rate, 20 Hz; pulse width, 150 ns; laser emission wavelength, 10.6 μm.

During the course of the experiments, various reactor conditions have been tested. However, the following conditions have been found to be particularly favourable: SiH_4 flow rate, 15 sccm; He flow rate, 1100 sccm; pulse energy of the CO_2 laser, 45 mJ (sccm denotes standard cubic centimeter per minute). The total pressure inside the reaction chamber was kept constant at 330 mbar. The induced decomposition of the gaseous precursor SiH_4 results in visible luminescence, appearing just 2 – 3 mm below the inner tube (see inset in Figure 31).

Sample preparation for single nanocrystals investigation: All samples with single Si NCs were prepared by the method of spincoating as in the case of silica nanoparticles (see chapter 2.1).

Microscopy: Fluorescence imaging of the single Si NCs was performed with the experimental setup sketched in Fig. 1 and described in chapter 2.1. For the polarization microscopy experiments the emission from the single silicon nanoparticles was observed

through a linear polarizer and its intensity was recorded as a function of the rotation angle of the polarizer.

6.3 Fluorescence Imaging of Single Si NCs Using Higher-Order Laser Modes

For the purpose of clarifying the origin of the PL of single Si NCs (QC vs. DCs) and to reveal possible similarities with results recently obtained results for single SiO_2 NPs (chapter 5) [10], confocal microscopy was carried out under the same experimental conditions as used for the investigation of single SiO_2 NPs.

Starting with confocal fluorescence imaging, the characteristics of the TDM for the excitation of single Si NCs were recorded. Figure 33 shows fluorescence images of two individual Si NCs embedded in a PMMA matrix excited with CVB. Images 33a and 33b display the same particles excited with APLB and RPLB, respectively. The observed patterns clearly demonstrate that single nanoparticles were detected possessing a stable one-dimensional TDM. Simulated patterns matching the experimental data (displayed in the lower panel of Figure 33) allow a precise determination of the three-dimensional orientation of the TDM for excitation relative to the substrate surface according to the coordinate system also depicted in Figure 33. Analyzing the experimental images (Figure 33a and 33b), one can derive for the left particle P1 an in-plane orientation of the TDM parallel to the substrate ($\theta = 90°$). The pattern obtained by excitation with RPLB has the shape of two lobe pattern, as in the case when APLB is used, but rotated by 90° (due to the transition from azimuthal to radial mode).

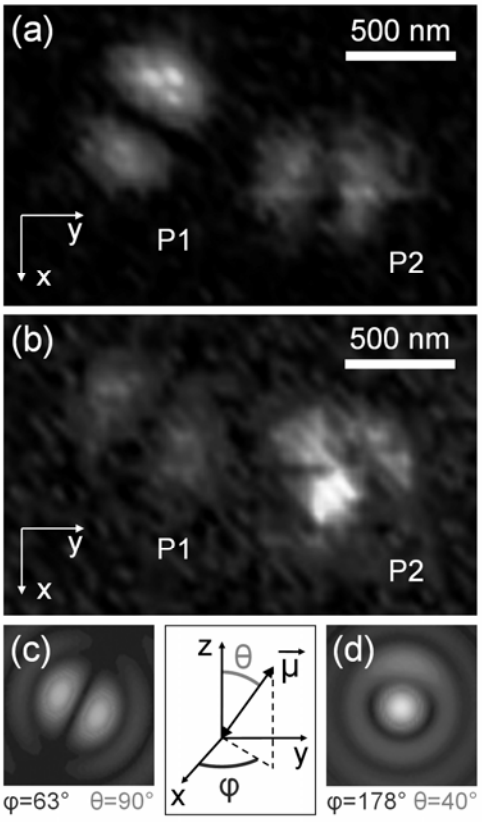

Figure 33. Fluorescence images of two Si NCs embedded in a thin PMMA layer and excited with azimuthally (a) and radially (b) polarized laser beam (λ_{exc} = 488 nm). Images (c) and (d) represent simulated fluorescence patterns giving the best fit to RPLB data shown in panel (b). Angle values for the TDM orientations are given below the calculated patterns according to coordinate system also shown. The *xy*-plane is parallel to the substrate surface.

For the right NP P2, exhibiting for RPLB excitation an emission pattern similar to a spot with a weak lobe above the spot, the TDM is oriented such that it includes an angle of θ = 40° with the *z*-axis. Images obtained from more than 300 single Si NCs clearly reveal a stable linear excitation TDM with random orientation. This observation is independent of the fact whether the NCs are embedded in PMMA or in PS.

Using the same method of polarization microscopy like in the chapter 5.4, we investigated the polarization of the emitted light from single Si NCs. We found that the

TDM for emission has the same direction as the one for excitation like in the case of single SiO_2 NPs (see chapter 5.4).

6.4 Flipping of the Transition Dipole Moment Orientation in Single Si Nanocrystals

A continuous series of fluorescence images obtained from the same Si NC by excitation with APLB is shown in Figure 34. The images were acquired one after the other, and the time needed to record one image was 100 s. The scanning direction was from left to right and from top to bottom. Starting with image 34a, the orientation of the

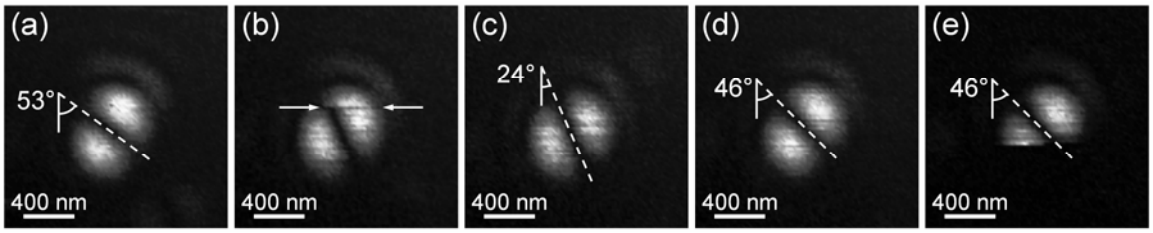

Figure 34. Series of fluorescence images, recorded one after the other, showing the occurrence of dynamical effects in a single Si NC embedded in a PMMA layer. As APLB was employed, the images reveal the projection of the TDM on the substrate. During the total time of observation of 500 s, the TDM experiences two flippings or orientational changes: one during the recording of image (b) and another between (c) and (d). The last image (e) shows fluorescence intermittency (bleaching) occurring 465 s after the start of the experiment.

projection of the TDM on the substrate surface (direction along the dark gap between the two bright spots with elliptical shape) is 53° with respect to the *x*-axis (referring to the coordinate system shown in Figure 33). Scanning the same area again, the TDM is observed to experience a sudden flipping of the TDM after approximately 145 s (referring to the beginning of the observation). This occurrence is marked by the two arrows in image 34b. The new orientation of the projection of the TDM on the surface after the flipping is 24°. 300 s after starting the experiment, another flipping has occurred, as revealed by the new orientation of the TDM ($\varphi = 46°$) in image 34d. In image 34e, a new phenomenon is observed, namely the sudden quenching (bleaching) of the PL after

65 s (in this time frame). This phenomenon is also called fluorescence intermittency, a well-known dynamical effect typical for single quantum dots. Although the image series of Figure 34 reveals two TDM flippings within 500 s, it should be noted that such orientation changes are observed quite rarely.

The observed flipping behavior of the TDM observed in Figure 34 cannot be related to a rotation of the nanoparticle itself. As the NPs are embedded (and thus locked) in a polymer matrix (PMMA in this case), sudden movements of the particle can definitely be ruled out. As has already been reported for single SiO_2 NPs (chapter 5), it is remarkable that, also for Si NCs, dynamical effects like the sudden flipping of the linear TDM were observed more often in PS than in PMMA as matrix material. An explanation for this behavior is given in chapter 5.6.

6.5 Summary and Conclusion

The present study is a follow-up of two earlier investigations on single Si NCs by Martin et al. [81] and on fully oxidized Si NCs (i.e. SiO_2 NPs, see chapter 5). In all studies, the samples were prepared from silicon nanopowders, which were produced under identical conditions in the same laboratory [84]. Moreover, all investigations utilized confocal microscopy employing very similar equipment. Compared to the SiO_2 NP study (chapter 5), the equipment is even identical. Therefore, we are in an optimum situation to compare the results of the present study with the earlier findings. This comparison allows us to draw important conclusions about the origin of the PL in small Si NCs as they are present in this study. The question to what extent these conclusions can be generalized and applied to other Si NC systems will also be discussed.

The fluorescence study of single Si NCs using CVB reveals that the TDM for excitation is linear. In contrast, for exciton creation in spherical or nearly spherical semiconductor quantum dots, we would expect a three-dimensional excitation TDM (like in the case of CdSe/ZnS QDs, see chapter 4) [3, 88, 89]. As this is not the case, we can conclude that the NC is not spherical or that the PL results from another mechanism than recombination of charge carriers in a quantum-confined system (QC). As in our study on SiO_2 NPs (chapter 5), the TDM for emission is found to have the same orientation as the TDM for excitation. Although, in most cases, the TDM stays rather stable, we sometimes

observe a sudden flipping of the TDM which is also not compatible with the QC picture. However, TDM flipping can be understood if defect centers (DCs) are responsible for the PL. In that case, it would be very likely that not only one DC but several DCs exist in the shell or interface of the same particle and may contribute to the PL. TDM flipping can then be explained by charge fluctuations in the (matrix) environment of the NP affecting the energy levels of the DCs and thus favoring the activation of different DCs depending on the situation.

In comparing Si NC and SiO_2 NP results, we found many close agreements: (1) The experiments visualizing the TDM for excitation and probing the orientation of the TDM for emission deliver exactly the same results. (2) No difference is found in studying the dynamical processes like TDM flipping, fluorescence intermittency, and bleaching.

Due to these close agreements, we are led to make defect centers responsible for the PL in both nanosystems.

Unfortunately, we cannot be sure that the Si NCs originally prepared were not oxidized to become SiO_2 NPs during the preparation of the confocal microscope samples, starting with the dispersion in toluene and ending with the preparation of the polymer matrix. But note that, in any case, the distinction between Si NCs with oxide shell and SiO_2 NPs becomes questionable if the volume of the crystalline core becomes comparable or even smaller than the volume of the oxide shell. To solve this problem, in the next chapter (chapter 7) we will investigate single Si NCs directly deposited on the substrate surface and thus we can exclude the fast oxidation process due to the dispersion of the nanoparticles in the toluene.

7 Luminescence Imaging of Individual Si Nanocrystals. Part II: Exciton Photoluminescence.

In this chapter we present the fluorescence excitation patterns which show the recombination of the quantum-confined electron-hole recombination in single Si nanocrystals. The investigated Si nanocrystals were directly deposited on the surface of the glass cover slide. We show, that using azimuthally polarized laser beam for the excitation of the nanocrystals, we can distinguish between the fluorescence excitation patterns of the defect or exciton photoluminescence.

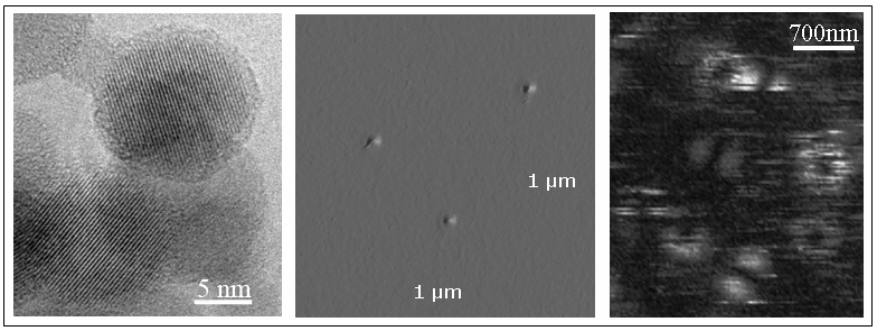

This chapter is based on:

A. I. Chizhik, A. M. Chizhik, T. Schmidt, F. Huisken and A. J. Meixner, in preparation.

Si nanocrystals were prepared by T. Schmidt (Jena University).

7.1 Introduction

Optical properties of Si NCs have been the subject of numerous studies, since it was realized that they can constitute bright light sources in the visible range, leading to potential applications in optoelectronics. Various models have been proposed to describe the mechanism of luminescence of Si NCs (see chapter 6). It is generally accepted that quantum confinement effect, which is intrinsic to the nanosized crystalline silicon, is the most accurate theory.

The spherical indirect-gap semiconductor Si/SiO_2 quantum dots with luminescence due to the electron-hole recombination possess no excitation and emission polarization [88, 89, 90], since in spherical nanoparticles the absorption and emission dipoles are uncorrelated in direction.

According to experimental results presented in literature, spherical CdSe/ZnS QDs possess 2D [3, 69, 91] emission TDM while spherical Si NCs possess 3D emission TDM [88, 90]. The reason of the dimensionality difference of the emission TDM of spherical CdSe/ZnS and spherical Si/SiO_2 QDs can be due to the different crystal structure, since the emission TDM is linked to the crystal structure. The CdSe/ZnS QDs have a wurtzite crystal structure, while Si NCs have diamond cubic structure [92]. But for both spherical CdSe/ZnS and Si/SiO_2 QDs the excitation TDM should be three-dimensional. Using for the excitation of single Si NCs CVB we should observe similar excitation fluorescence patterns, like in the case of single CdSe/ZnS QDs (see chapter 4).

In last chapter (chapter 6) we investigated samples with Si NCs which were prepared by method of spincoating. For this method of samples preparation the small amount of Si NCs powder was dispersed in toluene. We have shown that samples with single NCs prepared by this method possess only defect PL. We assume that during the dispersion in toluene, originally prepared Si NCs were oxidized and become SiO_2 NPs.

To exclude the interaction of the Si NCs with the solvent and thus fast oxidation process, we investigated single Si NCs directly deposited on the surface of the glass cover slide. In this chapter we show that some single Si NCs prepared by this method show the fluorescence patterns which correspond to the emission due to the electron-hole recombination.

7.2 Experimental

Sample preparation for single nanocrystals investigation: Free Si NCs can be produced by laser pyrolysis of silane in a gas flow reactor (see chapter 6.2). In this technique, Si NCs are extracted from the reaction volume through a conical nozzle to form a cluster beam. The NCs can be either deposited on a paper filter (see chapter 6) or can be directly deposited on the surface of the glass cover slide which was placed into the cluster beam.

For this study Si NCs were synthesized by laser pyrolysis of silane in a gas flow reactor. The Si NCs were subsequently extracted through a conical nozzle into a high-vacuum chamber. For the NCs generation the one short pulse (0,05 s) of the CO_2 laser was used. The NCs in the resulting aerosol beam were deposited on the surface of the glass cover slide. We investigated the samples with deposited Si NCs in 3 days after their production.

Figures 35 and 36 show the HRTEM and AFM images of investigated Si NCs, respectively. The HRTEM image shows that Si NCs have core/shell (crystalline Si core and amorphous SiO_2 shell) structure and possess spherical shape. AFM image shows separated single Si NCs prepared by method of direct deposition on the substrate surface.

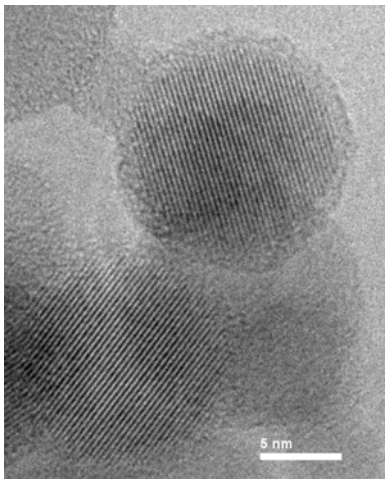

Figure 35. The HRTEM image of core/shell Si/SiO_2 nanoparticles reveals the spherical shape of the nanocrystals.

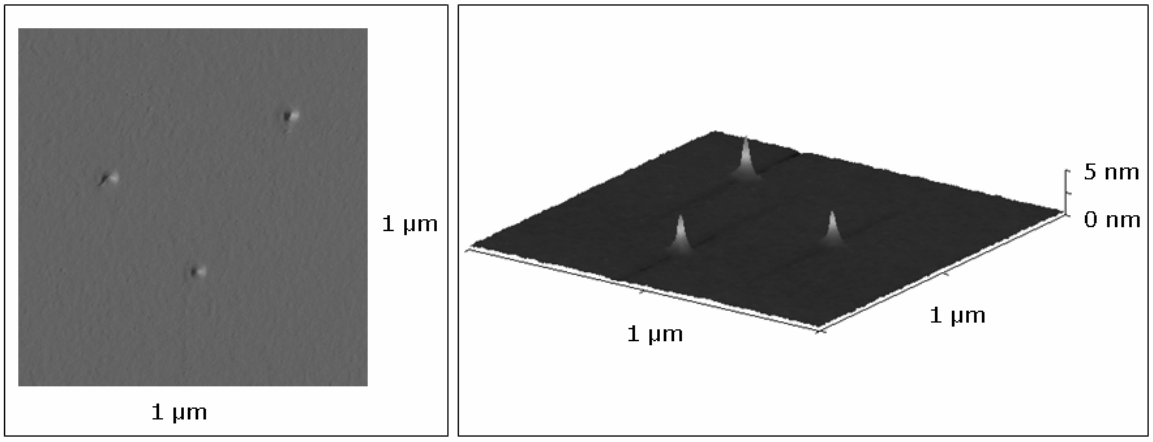

Figure 36. AFM images of three Si NCs deposited on the surface of the glass cover slide.

Microscopy: Fluorescence imaging of the single Si NCs was performed with the experimental setup sketched in Fig. 1 and described in chapter 2.1. All measurements were performed under a constant soft flow of nitrogen over the sample in order to reduce the bleaching and blinking of single Si NCs.

7.3 Fluorescence Imaging of Single Si NCs Using an Azimuthally Polarized Laser Beam

Figure 37 shows 2D (left image) and 3D (right image) fluorescence images of the 6 single Si NCs prepared by the method of direct deposition on the surface of the glass cover slide and excited with an APLB. The observed excitation patterns have two different shapes. The first type of the patterns has shape like two bright lobes with dark gap in between. These patterns correspond to the defect photoluminescence as was shown in chapters 5 and 6. The defects in silicon dioxide structure have linear excitation and emission TDM. The second type of the patterns has ring-like shape and these patterns show very fast blinking behavior. The similar patterns were observed for single CdSe/ZnS QDs after the excitation with an APLB (see chapter 4). We have shown that spherical CdSe/ZnS QDs, emitting light due to the electron-hole recombination, have 3D excitation TDM. As we have shown in the experimental chapter 7.2, the deposited Si NCs have spherical shape. According to this, we can assume, that observed ring-like

shape excitation patterns correspond to the Si NCs with emission due to the quantum-confined electron-hole recombination and these Si NCs possess 3D excitation TDM. This suggestion is in agreement with results published by Brus and coworkers [88], where they observed no excitation and emission polarization of spherical Si NCs.

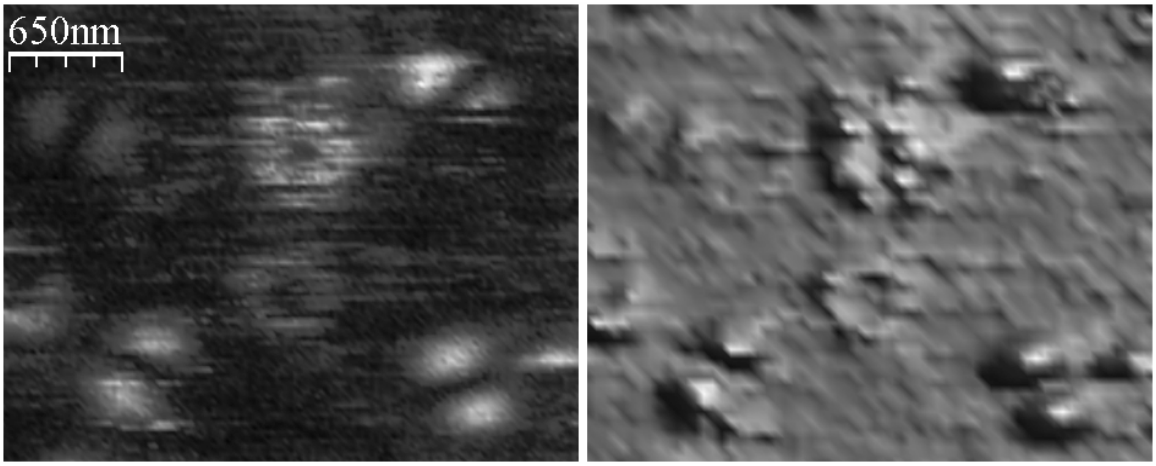

Figure 37. Fluorescence images of single Si NCs directly deposited on the surface of the glass cover slide and excited with an APLB. Left and right images show 2D and 3D fluorescence patterns of the same sample area, respectively.

The Si NCs which emit light due to the quantum-confined electron-hole recombination have significantly longer fluorescence lifetimes (from tens of μs to tens of ms) with respect to the fluorescence lifetimes of defects in silicon dioxide structure (several ns) [10, 88]. The luminescence quantum yield of these nanoparticles also was found to be very low (5.6% at room temperature) in comparison with standard rhodamine dye molecules (75% at room temperature) [88]. Thus, for the reasonable intensity of the patterns we recorded images with long acquisition time (acquisition time is 5 ms per pixel and 400 sec per image, image resolution is 200×200 pixels). The background photoluminescence can be related to the small amount of the oil from the pump which stuck to the surface of the cover slide during the deposition process of the nanoparticles.

Some of the particles with defect photoluminescence show sudden flipping of the excitation TDM during the scan (Figure 38, pattern A) or from one image to the next one. The explanation of this phenomenon was presented in chapter 5.6.

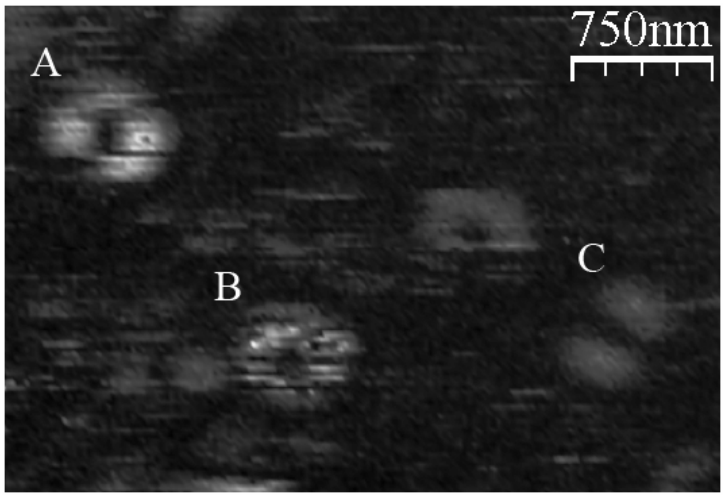

Figure 38. Fluorescence images of the Si NCs excited with an azimuthally polarized light. Fluorescence patterns of NCs **A** and **C** correspond to the defect photoluminescence, additionally NC **A** shows the sudden flipping of the TDM during the scan; pattern of NC **B** corresponds to the exciton photoluminescence.

7.4 Summary and Conclusion

In this chapter we have shown that some of the Si NCs prepared by the method of direct deposition emit light due to the quantum-confined electron-hole recombination. Using for the excitation of Si NCs an APLB, we can distinguish from the shape of the fluorescence images defect of exciton photoluminescence. We have shown that Si NCs which emit light due to the quantum confined electron-hole recombination possess 3D excitation TDM in contrast to Si NCs with defect photoluminescence which possess 1D excitation TDM.

8 Investigation of the Single Stopcock Molecules Orientation at Channel Entrances of an Organic Host-Guest Compound

In this chapter we present the investigation of the novel porphyrin-based stopcock molecules orientation in the nanochannel entrances of all-organic perhydrotriphenylene (PHTP) host-guest compounds using confocal microscopy in combination with an azimuthally polarized laser beam.

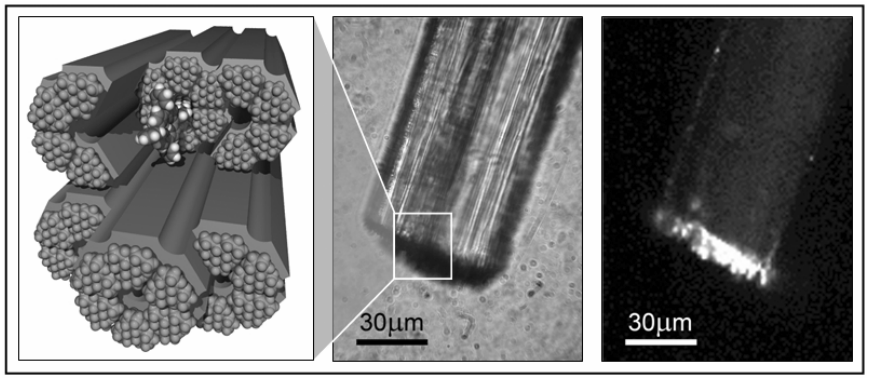

This chapter is based on:

A. M. Chizhik, R. Berger, A. I. Chizhik, A. Lyubimtsev, L. Viani, J. Cornil, S. Bär, M. Hanack, J. Hulliger, A. J. Meixner, H.-J. Egelhaaf, J. Gierschner, "Polarized Fluorescence from Single Stopcock Molecules at Channel Entrances of an All-Organic Host-Guest Compound", *Chem. Mat.*, **23(5)**, 1088–1090, **2011**. link to article page

Quantum chemical calculations were carried out by Dr. L. Viani (Mons University), PHTP crystals were synthesized by R. Berger (Bern University), stopcock molecules were synthesized by Dr. A. Lyubimtsev (Tübingen University).

8.1 Introduction

Host-guest compounds (HGCs) have gained considerable interest in the past years, since they allow the preparation of dye systems in well-defined geometries [33, 93-98]. The HGC approach provides control over the interactions between chromophores thus preserving their optical properties. In the case of zeolite based HGCs, chromophores are incorporated into the host by diffusion from the gas phase or from solution [33]. To avoid out-diffusion of guest molecules, the zeolite channels are closed by so-called stopcock molecules, which consist of two covalently linked moieties: one of them entering a channel, the other one being too large to enter and thus closing it [33]. Stopcocks may be used to provide HGCs with additional photophysical features such as directed energy transfer to/from the channel ends, thus making HGCs suitable as photon harvesting antenna systems [33]. Among *organic* channel-forming host systems, perhydrotriphenylene (PHTP) has found special attention [97-104]. Upon co-crystallization with rod-shaped guest molecules, parallel stacks of PHTP molecules form nanochannels with a diameter of about 5 Å, in which the guests are co-linearly aligned. An inter-channel distance of 15 Å ensures electronic separation of the chromophores [32, 97-103]. PHTP-based HGCs were intensively investigated in the last few years in particular with respect to their potential for long-range energy-transfer [105-107]. In contrast to the inorganic HGCs, the channels of the organic host are only formed in the presence of the guest compound, they are completely filled with guests and no cavities are found. Consequently, a strict 1D collinear arrangement of guest molecules in close van der Waals distance are found, which makes them exciting systems for both fundamental studies and as novel candidates for material science.

In this chapter, we demonstrate a first example of an all-organic PHTP-based HGC, featuring channels which are closed by stopcock molecules. The stopcock consists of a tetraphenylporphyrin substituted with a long alkoxy chain (SC-TPP; Fig. 39b), which enters the channels of PHTP. We demonstrate that using an APLB for the excitation it is possible to determine the orientation of the single stopcock molecules in the channels.

8.2 Experimental

Synthesis of stopcock molecules: The stopcock porphyrin (SC-TPP) was synthesized from 5-(4'-oxyphenyl)-10,15,20-triphenylporphin (63 mg, 0.1 mmol) with excess of 1 bromopentadecane (2 mL) in the presence of potassium carbonate (14 mg, 0.5 mmol) in *N,N*-dimethylformamide (DMF) [108]. The mixture was heated to 75 ^{o}C for 3 hours. Complete alkylation was confirmed by thin layer chromatography. After cooling, the reaction product was added to a water/methanol mixture (1:1, 20 mL), filtered off, washed thoroughly with hexane, dried, and subjected to column chromatography on silica gel with CH_2Cl_2 as eluent.

Preparation of PHTP-4,4'-dibromobiphenyl (DBBP) crystals with SC-TPP: HGCs were prepared by a temperature lowering procedure: PHTP (40 mg) was mixed with an excess of DBBP (80 mg) and dissolved in 2 ml 2-butanone by heating [109, 110]. After crystallization, 10 droplets of a diluted solution (0.1 mg/mL) of SC-TPP in 2-butanone were added at room temperature and the vial was kept 30 minutes in the dark. Afterwards, the crystals were filtered off and rinsed with methanol to remove excess stopcock material. The PHTP crystals with single molecules concentration of the SC molecules closing the channels entrances were prepared by the same procedure, but 70 mg of DBBP and 6 droplets of a highly diluted solution (0.001 mg/mL) of the stopcock molecule were used.

Spectroscopic characterization of free SC-TPP and PHTP HGCs: SC-TPP was dissolved in DCM (dichloromethane) in high dilution. The glass-air confinement sample with single molecule concentration was obtained by spin coating 10 µl of the solution in a mixture with PMMA, on a clean glass cover slide (d = 0.17 mm), giving a polymer film of 50 – 70 nm as determined by AFM. For the investigations of the horizontally oriented crystals with respect to the sample surface, PHTP HGCs were placed on the surface of a clean glass cover slide.

Microscopy: Fluorescence imaging of the HGCs was performed with the experimental setup sketched in Fig. 1 and described in chapter 2.1. PHTP-crystals were imaged by digital optical microscope (VHX-600, Keyence) with dual light high-magnification zoom lens (VH-Z250R, Keyence). For the polarization microscopy

experiments the emission of the stopcock molecules included in the channels of the crystals was observed through a linear polarizer and its intensity was recorded as a function of the rotation angle of the polarizer.

Calculations: The ground-state geometry of TPP was optimized using density functional theory (DFT) imposing the highest possible point group symmetry (C_{2h}) for the non-planar conformation of unsubstituted TPP (i.e., without the alkoxy substituent). Energies, orientations and intensities of the lowest excited states were obtained within the time-dependent (TD) DFT formalism. In all cases the B3LYP functional and the 6-311G* basis set was used within the Gaussian03 programme package [111].

8.3 Density Functional Theory Calculations

The gas-phase structure and electronic properties of SC-TPP were investigated by (time dependent) density functional theory ((TD-)DFT) calculation, see Fig. 39b. The phenyl rings are strongly twisted against the porphyrin core by $\theta_1 = 73°$ (with a small barrier of 0.7 kJ/mol at $\theta_1 = 90°$; the barrier at 0° is far above kT, due to strong steric hindrance). The TDMs of the transitions from the ground state to the states S_1 (with an energy of E = 1.84 eV and an oscillator strength of $f = 0.06$) and S_2 (E = 1.96 eV, $f = 0.16$) are perpendicular to each other, pointing through the opposite amine and imine functionalities of the SC-TPP core, respectively. Upon introducing the alkoxy substituent into one of the phenyl groups, the TDMs of the first two states are slightly tilted by 1° and 5° within the plane of the TPP core, respectively. Rotation of the alkyl chain around the C_{phenyl}-O bond results in two energetically equivalent conformations of SC-TPP at torsion angles of $\theta_2 = 0°$ and $\theta_2 = 180°$ (with respect to the plane of the phenyl ring). The rotational barrier of 15 kJ/mol at $\theta_2 = 90°$ between these two conformations is well above kT, so that the O-C_{alkyl} bond is preferentially found in a plane perpendicular to the TPP core. Rotation of the alkyl chain around the C_{alkyl}-O bond is almost unhindered at room temperature, having a barrier of only 1.2 kJ/mol at 32° with respect to the *trans*-configuration.

8.4 Single Stopcock Molecules in the Glass-Air Confinement

Single stopcock molecules were characterized in a polymer matrix (PMMA) prior to inclusion, using confocal microscopy under APLB excitation [4]. The image in Fig. 39a reveals significant differences between the emission intensities of different molecules, which are mainly related to the different tilts of the molecular TDMs with respect to the sample surface. One of the molecules (at the bottom-left corner) shows the effect of sudden bleaching which proves the emitters to be single molecules. Only two lobe patterns were observed indicating that no aggregations of the molecules were formed.

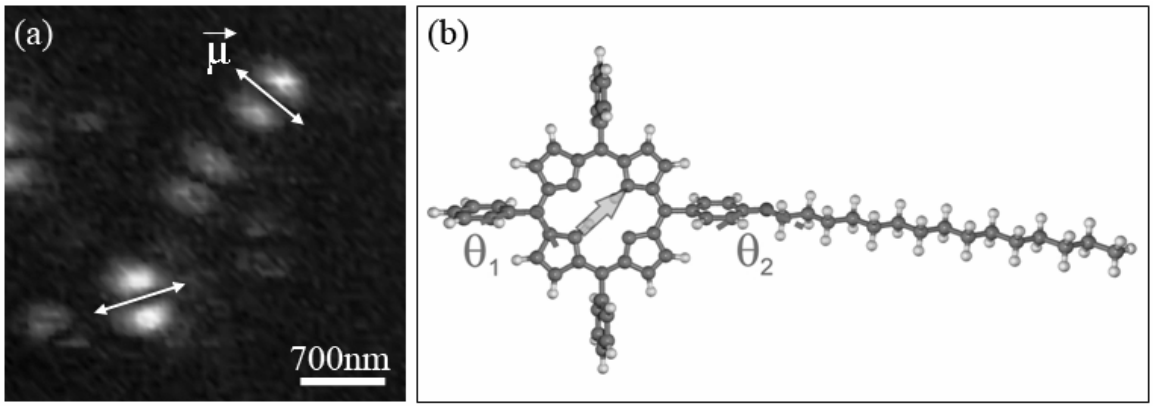

Figure 39. (a) Fluorescence microscopy image of six isolated TPP-SC molecules in PMMA, excited by APLB. The arrows indicate the orientation of the TDM projection on the sample surface. (b) DFT optimized geometry of TPP-SC. The arrow indicates the direction of the TDM. θ_1 indicates the torsion angle between the planes of the phenyl ring and the TPP core. θ_2 indicates the torsion angle between the plane of the phenyl ring and the O-C_{alkyl} bond.

8.5 PHTP – Crystals without Stopcock Molecules

PHTP-DBBP crystals without stopcock molecules were imaged by a digital optical microscope (Fig. 40). They were found to be between 3 and 50 μm in diameter (0.1 to 2 mm in length). The channel ends show a certain distribution in space along the *c*-axis of the crystal, with some of the channel entrances being dislocated up to several

tens of µm from the crystal basis. A weak uniform background fluorescence signal is detected (Fig. 41f) whose spectrum is identical to that of pure PHTP powder.

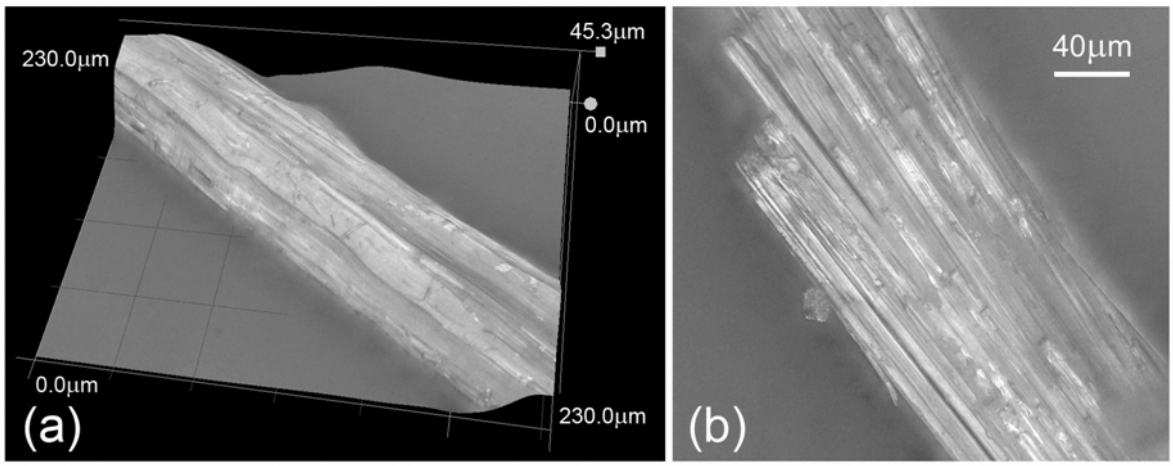

Figure 40. Geometrical structure of a PHTP-crystal recorded by digital optical microscope. (a) 3-dimensional structure of the central part of the crystal. (b) A photo of the end of the crystal, resolving a multi step structure of the channel entrances.

8.6 PHTP – Crystals with Stopcock Molecules

PHTP-DBBP crystals with stopcock molecules (PHTP-SC) were investigated by recording optical (Fig. 41a, c) and fluorescence (Fig. 41b, d) images. Strong fluorescence is emitted from the bases of the crystals, whereas the prismatic faces exhibit significantly lower intensity. This is quantified by the line scans in Figs. 42a and 42b, which confirm that the emission is concentrated at the channel ends. Light guiding effects can be excluded as a reason for this observation, since inclusion compounds without stopcock molecules, but with chromophores in the channels, did not show enhanced emission from the crystal ends [112]. Further evidence for the concentration of stopcocks at the channel ends arises from the comparison of the line scans through the crystals with low and high loading of the stopcock molecules (Fig. 42). In crystals with low loading of the fluorophores, the emission is limited to the channel ends (Fig. 42a and 42b). For crystals with high loading, where all outer surfaces are covered by adsorbed fluorophores, the intensity profile is homogeneous along the crystal axis (Fig. 42c and 42d). Even after thorough washing of the crystals, adsorption might still occur at cracks present at the

surface as demonstrated by the fluorescence image of a small crystal (length ca 20 μm) with a rather inhomogeneous surface structure (Fig. 41c, 41d). However, the effect is rather minor as shown by the comparison of the fluorescence spectra in Fig. 41e, demonstrating the background emission from the middle of the crystal which essentially corresponds to the emission of pure PHTP (Fig. 41f, solid line). In contrast, the emission from the end of the crystal originates mainly from TPP.

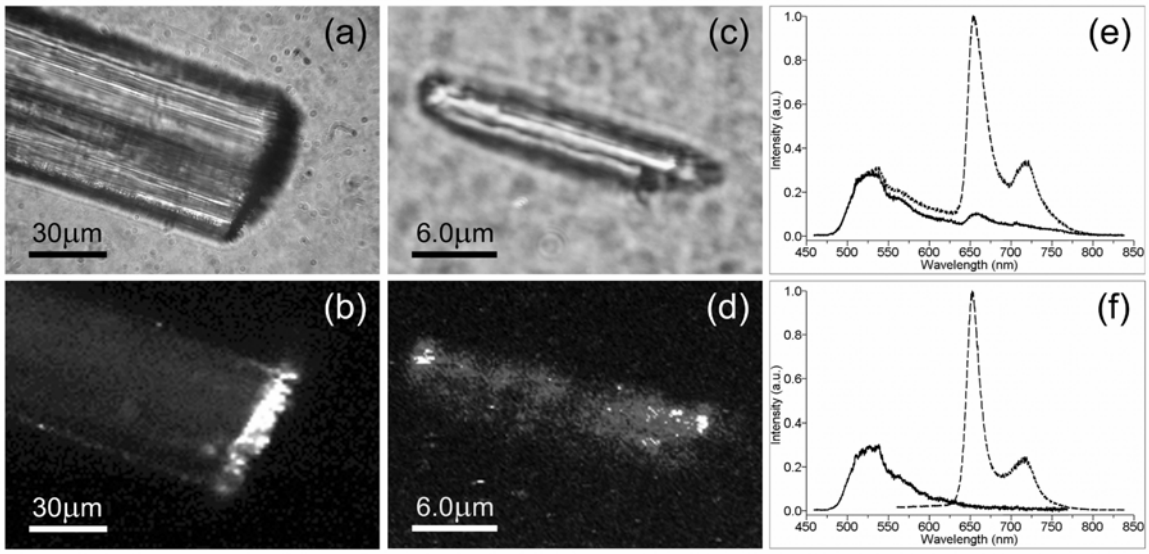

Figure 41. Optical (a, c) and fluorescence images (b, d) of a large (a, b) and a small (c, d) PHTP crystal with included stopcock (SC) molecules. e) Normalized fluorescence spectra acquired at the end (dashed curve) and at the middle part (solid curve) of a crystal. f) Emission spectra of SC molecules in PMMA (dashed curve) and of a stopcock-free PHTP crystal (solid curve).

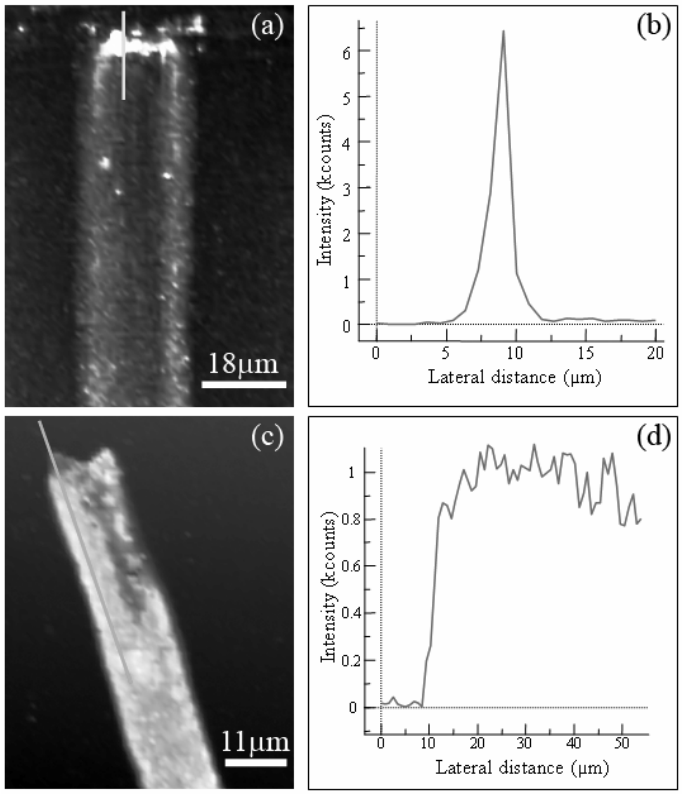

Figure 42. a) Fluorescence image of a single PHTP – crystal with included stopcock molecules; b) emission intensity along the line indicated on the left; c) fluorescence image of an a single PHTP – crystal with stopcock molecules covering the surface of the crystal; d) emission intensity along the line indicated on the left.

8.7 Distribution of the Stopcock Molecules in the Channels

The thickness of the investigated crystals typically exceeded the size of our objective lens focal spot. Hence, one fluorescence scan exhibits the signal only from particular cut off of the crystal. At the same time this allowed us to carry out a reconstruction of spatial distribution of stopcock molecules at the whole surface of the crystal by recording a series of fluorescence images and stepwise shifting the objective

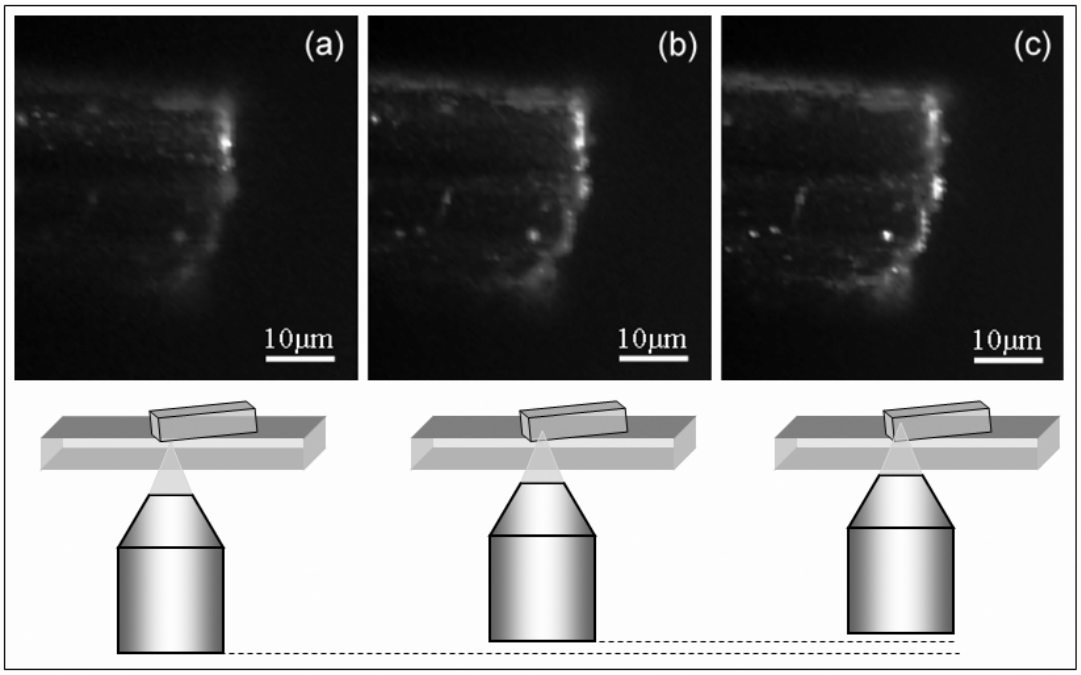

Figure 43. Fluorescent images series of a single crystal on a cover slide with included stopcock molecules, acquired at different positions of the focal plane. (a) The focal plane is located at the border cover slide/crystal. For images (b) and (c), the focus was moved upwards by about 300 nm and 600 nm, respectively.

lens focal plane throughout the whole crystal end. Figure 43 shows a series of fluorescence images acquired at three different focal plane levels, from the bottom towards the central part of the crystal. In the case when the laser beam is focused on the boundary between the cover slide and the crystal, we collect the emission mainly from the bottom face of the crystal (Fig. 43a), while the central part is out of focus. Shifting of the focal plane further to 300 nm (Fig. 43b) and 600 nm (Fig. 43c) towards the crystal centre allows the imaging of the following cutoffs of the crystal. Bright features located in the central part of the crystal which are clearly pronounced in Figure 43c are related to emission of SC molecules, included in the channels having the entrances not at the end of the crystal. Thus obtained images form three-dimensional distribution of included SC molecules.

8.8 PHTP – Crystals with Single Stopcock Molecules

More detailed information on the insertion of the stopcock molecules into the channels of PHTP is provided by the APLB technique described above, which yields the orientation of the porphyrin TDM (S_1) with respect to the axis of the channel into which the alkoxy tail of the SC-TPP is inserted. For SC-TPP molecules which are not included in the channels, a random distribution of TDM orientations is expected. Evaluation of the two lobe patterns (Fig. 44) with respect to their orientation against the crystal axis yields a ratio of parallel to perpendicular orientations of the TDM vs. the crystal axis of about 2:1, whereas intermediate orientations, i.e., with both parallel and perpendicular components, are hardly observed. This observation might be explained by the fact that the crystal basis is not a smooth planar surface but that some channels stick out more than others. TPP cores whose alkyl chains are inserted in protruding channels will attach face-on to the crystal basis. This leads to projections of the TDMs which are perpendicular to the crystal axis. TPP cores whose alkyl chains are inserted in channels, which are surrounded by protruding ones, will adsorb to the side walls of adjacent protruding channels. The resulting projections of the TDMs will be preferentially parallel to the crystal axis.

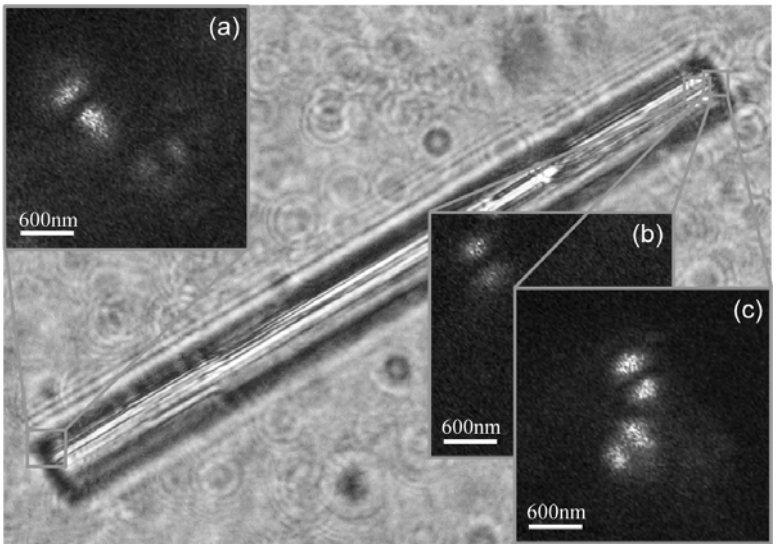

Figure 44. Fluorescence patterns of single stopcock molecules closing the channel entrances of PHTP crystal excited with APLB. The background is an optical image of the PHTP-SC-TPP crystal.

Statistical Analysis: We analyzed 51 excitation patterns of different single stopcock molecules, included into crystal channels and excited with an APLB. In this case the fluorescence patterns show the projection of the TDM on the sample surface. Since focused an APLB has only the in-plane field component, different orientation of the single molecule TDM results in different excitation efficiency of the emitter (see chapter 2). The dipoles which are oriented horizontally on the sample surface can be efficiently excited, while the dipoles possessing vertical orientation cannot be excited, and therefore, invisible in the excitation pattern. From 51 observed fluorescence patterns, 15 show that the TDMs of the molecules have orientation perpendicular to the crystal axis and 36 – parallel to the crystal axis. The stopcock molecules which are attached face-on to the crystal basis can possess any orientation of the TDM within the plane, perpendicular to the crystal axis (i.e., when the projection of the TDM on the sample surface is perpendicular to the crystal axis). According to our estimation only dipoles which are tilted under the angle within the range from 0° to 47° with respect to the sample surface, can be detected on the average background signal. Therefore, near half of the molecules which are attached face-on to the crystal basis are invisible on the excitation patterns. Thus we can double the number of the detected dipoles, oriented perpendicularly to the crystal axis, which gives us the ratio 30:36. Obtained values show that the ratio between the molecules possessing the TDM perpendicular to the crystal axis and those, parallel to the crystal axis is near 1:1.

8.9 Crystals Oriented Vertically with Respect to the Sample Surface

For the investigations of the crystals which are oriented vertically with respect to the sample surface the special holder made from two cover slides was used. One cover slide was glued on the surface of the second cover slide under 90° angle (Fig. 45a). The single crystals were fixed with optical glue (Norland Optical Adhesive, Norland Products) on the surface of the perpendicular standing cover slide vertically with respect to the second cover slide surface. To exclude the influence of the optical glue to the crystal basis with absorbed stopcock molecules, only upper crystal edge was glued to the cover slide surface. The crystals with different sizes oriented vertically with respect to the

sample surface were investigated (Fig. 45a). Figure 45b and 45c shows the optical and fluorescence images of the single crystal basis with included stopcock molecules into the channels, respectively.

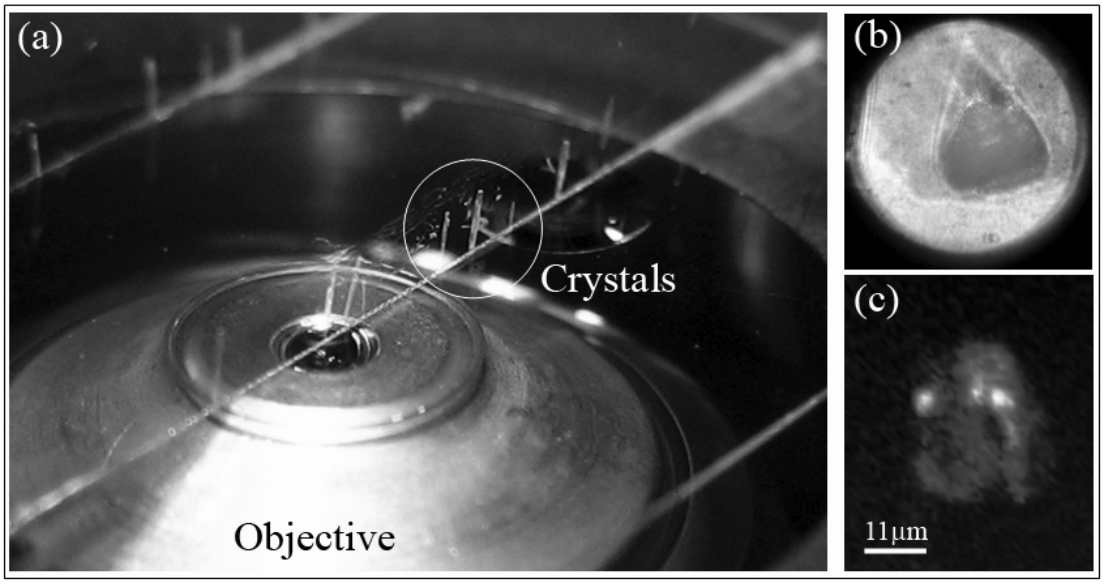

Figure 45. (a) The photo of the crystals oriented vertically with respect to the sample surface. (b), (c) An optical and fluorescence images of the crystal basis, respectively.

For a parallel orientation of the crystal axis with respect to the laser beam (i.e., perpendicular to the substrate surface), we observed completely depolarized emission (Fig. 46) showing the absence of one particular preferable direction of the SC molecules TDMs projection on the surface perpendicular to the crystal axis. According to expectations, this result demonstrates that the SC molecules, attached face-on to the crystal basis can possess any projection of the TDM on the surface, perpendicular to the crystal axis.

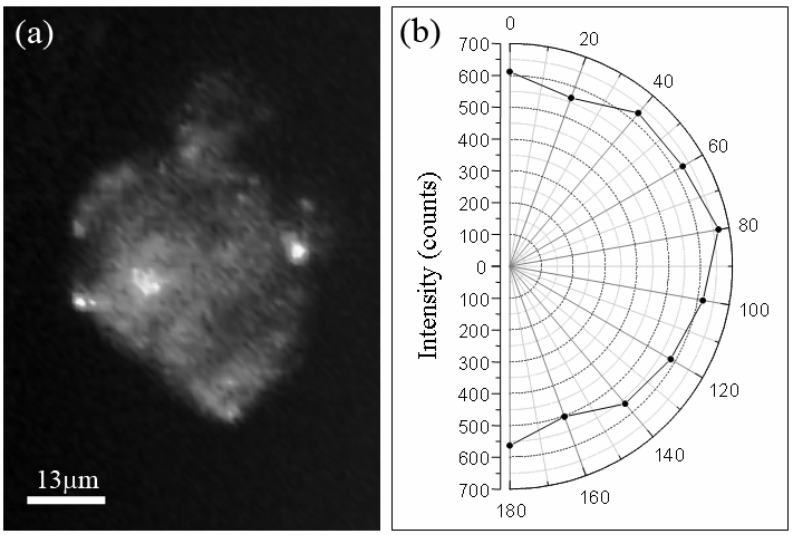

Figure 46. (a) Fluorescence image of the basis of the vertically oriented PHTP crystal with included SC molecules. The crystal axis has a parallel orientation with respect to the laser beam. (b) The emission of the included SC molecules was observed through a linear polarizer and emission intensity was recorded as a function of the rotation angle of the polarizer. The result presented in polar coordinates shows that the emission is completely depolarized.

8.10 Summary and Conclusion

In conclusion, we have prepared the first example of an all-organic channel-forming host-guest-compound where the channel entrances are closed by porphyrin based molecular stopcocks. The localization of the stopcocks in the channel entrances was confirmed by confocal microscopy in combination with an APLB. We found two possible ways of the stopcock molecules to close the channel entrances of the crystals: TPP cores of the stopcock molecules adsorb to the side walls of adjacent protruding channels and TPP cores whose alkyl chains are inserted in protruding channels attach face-on to the crystal basis.

9 Investigation of the Single CdSe/ZnS Quantum Dots Orientation in the Channels of Porous Silica Beads

In this chapter we present the results on investigation of CdSe/ZnS quantum dots included into the channels of the mesoporous silica beads. The silica beads with different concentration of the QDs in the channels were investigated. We show that using an azimuthally polarized laser beam for the excitation, the 2D orientation of included single QDs excitation TDM can be determine.

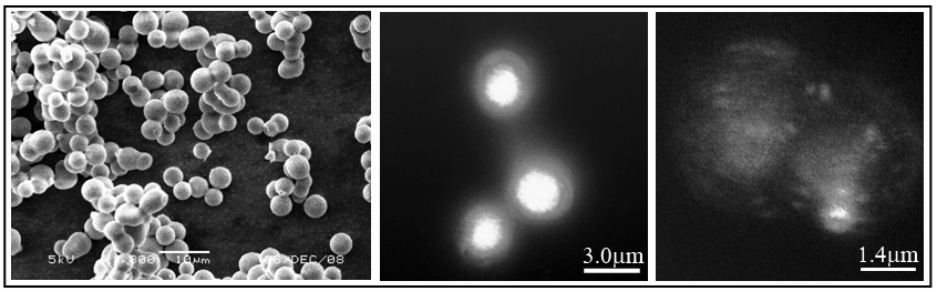

This chapter is based on:

A. M. Chizhik, A. I. Chizhik, J. H. Ramm, D. Brühwiler, A. J. Mexner, H.-J. Egelhaaf, J. Gierschner, in preparation.

and

J. H. Ramm, PhD Thesis, University of Zürich, **2010**.

Mesoporous silica beads were synthesized by Dr. J. H. Ramm (Zürich University).

9.1 Introduction

Due to their size-tunable properties, semiconductor quantum dots (QD) received much attention concerning potential applications in the field of optoelectronics [113], solar cells [114, 115], light emitting devices [116], or biosensing [117] and biolabeling [118, 119]. QDs offer a narrow, tunable symmetric emission spectrum [117, 120, 121]. A decrease of the QD size results in an increase of the separation between the energy levels. This change in the electronic structure can be followed by detection of the emission wavelength. A coating of QDs with a passivation layer such as ZnS [122], CdSe [122], CdS [123] or ZnSe [124] increases the quantum efficiency. CdSe QDs which are capped with ZnS feature increased quantum efficiency exceeding 50% and additionally show decreased toxicity [125]. To avoid coagulation, which would affect the luminescence properties, the surface is typically coated with a hydrophobic organic group containing bulky (C8-C18) alkyl moieties (mostly tri-n-octylphosphine oxide (TOPO)) [126, 127].

The combination of mesoporous materials and QDs offers interesting possibilities in terms of organization and confinement. Research efforts have focused on the in-situ synthesis of QDs in mesoporous silicas [128, 129]. Inclusion in nanofibers of porous alumina and the doping in large pore size silica materials were studied as well. The mesoporous material provides a stable and accessible surface with well defined pore size distribution for the loading of QDs. An additionally well defined morphology offers possibilities for the investigation of the properties of single QDs inside the silica by means of confocal microscopy in combination with cylindrical vector beams.

9.2 Experimental

Preparation of mesoporous silica beads for the inclusion of the QDs: In order to prepare a material for optical studies, commercially available CdSe/ZnS QDs with a hydrophobic coating (PlasmaChem GmbH, Berlin) were used. A silica material with well defined morphology and large pores was employed as a host. Therefore, a SBA-15 (Santa Barbara Amorphous) type material with pore sizes between 20 and 24 nm was synthesised by adding mesitylene (TMB) as a swelling agent. The morphology of the particles was controlled by adjusting the amount of KCl and TMB in the synthesis to achieve spherical particles as described in the literature [130]. An adequate environment

for the hydrophobic QDs was prepared by grafting octadecyltrimethoxysilane (ODTMS) to the silica surface. The QDs exhibit a size of 2 to 7 nm. The SBA-15 type silica features a pore size of about 18 nm to 19 nm after the functionalization (L S/Od-1/-2) and offers sufficient space for an inclusion of the QDs. Grafting of ODTMS causes a reduction of the pore size of approximately 4 nm. Different amounts of QDs were included by varying the concentration of the dispersions. SEM images showed spherical particles of sizes between 1 and 5 μm (Figure 47). However, extensive treatment with 1-butanol during the loading and washing seemed to cause a partial decomposition of the spherical particles.

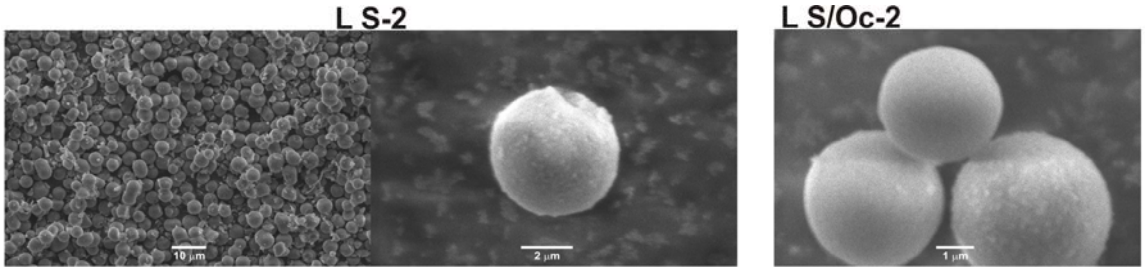

Figure 47. SEM images of large pore size SBA-15 before (left) and after (right) grafting of ODTMS.

Inclusion of the QDs in the porous of the silica beads: Under continuous stirring and ultrasonification (~5 min), a weighed quantity of typically about 1 mg of CdSe/ZnS QDs (PlasmaChem GmbH, Berlin) was dispersed in 1 mL of chloroform. This stock solution was diluted to a specific concentration and a distinct amount of this dispersion was added to a mixture of 50 mg of ODTMS functionalized SBA in 5 mL of 1-butanol. The mixture was stirred for 24 h, the solvent was removed by centrifugation and the product was washed two times by dispersing in 5 mL of 1-butanol and removal of the solvent by centrifugation. The product was dried at 60 °C overnight.

Sample preparation for single QDs investigation: All samples with single CdSe/ZnS QDs were prepared by the method of spincoating (see chapter 2.1).

Sample preparation for single mesoporous silica beads with/without QDs investigation: All samples with single mesoporous silica beads were prepared by method of spincoating (see chapter 2.1). The ethanol was used for the dispersion of the silica beads powder. To fix the beads on the surface of the cover slide the polymer layer (PMMA) was additionally spin coated on top of the sample.

Microscopy: Fluorescence imaging of the single QDs and mesoporous silica beads was performed with the experimental setup sketched in Fig. 1 and described in chapter 2.1.

9.3 Single Quantum Dots in the Glass-Air Confinement

Figure 48 shows the SEM image of the single QDs, possessing elongated shape.

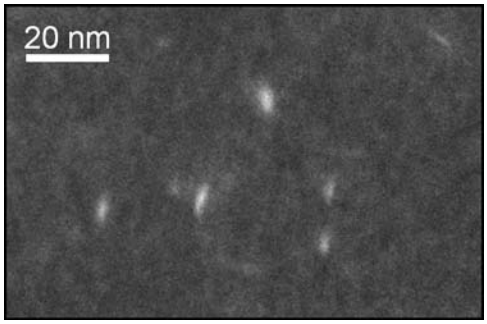

Figure 48. SEM image of the CdSe/ZnS quantum dots reveals the elongated shape of the nanocrystals.

As was described in the experimental part of this chapter (9.2), to include QDs in the channels of silica beads and to wash the surface of silica beads after the inclusion, the beads were dispersed in 1-butanol. For the samples preparation for the confocal microscopy measurements the silica beads with the included QDs were dispersed in ethanol. The 1-butanol and ethanol are polar solvents in contrast with the non-polar chloroform which was used for the dispersion of QDs before the inclusion into the porous of the beads. The polar solvents were used to exclude the out diffusion of the QDs from the porous. The polar solvents can change the photophysical properties of the QDs, especially when the shape of the QDs is not spherical, but elongated [131]. For example, during the dispersion in the polar solvent, some negative charges from the solvent can attach the surface of the QDs and influence on the excitation TDM. The TDM can change the dimensionality from 3D to 1D and can have the orientation along the *c*-axis of the crystal.

We investigated the excitation TDM of elongated QDs after the dispersion in the polar solvent and ultrasonification during 5-10 min. The DCM (dichlormethan) was used as the solvent for the preparation of the samples with single QDs for the confocal

microscopy measurements. Figure 49a shows the excitation fluorescence patterns of the single QDs excited with APBL. Surprisingly, all patterns have shape like two bright lobes with dark gap in between in contrast to the toluene or water soluble QDs (see chapter 4). Based on this observation, we can suggest that investigated elongated QDs dispersed in DCM possess 1D excitation TDM, since the fluorescence patterns have two lobe shapes. The same QDs dispersed in the toluene show usual fluorescence patterns like it was shown in chapter 4.

Figure 49b shows the typical emission spectrum of single CdSe/ZnS QDs embedded in PMMA matrix (for the sample preparation by method of spin coating, QDs were dispersed in DCM). The maximum of the emission at 610 nm corresponds to the electron-hole recombination energy, which is in agreement with the emission wavelength specified by the producer of the QDs. This means that the dispersion of the QDs in the polar solvent does not affect the emission of the nanoparticles.

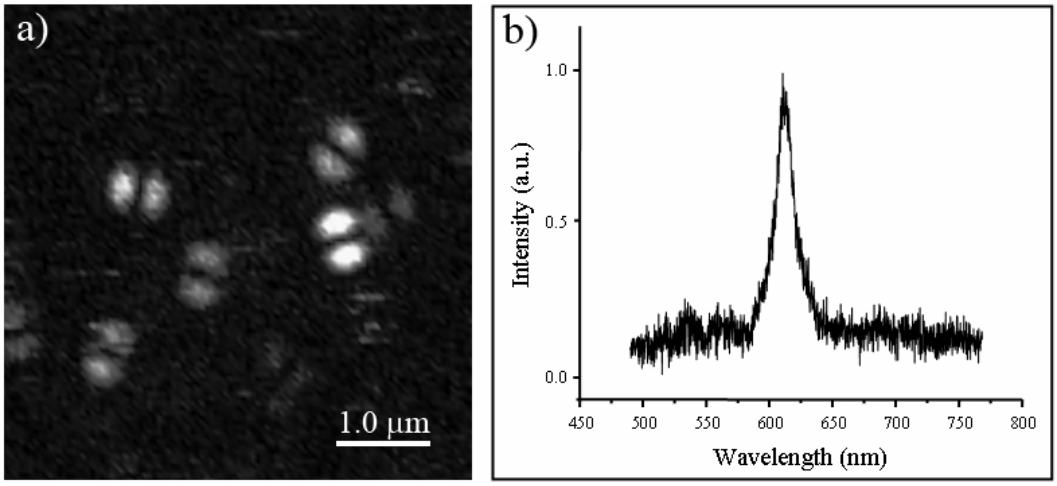

Figure 49. (a) Fluorescence excitation patterns obtained upon excitation of single CdSe/ZnS quantum dots with an APBL and (b) emission spectrum of single CdSe/ZnS quantum dot embedded in PMMA matrix.

9.4 Porous Silica Beads without and with Quantum dots in the Channels

The fluorescence images and normalized emission spectra of two porous silica beads without QDs are presented in Figure 50 (left). The emission spectrum has a broadened shape with a maximum around 550 nm. The photoluminescence is assigned to oxygen related defect sites [132]. Different colors indicate spectra which were recorded

one after another (from 1 to 4) from the same area of the silica bead. Fast bleaching of the emission was observed.

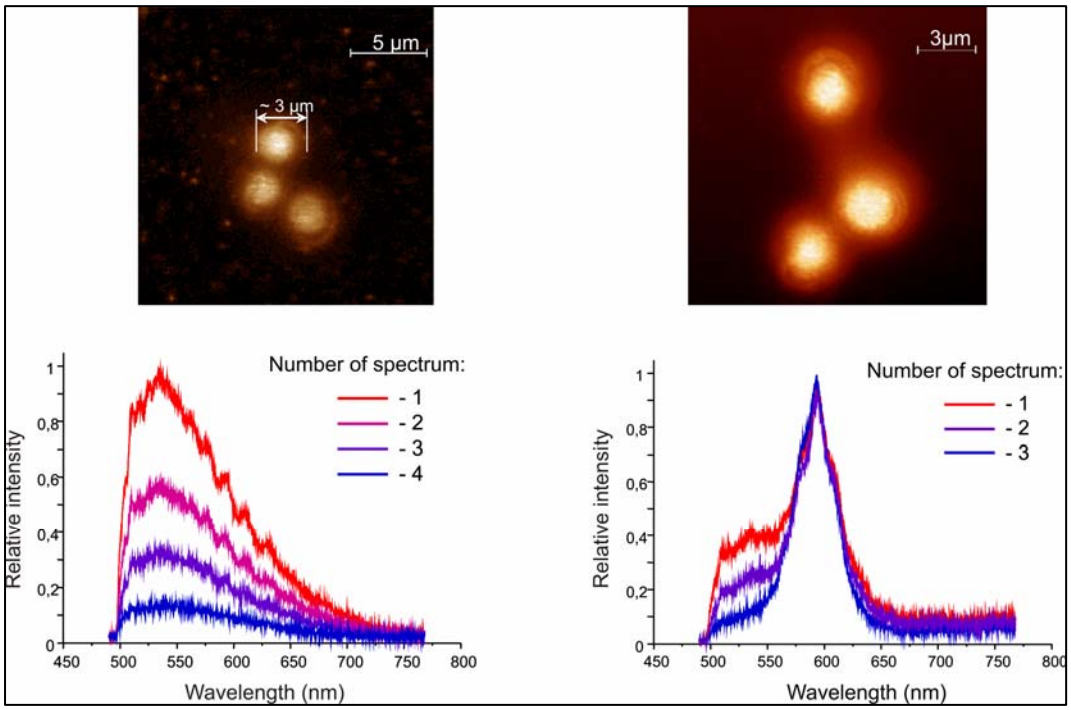

Figure 50. Fluorescence images and spectra of silica spheres without (left) and with (right) CdSe/ZnS QDs in the channels.

Figure 50 (right) shows the fluorescence images and normalized emission spectra of three porous silica bead with high concentration of included QDs in the channels. The emission spectra exhibit a maximum with a shoulder: the maximum at 610 nm, corresponding to the emission of included QDs and the shoulder at around 520 nm, corresponding to the emission of the porous silica. The spectra were acquired one after another from the same area of the bead. The emission from the quantum dots exhibit significantly lower bleaching that the signal from the porous silica.

9.5 Porous Silica Beads with Single Quantum Dots in the Channels

Figure 51 shows fluorescence images of single porous silica beads with different concentrations of the included QDs. The left image displays two porous silica beads with relatively high concentration of QDs in the channels. The right image shows two porous

silica beads with low concentration of the included QDs. The double lobe excitation patterns of single QDs (like in the case of the QDs in glass-air confinement, see chapter 9.3) in the channels of silica spheres were observed. High concentration was achieved by adsorption from dispersion with 2.7 mg/L and low concentration from 6.3 ng/L of QDs.

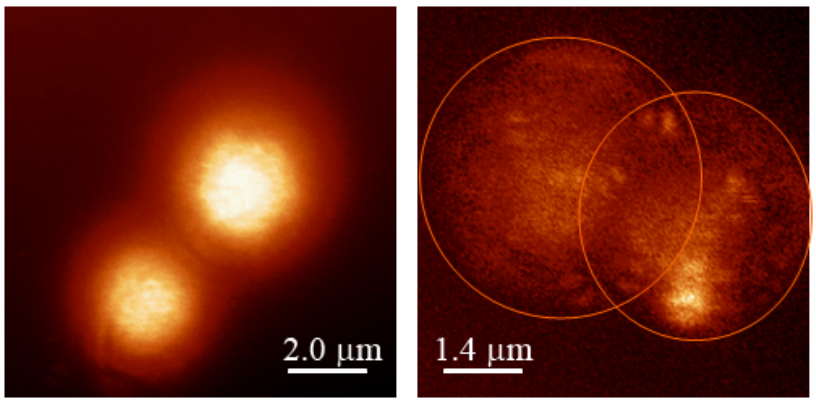

Figure 51. Fluorescence images of silica spheres with different concentration of CdSe/ZnS QDs in the channels excited with an APLB.

9.6 Distribution of the Quantum Dots in the Channels

Due to the dimensions of the silica beads it is not possible to acquire the complete picture of the single QDs distribution in a single scan. However, the spatial distribution of the QDs in the channels can be reconstructed by stepwise *z*-scanning, thus collecting fluorescence images from different cross-sections of the silica bead. Figure 52 shows a series of fluorescence images acquired at five different levels, from the bottom to the central part of a silica bead with included QDs in the channels. Figure 52(1) gives the fluorescence image acquired with the laser beam focused on the boundary between the glass cover slide and the silica bead. The images shown in Figure 52(2-5) correspond to the shift of the focal plane upwards by about 30 nm, 60 nm, 90 nm and 110 nm, respectively. Using this method, a complete picture of the distribution of QDs throughout the whole silica bead can be acquired.

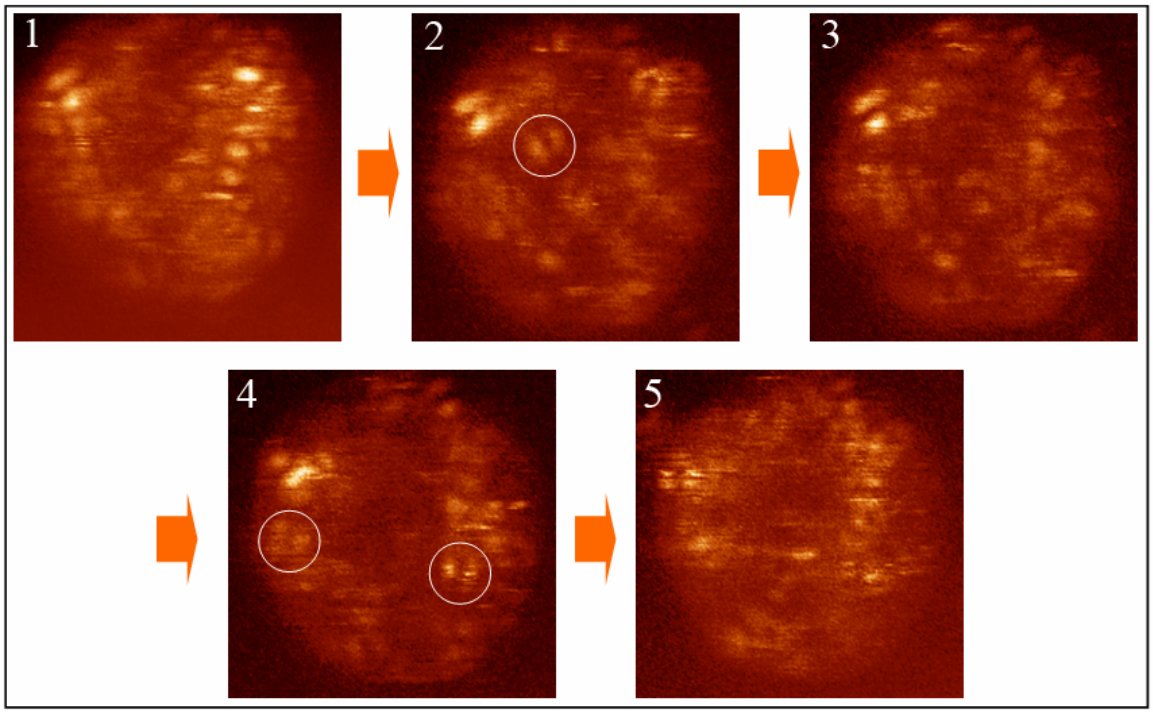

Figure 52. Fluorescence images of single silica bead with loaded CdSe/ZnS QDs at different *z*-position of the focal plane: (1) z = 0 nm, (2) z = 30 nm, (3) z = 60 nm, (4) z = 90 nm, (5) z = 110 nm, excited with an APLB. The size of each image is 2×2 μm.

9.7 Summary and Conclusion

A loading of the porous silica beads with QDs in different concentrations was accomplished as was shown by confocal microscopy measurements. Single QDs could be detected by fluorescence imaging. However, measurement of the orientation of elongated QDs relative to the channel system requires their inclusion arrays of silica nanochannels [133]. First experiments with hexagonal fibers were problematic due to their relatively small pore size (2.9 nm). A successful approach would require small (less than 3 nm) QDs coated with short alkyl groups or monodirectional silica channels with larger pore sizes. In addition we have shown that slightly elongated QDs solved in the polar solvent change the dimensionality of the excitation TDM from 3D to 1D and thus the shape of the fluorescence patterns also changes. This result needs further investigation.

List of the Abbreviations:

AFM – atomic force microscopy
APD – avalanche photo diode
APLB – azimuthally polarized laser beam

CCD – charge-coupled device
CVB – cylindrical vector beams

DC – defect centre
DCM – dichlormethan

HRTEM – high resolution transmission electron microscopy
H_2Pc – metal-free phthalocyanine

NA – numerical aperture
NC – nanocrystal
NMR – nuclear magnetic resonance
NP – nanoparticle

OEP – octaethylporphyrin

PHTP – perhydrotriphenylene
PI – perylene derivative N-(2,6-diisopropylphenyl)-perylene-3,4-dicarboxymide
PL – photoluminescence
PMMA – poly(methyl-methacrylate)
PS – polystyrene
PVA – polyvinyl alcohol

RPLB – radially polarized laser beam
R6G – rhodamine 6G

SEM – scanning electron microscopy
SC – stopcock

TDM – transition dipole moment
TEM – transmission electron microscopy
TPP – tetraphenylporphyrin

QD – quantum dot
QC – quantum confinement

3D – three dimensional
2D – two dimensional
1D – one dimensional

References:

Chapter 1

[1] J. Jasny, J. Sepioł, *Chem Phys Lett*, 273, 444, **1997**.

[2] M. Böhmer, J. Enderlein, *J. Opt. Soc. Am. B*, 20, 554, **2003**.

[3] S. A. Empedocles, R. Neuhauser, M. G. Bawendi, *Nature*, 339, 126, **1999**.

[4] L. Novotny, M. R. Beversluis, K. S. Youngworth, T. G. Brown, *Phys. Rev. Lett.*, 86, 5251, **2001**.

[5] H. Ishitobi, I. Nakamura, N. Hayazawa, Z. Sekkat, S. Kawata, *J. Phys. Chem. B*, 114, 2565, **2010**.

[6] R. Gutbrod, D. Khoptyar, M. Steiner, A. M. Chizhik, A. I. Chizhik, S. Baer, A. J. Meixner, *Nano Lett.*, 10, 504, **2010**.

[7] D. Khoptyar, R. Gutbrod, A. Chizhik, J. Enderlein, F. Schleifenbaum, M. Steiner, A. J. Meixner, *Opt. Express*, 16, 9907, **2008**.

[8] R. Gutbrod, A. I. Chizhik, A. M. Chizhik, D. Khoptyar, A. J. Meixner, *Opt. Lett.*, 34, 629, **2009**.

[9] A. I. Chizhik, R. Gutbrod, A. M. Chizhik, S. Bär, A. J. Meixner, *Proc. SPIE*, 7396, 73960F, **2009**.

[10] A. M. Chizhik, A. I. Chizhik, R. Gutbrod, A. J. Meixner, T. Schmidt, J. Sommerfeld, F. Huisken, *Nano Lett.*, 9, 3239, **2009**.

[11] A. M. Chizhik, T. Schmidt, A. I. Chizhik, F. Huisken, A. J. Meixner, *Proc. SPIE*, 7393, 739305, **2009**.

[12] A. V. Failla, H. Qian, H. Qian, A. Hartschuh, A. J. Meixner, *Nano Lett.*, 6, 1374, **2006**.

[13] M. Fleischer, D. Zhang, K. Braun, S. Jäger, R. Ehlich, M. Häffner, C. Stanciu, J. K. H. Hörber, A. J. Meixner, D. P. Kern, *Nanotechnology*, 21, 065301, **2010**.

[14] H. Piwonski, C. Stupperich, A. Hartschuh, J. Sepiol, A. Meixner, J. Waluk, *J. Am. Chem. Soc.*, 127, 5302, **2005**.

[15] H. Piwonski, A. Hartschuh, N. Urbanska, M. Pietraszkiewicz, J. Sepiol, A. J. Meixner, J. Waluk, *J. Phys. Chem. C*, 113, 11514, **2009**.

[16] T. Züchner, A. V. Failla, A. Hartschuh, A. J. Meixner, *J. Microsc.*, 229, 337, **2008**.

Chapter 2

[17] R. Dorn, S. Quabis, G. Leuchs, *Phys. Rev. Lett.*, 91, 233901, **2003**.

[18] M. A. Lieb, Ph.D. Thesis, University of Siegen, **2001**.

[19] I. Horcas, R. Fernandez, J. M. Gomez-Rodriguez, J. Colchero, J. Gomez-Herrero, A. M. Baro, *Rev. Sci. Instrum.*, 78, 013705, **2007**.

[20] K. Yonezawa, Y. Kozawa, S. Sato, *Opt. Lett.*, 31, 2151, **2006**.

[21] G. Machavariani, Y. Lumer, I. Moshe, A. Meir, S. Jackel, N. Davidson, *Appl. Opt.*, 46, 3304, **2007**.

[22] J. F. Bisson, J. Li, K. Ueda, Y. Senatsky, *Opt. Express*, 14, 3304, **2006**.

[23] M. A. Ahmed, A. Voss, M. M. Vogel, T. Graf, *Opt. Lett.*, 32, 3272, **2007**.

[24] V. G. Niziev, R. S. Chang, A. V. Nesterov, *Appl. Opt.*, 45, 8393, **2006**.

[25] M. Stalder, M. Schadt, *Opt. Lett.*, 21, 1948, **1996**.

[26] A. V. Failla, S. Jäger, T. Züchner, M. Steiner, A. J. Meixner, *Opt. Express*, 15, 8532, **2007**.

[27] G. Machavariani, Y. Lumer, I. Moshe, A. Meir, S. Jackel, *Opt. Lett.*, 32, 1468, **2007**.

[28] L. Novotny, B. Hecht, Principles of nano-optics, Cambridge University Press, Cambridge, UK, **2006**.

[29] Q. Zhan, J. R. Leger, *Opt. Express*, 10, 324, **2002**.

[30] Q. Zhan, *Adv. Opt. Photon.*, 1, 1, **2009**.

[31] P. J. Langley, J. Hulliger, *Chem. Soc. Rev.*, 28, 279, **1999**.

[32] G. Srinivasan, J. A. Villanueva-Garibay, K. Müller, D. Oelkrug, B. Mili´an Medina, D. Beljonne, J. Cornil, M. Wykes, L. Viani, J. Gierschner, R. Martinez-Alvarez, M. Jazdzyk, M. Hanack, H.-J. Egelhaaf, *Phys. Chem. Chem. Phys.*, 11, 4996, **2009**.

[33] G. Calzaferri, S. Huber, H. Maas, C. Minkowski, *Angew. Chem. Int. Ed.*, 42, 3732 **2003**.

Chapter 3

[34] P. Gregory, *J. Porphyrins Phthalocyanines*, 4, 432, **2000**.

[35] M. Ochsner, *J. Photochem. Photobiol. B*, 39, 1, **1997**.

[36] D. Phillips, *Pure Appl. Chem.*, 67, 117, **1995**.

[37] J. J. Schuitmaker, P. Baas, H. L. L. M. van Leengoed, F. W. van der Meulen, W. M. Star, N. van Zandwijk, *J. Photochem. Photobiol. B*, 34, 3, **1996**.

[38] I. Lanzo, N. Russo, E. Sicilia, *J. Phys. Chem. B*, 112, 4123, **2008**.

[39] A. Renn, U. P. Wild, A. Rebane, *J. Phys. Chem. A*, 106, 3045, **2002**.

[40] www.porphyrin-systems.de (14.05.2009).

[41] B. Wehrle, H. H. Limbach, M. Köcher, O. Ermer, E. Vogel, *Angew. Chem. Int. Ed. Engl.*, 26, 934, **1987**.

[42] Y.-D. Wu, K. W. K. Chan, C.-P. Yip, E. Vogel, D. A. Plattner, K. N. Houk, *J. Org. Chem.*, 62, 9240, **1997**.

[43] H. H. Limbach, J. M. Lopez, A. Kohen, *Phil. Trans. R. Soc. B*, 361, 1399, **2006**.

[44] M. J. Crossley, M. M. Harding, S. Sternhell, *J. Org. Chem.*, 53, 1132, **1988**.

[45] J. Braun, R. Schwesinger, P. G. Williams, H. Morimoto, D. E. Wemmer, H. H. Limbach, *J. Am. Chem. Soc.*, 118, 11101, **1996**.

[46] J. Braun, H. H. Limbach, P. G. Williams, H. Morimoto, D. E. Wemmer, *J. Am. Chem. Soc.*, 118, 7231, **1996**.

[47] M. J. Crossley, M. M. Harding, S. Sternhell, *J. Am. Chem. Soc.*, 108, 3608, **1986**.

[48] M. J. Crossley, L. D. Field, M. M. Harding, S. Sternhell, *J. Am. Chem. Soc.*, 109, 2335, **1987**.

[49] A. Vdovin, J. Waluk, B. Dick, A. Slenczka, *ChemPhysChem*, 10, 761, **2009**.

[50] P. Fita, N. Urbanska, C. Radzewicz, J. Waluk, *Chem. Eur. J.*, 15, 4851, **2009**.

[51] J. Waluk, E. Vogel, *J. Phys. Chem.*, 98, 4530, **1994**.

[52] M. Drobizhev, N. S. Makarov, A. Rebane, G. de la Torre, T.Torres, *J. Phys. Chem. C*, 112, 848, **2008**.

[53] S. Völker, J. H. van der Waals, *Molecular Phys.*, 32, 1703, **1976**.

[54] U. Even, J. Jortner, *J. Chem. Phys.*, 77, 4391, **1982**.

[55] K. M. Merz Jr., C. H. Reynolds, *J. Chem. Soc. Chem. Comm.*, 90, **1988**.

[56] S. Bär, A. I. Chizhik, R. Gutbrod, F. Schleifenbaum, A. M. Chizhik, A. J. Meixner, *Anal. Bioanal. Chem.*, 396, 3, **2010**.

[57] M. J. F. Calvete, Ph.D. Thesis, University of Tübingen, **2004**.

[58] N. S. Dudkina, P. A. Shatunov, E. M. Kuvshinova, S. G. Pukhovskaya, A. S. Semeikin, O. A. Golubchikov, *Russ. J. Gen. Chem.*, 68, 1955, **1998**.

[59] M. J. Frisch, G. W. Trucks, H. B. Schlegel, G. E. Scuseria, M. A. Robb, J. R. Cheeseman, J. A. Montgomery, Jr., T. Vreven, K. N. Kudin, J. C. Burant, et al. *Gaussian 03*, revision E.01; Gaussian, Inc.: Wallingford, CT, **2004**.

[60] T. Strenalyuk, S. Samdal, H. V. Volden, *J. Phys. Chem. A*, 112, 4853, **2008**.

[61] D. K. Maity, T. N. Truong, *J. Porphyrins Phthalocyanines*, 5, 289, **2001**.

[62] K. A. Nguyen, R. Pachter, *J. Phys. Chem. A*, 104, 4549, **2000**.

Chapter 4

[63] A. P. Alivisatos, *J. Phys. Chem.*, 100, 13226, **1996**.

[64] A. L. Efros, M. Rosen, *Annu. Rev. Mater. Sci.*, 30, 475, **2000**.

[65] A. D. Yoffe, *Adv. Phys.*, 50, 1-208, **2001**.

[66] M. Nirmal, B. O. Dabbousi, M. G. Bawendi, J. J. Macklin, J. K. Trautman, T. D. Harris, L. E. Brus, *Nature*, 383, 802, **1996**.

[67] A. Issac, C. von Borczyskowski, F. Cichos, *Phys. Rev. B*, 71, 161302, **2005**.

[68] N. Herron, J. C. Calabrese, W. E. Farneth, Y. Wang, *Science*, 259, 1426, **2001**.

[69] R. Schuster, M. Barth, A. Gruber, F. Cichos, *Chem.Phys. Lett.*, 413, 280, **2005**.

[70] P. Frantsuzov, M. Kuno, B. Jankó, and R. A. Marcus, *Nat. Phys.*, 4, 519, **2008**.

[71] W. G. J. H. M. van Sark, P. L. T. M. Fredrix, A. A. Bol, H. C. Gerritsen, A. Meijerink, *ChemPhysChem*, 3, 871, **2002**.

Chapter 5

[72] L. T. Canham, *Appl. Phys. Lett.*, 57, 1046, **1990**.

[73] V. Lehmann, U. Gösele, *Appl. Phys. Lett.*, 58, 856, **1991**.

[74] S. M. Prokes, *Appl. Phys. Lett.*, 62, 3244, **1993**.

[75] Y. Kanemitsu, S. Okamoto, M. Otobe, S. Ota, *Phys. Rev. B*, 55, R7375, **1997**.

[76] A. G. Cullis, L. T. Canham, P. D. J. Calcott, *J. Appl. Phys.*, 82, 909, **1997**.

[77] S. Godefroo, M. Hayne, M. Jivanescu, M. Stesmans, M. Zacharias, O. I. Lebedev, G. van Tendeloo, V. V. Moshchalkov, *Nature Nanotech.*, 3, 174, **2008**.

[78] U. Gösele, *Nature Nanotech.*, 3, 134, **2008**.

[79] G. Ledoux, J.Gong, F.Huisken, O.Guillois, C. Reynaud, *Appl. Phys. Lett.*, 80, 4834, **2002**.

[80] M. V. Wolkin, J. Jorne, P. M. Fauchet, G. Allan, C. Delerue, *Phys. Rev. Lett.*, 82, 197, **1999**.

[81] J. Martin, F. Cichos, F. Huisken, C. von Borczyskowski, *Nano Lett.*, 8, 656, **2008**.

[82] A. Colder, F. Huisken, E. Trave, G. Ledoux, O. Guillois, C. Reynaud, H. Hofmeister, E. Pippel, *Nanotechnology*, 15, L1, **2004**.

[83] F. Huisken, H. Hofmeister, B. Kohn, M. A. Laguna, V. Paillard, *Appl. Surf. Sci.*, 154, 305, **2000**.

[84] F. Huisken, G. Ledoux, O. Guillois, C. Reynaud, *Adv. Mater.*, 14, 1861, **2002**.

Chapter 6

[85] J. Heitmann, F. Müller, M. Zacharias, U. Gösele, *Adv. Mater.*, 17, 795, **2005**.

[86] B. Delley, E. F. Steigmeier, *Phys. Rev. B*, 47, 1397, **1993**.

[87] A. Puzder, A. J. Williamson, J. C. Grossman, G. Galli, *Phys. Rev. Lett.*, 88, 097401, **2002**.

[88] L. E. Brus, P. F. Szajowski, W. L. Wilson, T. D. Harris, S. Schuppler, P. H. Citrin, *J. Am. Chem. Soc.*, 117, 2915, **1995**.

[89] D. Kovalev, H. Heckler, G. Polisski, F. Koch, *Phys. Stat. Sol. (b)*, 215, 871, **1999**.

Chapter 7

[90] L. Brus, Light Emission in Silicon, edited by D. J. Lockwood, Semiconductors and Semimetals, Academic Press, New York, **1996**.

[91] D. Patra, I. Gregor, J. Enderlein, *Appl. Phys. Lett.*, 87, 101103, **2005**.

[92] F. Koberling, U. Kolb, G. Philipp, I. Potapova, T. Basche´, A. Mews, *J. Phys. Chem. B*, 107, 7463, **2003**.

Chapter 8

[93] A. Ajayaghosh, S. J. George, V. K. Praveen, *Angew. Chem. Int. Ed.*, 42, 332, **2003**.

[94] F. J. M. Hoeben, P. Jonkheijm, E. W. Meijer, A. P. H. J. Schenning, *Chem. Rev.*, 105, 149, **2005**.

[95] A. D. Guerzo, A. G. L. Olive, J. Reichwagen, H. Hopf, J.-P. Desvergne, *J. Am. Chem. Soc.*, 127, 17984, **2005.**

[96] J. S. Wilson, M. J. Frampton, J. J. Michels, L. Sardone, G. Marletta, R. H. Friend, P. Samorí, H. L. Anderson, F. Cacialli, *Adv. Mater.*, 17, 2659, **2005**.

[97] P. J. Langley, J. Hulliger, *Chem. Soc. Rev.*, 28, 279, **1999**.

[98] G. Couderc, J. Hulliger, *Chem. Soc. Rev.*, 39, 1545, **2010**.

[99] A. Lyubimtsev, M. N. Misir, M. Celvete, M. Hanack, *Eur. J. Org. Chem.*, 3209, **2008**.

[100] M. M. Tsotsalas, K. Kopka, G. Luppi, S. Wagner, M. P. Law, M. Schfers, L. De Cola, *ACS Nano*, 4, 342, **2010**.

[101] D. Brühwiler, G. Calzaferri, T. Torres, J. H. Ramm, N. Gartmann, L.-Q. Dieu, I. López-Duarte, M. V. Martínez-Díaz, *J. Mater. Chem.*, 19, 8040, **2009**.

[102] J. Gierschner, L. Lüer, D. Oelkrug, E. Musluoglu, B. Behnisch, M. Hanack, *Adv. Mater.*, 12, 757, **2000**.

[103] J. Gierschner, H.-J. Egelhaaf, H.-G. Mack, D. Oelkrug, R. Martinez Alvarez, M. Hanack, *Synth. Met.*, 137, 1449, **2003**.

[104] M. Aloshyna, B. Milián Medina, L. Poulsen, J. Moreau, D. Beljonne, J. Cornil, G. Di Silvestro, M. Cerminara, F. Meinardi, R. Tubino, H. Detert, S. Schrader, H.-J. Egelhaaf, C. Botta, J. Gierschner, *Adv. Funct. Mater.*, 18, 915, **2008**.

[105] L. Poulsen, M. Jazdzyk, J.-E. Communal, J. C. Sancho-García, A. Mura, G. Bongiovanni, D. Beljonne, J. Cornil, M. Hanack, H.-J. Egelhaaf, J. Gierschner, *J. Am. Chem. Soc.*, 129, 8585, **2007**.

[106] L. Viani, L. Poulsen, M. Jazdzyk, G. Patrinoiu, F. Cordella, A. Mura, G. Bongiovanni, C. Botta, D. Beljonne, J. Cornil, M. Hanack, H.-J. Egelhaaf, J. Gierschner, *J. Phys. Chem. B.*, 113, 10566, **2009**.

[107] C. Botta, G. Patrinoiu, P. Picouet, S. Yunus, J.-E. Communal, F. Cordella, F. Quochi, A. Mura, G. Bongiovanni, M. Pasini, S. Destri, G. Di Silvestro, *Adv. Mater.*, 16, 1716, **2004**.

[108] J. Hulliger, *Angew. Chem. Int. Ed. Engl.*, 33, 143, **1994**.

[109] E. Brule, Y. R. de Miguel, K. K. Hii, *Tetrahedron*, 60, 5913, **2004**.

[110] A. S. Semeikin, S. A. Syrbu, O. L. Koifman, *Izv. Vyssh. Uchebn. Zaved., Khim. Khim. Tekhnol.*, 47, 46, **2004**.

[111] M. J. Frisch et al, *Gaussian 2003, Revision C.02*, Gaussian Inc.: Pittsburgh PA, **2003**.

[112] J. Hulliger, O. König, R. Hoss, *Adv. Mater.*, 7, 719, **1995**.

Chapter 9

[113] C. J. Murphy, *Anal. Chem.*, 74, 520A, **2002**.

[114] U. H. Wendy, P. Xiaogang, A. P. Alivisatos, *Adv. Mater.*, 11, 923, **1999**.

[115] N. C. Greenham, X. Peng, A. P. Alivisatos, *Phys. Rev. B*, 54, 17628, **1996**.

[116] S. Coe, W.–K. Woo, M. Bawendi, V. Bulovic, *Nature*, 420, 800, **2002**.

[117] W. C. W. Chan, D. J. Maxwell, X. H. Gao, R. E. Bailey, M. Y. Han, S. M. Nie, *Current Opinion in Biotechnology*, 13, 40, **2002**.

[118] A. P. Alivisatos, *Nat. Biotechnol.*, 22, 47, **2004**.

[119] A. P. Alivisatos, *Science*, 271, 933, **1996**.

[120] W. C. W. Chan, S. Nie, *Science*, 281, 2016, **1998**.

[121] M. Bruchez Jr., M. Moronne, P. Gin, S. Weiss, A. P. Alivisatos, *Science*, 281, 2013, **1998**.

[122] A. R. Kortan, R. Hull, R. L. Opila, M. G. Bawendi, M. L. Steigerwald, P. J. Carroll, L. E. Brus, *J. Am. Chem. Soc.*, 112, 1327, **2002**.

[123] X. Peng, M. C. Schlamp, A. V. Kadayanich, A. P. Alivisatos, *J. Am. Chem. Soc.*, 119, 7019, **1997**.

[124] C. F. Hoener, K. A. Allan, A. J. Bard, A. Campion, M. A. Fox, T. E. Mallouk, S. E. Weber, J. M. White, *J. Phys. Chem.*, 96, 3812, **2002**.

[125] M. A. Hines, P. Guyot-Sionnest, *J. Phys. Chem.*, 100, 468, **1996**.

[126] G. Kalyuzhny, R. W. Murray, *J. Phys. Chem. B*, 109, 7012, **2005**.

[127] M. Kuno, J. K. Lee, B. O. Dabbousi, F. V. Mikulec, M. G. Bawendi, *J. Chem. Phys.*, 106, 9869, **1997**.

[128] H. Parala, H. Winkler, M. Kolbe, A. Wohlfart, R. A. Fischer, R. Schmechel, H. v. Seggem, *Adv. Mater.*, 12, 1050, **2000**.

[129] H. Winkler, A. Birkner, V. Hagen, I. Wolf, R. Schmechel, H. v. Seggem, R. A. Fischer, *Adv. Mater.*, 11, 1444, **1999**.

[130] L. Wang, T. Qi, Y. Zhang, J. Chu, *Microporous Mesoporous Mater.*, 91, 156, **2006**.

[131] U. T. D. Thuy, N. Q. Liem, D. X. Thanh, M. Protière, *Appl. Phys. Lett*, 91, 241908, **2007**.

[132] M. E. Gimmon-Kinsel, K. Groothuis, K. J. Balkus Jr., *Microporous Mesoporous Mater.*, 20, 67, **1998**.

[133] Y. Kievsky, I. Sokolov. IEEE *Trans. Nanotechnol.*, 4, 490, **2005.**

A Acknowledgment

My supervisors **Prof. Dr. Alfred J. Meixner** (University of Tübingen), **Dr. Johannes Gierschner** (University of Tübingen, IMDEA Nanoscience) and **Dr. Hans-Joachim Egelhaaf** (University of Tübingen, Konarka Technologies) for stimulating discussions and numerous valuable advices. I would also like to thank **Prof. Dr. Alfred J. Meixner** for providing laboratory and equipment for the investigations. I am grateful to **Dr. Johannes Gierschner** and **Dr. Hans-Joachim Egelhaaf** for organizing the Nanomatch project, which gave me a great opportunity to gain significant scientific experience.

Dipl.-Phys. Alexey Chizhik (University of Tübingen) for his continuous support during my PhD and stimulating discussions.

Dr. Wolfgang Langer (University of Tübingen) and **Juliette Ruddy** (University of Tübingen) for a lot of help with solving administrative and bureaucratic problems.

All members of the **Nano Optics group**, **Tübingen University** for fruitful discussions and the team work.

NANOMATCH Project, European Commission through the Human Potential Program (Marie-Curie Research Training Network NANOMATCH, Contract No. MRTN-CT-2006-035884) **for financial support during three years of my PhD.**

Collaborators:

Prof. Friedrich Huisken, **Dipl.-Phys. Torsten Schmidt**, **Dipl.-Phys. Karsten Potrick** and **Dipl.-Phys. Jana Sommerfeld** (University of Jena) for very fruitful collaboration, interesting discussions and providing the Si NCs and SiO_2 NPs for the measurements which are described in chapter 5, 6 and 7.

Prof. Michael Hanack and **Dr. Alexey Lubimtsev** (University of Tübingen) for providing the OEP molecules (chapter 3), as well as for their interest in my work.

Prof. Jürg Hulliger and **Dipl.-Chem. Ricarda Berger** (University of Bern) for providing the PHTP-crystals with stopcock molecules (chapter 8) and stimulating discussions.

Dr. Jérome Cornil and **Dr. Lucas Viani** (University of Mons) for quantum chemical calculations presented in chapter 8.

Dr. Dominik Brühwiler and **Dr. Jan Hinrich Ramm** (Universityof Zürich) for the providing the porous silica beads with included QDs (chapter 9).

Dr. Hans-Georg Mack (University of Tübingen) for quantum chemical calculations presented in chapter 3 and fruitful discussions.

Dipl.-Chem Regina Jäger (University of Tübingen) for her help with the investigations of the tautomerism process in OEP molecules (chapter 3).

Prof. Dr. Oliver Eibl and **Zainul Aabdin** (University of Tübingen) for TEM and SEM images of single CdSe/ZnS quantum dots.

Moreover, I would like to thank:

My parents **Mikhail** and **Irina Litkevich** for their continuous support.

B Abstract

In this study we investigate photo-physical and photo-chemical properties of single molecules and semiconductor quantum dots by imaging their excitation transition dipole moment (TDM) using confocal microscopy combined with azimuthally and radially polarized laser beams. We show that using this technique the three-dimensional (3D) orientation, dimensionality and dynamical effects of excitation TDM of single quantum emitters can be determined.

The work can be divided into the three main parts:

1. The determination of 3D TDM orientation and study of the tautomerism process in single dye molecules.

2. The investigation of direct/indirect band gap semiconductor single quantum dots and single silicon dioxide nanoparticles.

3. The study of host-guest compounds: the orientation of the guest molecules or quantum dots in the channels of host compounds.

Each of the chapters presents independent topic of the research. In chapter 1, we introduce and motivate the research described in this work and define the scope of this thesis. Chapter 2 gives an overview of the experimental methods and equipment used in this study. Each chapter starts with an introduction of the object of the research and experimental part which refers to the specific instrumentation briefly presented in chapter 2.1.

In chapters 3, we investigate the changing of the TDM orientation during the excited-state tautomerism process in single metal-free phthalocyanine and porphyrin molecules. In the case of phthalocyanine molecules the fluorescence excitation patterns show that the angle between the transition dipole moments of the two trans forms is near 90^{o}. Most of porphyrin molecules exhibit the absence of the tautomerism process, while for 7% of the total number of investigated molecules we observe excitation patterns of two different trans forms of the same single molecule. Experimental results are in good agreement with theoretical prediction based on quantum chemical calculations.

In chapter 4, we investigate the excitation TDM of the single CdSe/ZnS quantum dots (QD). We study different types of commercially available water/toluene soluble QDs. We show that single CdSe/ZnS QDs possess 3D excitation TDM in contrast to dye

molecules which possess linear excitation TDM. We demonstrate that using the cylindrical vector beams we can determine the dimensionality of the excitation TDM. Investigated QDs show characteristic dynamical effects featuring single QDs such as fluorescence intermittency (blinking and bleaching).

In chapter 5, we study single SiO_2 nanoparticles (NPs) which possess defect luminescence. The obtained results clearly demonstrate the presence of the one-dimensional TDM of SiO_2 NPs. Moreover, image series of the same sample area revealed the possibility for some silica NPs to change their TDM orientation from one image to another.

In chapter 6 and 7, we investigate single Si/SiO_2 core-shell nanocrystals (Si NCs) produced by laser pyrolysis. In chapter 6, we study samples with single Si NCs embedded in polymer matrix which were prepared by method of spin coating. In chapter 7, we study the Si NCs which were directly deposited on the surface of the glass cover slide. We show that samples with Si NCs prepared by method of spin coating possess defect photoluminescence, while some of directly deposited Si NCs possess emission due to the quantum confined electron-hole recombination. We demonstrate that Si NCs with defect photoluminescence possess linear excitation TDM, while Si NCs with exciton photoluminescence - 3D excitation TDM.

In chapters 8 and 9, we demonstrate that the orientation of the single quantum emitters can be determined not only in polymer layer spin coated on the glass cover slide surface but, for example, inside the nanochannels of host materials. We investigate two different types of host-guest compounds. In chapter 8, we show the ability of new type of stopcock molecules close the channels of the organic crystals. Using an azimuthally polarized laser beam we determine the single stopcock molecules orientation in the nanochannel entrances of the crystals.

In chapter 9, we study mesoporous silica beads with included CdSe/ZnS QDs in the channels. The beads with different concentration of the QDs included in the channels were investigated. Using an azimuthally polarized laser beam for the sample excitation we determine the orientation of single QDs in the channels of mesoporous silica beads.

C Zusammenfassung

In dieser Arbeit untersuchen wir fotophysikalische und fotochemische Eigenschaften einzelner Moleküle und Halbleiterquantenpunkte durch Abbildung ihrer Anregungs- Übergangsdipolmomente (transition dipole moments TDMs) mit konfokaler Mikroskopie in Kombination mit azimutal und radial polarisierten Laserstrahlen. Wir zeigen, dass mit dieser Technik die dreidimensionale (3D) Orientierung, Dimensionalität und dynamische Effekte des Anregungs-TDM einzelner Quantenemitter bestimmt werden können.

Die Arbeit kann in drei Hauptabschnitte unterteilt werden:

1. Die Bestimmung der 3D TDM-Orientierung und Untersuchung der Tautomerieprozesse in einzelnen Farbstoffmolekülen.

2. Die Untersuchung direkter/indirekter Bandlücken in Halbleiterquantenpunkten und einzelnen Siliziumdioxidnanopartikeln.

3. Die Analyse von Wirt-Gast-Systemen: Orientierung der Gastmoleküle oder Quantenpunkte in den Kanälen der Wirtsteilchen.

In Kapitel 1 führen wir in die Forschung dieser Arbeit ein und definieren den Rahmen. Kapitel 2 gibt einen Überblick über die experimentellen Methoden und die Ausstattung, die in dieser Studie verwendet werden. Die folgenden Kapitel stellen unabhängige Forschungsgebiete dar. Jedes Kapitel beginnt mit einer Einleitung über das entsprechende Forschungsobjekt und den experimentellen Teil, der sich auf die in Kapitel 2.1 kurz beschriebene Messtechnik bezieht.

In Kapitel 3 untersuchen wir die Änderung der TDM-Orientierung während der Tautomerie im angeregten Zustand in einzelnen metallfreien Phthalocyanin- und Porphyrinmolekülen. Im Falle der Phthalocyaninmoleküle zeigen die Fluoreszenzanregungsmuster, dass der Winkel zwischen den Übergangsdipolmomenten der beiden trans-Formen etwa 90° beträgt. Die meisten Porphyrinmoleküle weisen keine Tautomerie auf, während wir für 7% aller untersuchten Moleküle Anregungsmuster von zwei unterschiedlichen trans-Formen desselben einzelnen Moleküls beobachten. Die Versuchsergebnisse stimmen gut mit den theoretischen Erwartungen, basierend auf quantenchemischen Berechnungen, überein.

In Kapitel 4 untersuchen wir das Anregungs-TDM der einzelnen CdSe/ZnS Quantenpunkte (quantum dots QDs). Wir erforschen verschiedene Arten kommerziell erhältlicher, in Wasser/Toluol löslicher QDs. Wir zeigen, dass einzelne CdSe/ZnS QDs ein 3D Anregungs-TDM besitzen, im Gegensatz zu Fluoreszenzmolekülen, die ein lineares Anregungs-TDM besitzen. Wir zeigen auf, dass wir unter Verwendung der zylindrischen Vektorstrahlen die Dimensionalität des Anregungs-TDM bestimmen können. Untersuchte QDs weisen charakteristische dynamische Effekte einzelner QDs auf wie Fluoreszenzperiodizität (Blinken und Bleichen).

In Kapitel 5 analysieren wir einzelne SiO_2 Nanopartikel (NPs), die Defektlumineszenz aufweisen. Die Ergebnisse zeigen eindeutig die Anwesenheit des eindimensionalen TDM von SiO_2 NPs. Darüberhinaus decken Bilderserien derselben Probenbereiche die Wahrscheinlichkeit auf für einige Silica NPs die Orientierung ihres TDM von einer Aufnahme zur nächsten zu ändern.

In den Kapiteln 6 und 7 erforschen wir einzelne, mit Laserpyrolyse hergestellten, Si/SiO_2 Kern-Hülle-Nanokristalle (Si NKs). In Kapitel 6 untersuchen wir Proben mit einzelnen Si NKs eingebettet in einer Polymermatrixt, die mit dem spin-coating-Verfahren hergestellt wurden. In Kapitel 7 untersuchen wir Si NKs, die direkt auf die Oberfläche der Deckgläschen gebracht wurden. Wir zeigen, dass Proben mit Si NKs, die mit Hilfe des spin-coating-Verfahrens hergestellt wurden, Defektlumineszenz aufweisen, während einige der direkt aufgebrachten Si NKs Emission aufgrund quantenbegrenzter Elektron-Loch-Rekombination besitzen. Wir zeigen, dass Si NKs mit Defektlumineszenz ein lineares Anregungs-TDM besitzen, jedoch Si NKs mit Excitonenfotolumineszenz 3D Anregungs-TDM.

In den Kapiteln 8 und 9 legen wir dar, dass die Orientierung einzelner Quantenemitter nicht nur in einer Polymerschicht, aufgeschleudert auf die Deckgläschenoberfläche, bestimmt werden kann, sondern z.B. innerhalb der Nanokanäle von Wirtsmaterialien. Wir untersuchen zwei unterschiedliche Arten von Wirt- Gast-Systemen. In Kapitel 8 zeigen wir die Eigenschaft einer neuen Art von Stopcockmolekülen die Kanäle der organischen Kristalle zu schließen. Mit einem azimutal polarisierten Laserstrahl bestimmen wir die Orientierung der einzelnen Stopcockmoleküle in den Eingängen der Nanokanäle der Kristalle.

In Kapitel 9 untersuchen wir mesoporöse Silica Kügelchen mit eingeschlossenen CdSe/ZnS QDs in den Kanälen. Die Kügelchen mit verschiedenen Konzentration der in den Kanälen eingeschlossenen QDs werden analysiert. Mit einem azimutal polarisierten Laserstrahl zur Anregung bestimmen wir die Orientierung einzelner QDs in den Kanälen mesoporöser Silicakügelchen.